LAMINAR–TURBULENT TRANSITION DUE TO 2-D EXCRESCENCES AT 1% CHORD ON A SWEPT WING

A Dissertation

by

BRIAN KEITH CRAWFORD

Submitted to the Office of Graduate and Professional Studies of
Texas A&M University
in partial fulfillment of the requirements for the degree of

DOCTOR OF PHILOSOPHY

Chair of Committee,	William S. Saric
Committee Members,	Helen L. Reed
	Edward B. White
	David A. Staack
Head of Department,	Rodney D. W. Bowersox

May 2015

Major Subject: Aerospace Engineering

ABSTRACT

Laminar flow has the potential to dramatically reduce fuel consumption and/or extend the range of modern aircraft. However, before laminar-flow aircraft can be made practical, the effect of surface imperfections must be better understood. Many studies have been performed on the effects of distributed roughness and other types of imperfections. Two-dimensional step excrescences, however have not been studied in significant detail until recently. Two-dimensional steps are common on real aircraft due to practical considerations such as skin-panel junctions, high-lift-device interfaces, deicing mechanisms, etc. Traditionally, these 2-D excrescences have been treated as just another form of roughness; however, the behavior of these steps is fundamentally distinct.

The present study tests the effect of 2-D excrescences near 1% chord in order to examine the effects of pressure gradient and curvature. Testing on a 30° swept-wing model is performed in both the flight environment aboard a Cessna O-2A Skymaster, as well as in the Klebanoff-Saric Wind tunnel at Texas A&M University. In both environments, IR thermography is utilized to detect the global laminar–turbulent transition location. In the wind tunnel, a hotwire traverse is also utilized to map out the boundary layer and further measure the influence of these excrescences.

Interactions between the crossflow instability and these excrescences are observed. Both critical and subcritical step induced transition behavior is present. Comparisons are made to other contemporary experiments in order to draw conclusions about the influence of pressure gradient, sweep, and curvature on the step-induced transition behavior. The resulting data are intended for use in validating an ongoing companion computational effort.

DEDICATION

To my wife, Jessie, and my parents, Roy and Elaine

ACKNOWLEDGEMENTS

A great deal of teamwork is required for a successful flight test campaign. As such, there are numerous parties that contribute to the success of this research. This material is based upon work supported by the United States Air Force under Contract No. FA8650-12-D-3212/0005 under UDRI Subcontract No. RSC13030. This document was cleared for release under case number 88ABW-2014-5776. Any opinions, findings and conclusions or recommendations expressed in this material are those of the authors and do not necessarily reflect the views of the United States Air Force. Additional funding was provided by the Northrop Grumman Corporation. I would also like to thank Northrop Grumman for giving us access to their experiments and for sharing their pre-publication data on their unswept work.

I would like to thank Dr. William Saric for holding all of the work to a high standard, and providing a great deal of invaluable advice. I would also like to thank Dr. Saric for supporting all of my side projects. Dr. Helen Reed's input and experience was also greatly appreciated, as well as her computational perspective. Additionally, I would like to thank Dr. Edward White and Dr. David Staack for their guidance.

I would particularly like to thank Dr. Glen Duncan for all of his help with the countless hours, early mornings, and late nights in the lab. I would also like to thank him for all of the excellent discussions about the research. Without all of his help, this research would have taken a great deal longer. David West was also invaluable for all of his attention to detail and hard work. Matthew Tufts performed the CFD calculations for this effort. I would like to thank him for always getting me whatever computational data I asked for in short order.

I would also like to thank our test pilot, Lee Denham, for his excellent flying, and for always being flexible and willing to try new things. Furthermore, I would like to thank our A&P mechanic, Cecil Rhodes, for keeping the aircraft in a safe condition, and for all of his

mechanical expertise. Additionally, I would like to thank all of the crew that helped with flying in the early mornings: Dr. Glen Duncan, David West, Ian Neel, Matthew Tufts, Heather Kostak, Colin Cox, Dr. Matthew Kuester, Dr. Robert Ehrmann, Dr. Pedro Paredes, Dr. Chi Mai, Dr. Jerrod Hofferth, Alex Craig, and Dr. William Saric.

Dr. Matthew Kuester was also a great help with setting up the model in the wind tunnel, as well with the inevitable troubleshooting. I would also like to thank Dr. Glen Duncan, David West, David Monschke, Heather Kostak, and Colin Cox for all of their help with the wind tunnel setup and operation.

Finally, I would like to thank my wife, Jessie, for always being supportive through all of the long and strange hours, and for being there to help with tunnel operations when no-one else was available.

TABLE OF CONTENTS

Page

LIST OF FIGURES

LIST OF TABLES

TABLE Page

NOMENCLATURE

α	Model angle of attack, referenced to the streamwise direction
Λ	Model effective sweep angle
$\bar{a}$	Steady disturbance amplitude
δ	Boundary-layer thickness
δ_1	Boundary-layer displacement thickness
δ_2	Boundary-layer momentum thickness
δ_{99}	Boundary-layer thickness at $u/u_e = 0.99$
σ_k	Step height uncertainty
a'	Unsteady disturbance amplitude
A	Steady disturbance amplitude, integrated through the boundary layer
a_T, b_T, n_T	Hotwire temperature compensation coefficients
a_u, b_u, n_u	Hotwire calibration coefficients
c_T	Hotwire temperature coefficient
c_x, c_y	Camera image sensor center
c_p	Coefficient of pressure
$c_{p,2D}$	Two-dimensional pressure coefficient $c_{p,3D}/\cos^2(\Lambda)$
$c_{p,3D}$	Three-dimensional pressure coefficient, ratio of static pressure to dynamic pressure
E	Hotwire voltage
f_x, f_y	Camera focal depths
k	Step height, normal to the surface
k_{1-6}	Camera radial distortion coefficients
N_{exp}	Experimental n-factor
p_{1-2}	Camera tangential distortion coefficients

r	Camera fixed radial homogenous coordinate
Re'	Unit Reynolds number
Re_{ke}	Reynolds number based on conditions at the boundary-layer edge, with step height reference length
Re_{kk}	Reynolds number based on conditions at the step height, with step height reference length
s	Surface distance, normal to the leading edge
T	Local temperature
T_w	Model wall temperature
T_{ref}	Reference temperature
u	Local streamwise velocity
u'	Unsteady component of velocity
u_c, v_c	Camera image sensor coordinates
u_e	Local streamwise edge velocity
$mean, z$	Mean along the z direction
rms, z	RMS along the z direction
x, y, z	Leading edge normal (surface parallel) x, surface normal y, right handed coordinate system
x_s, y_s, z_s	Streamwise x_s, surface normal y_s, right handed coordinate system
x_{fs}	Freestream streamwise direction
x_{tr}	Streamwise transition location
x/c	Leading edge normal x location divided by leading edge normal chord distance
X, Y, Z	Model fixed coordinate frame
x_c, y_c, z_c	Camera fixed coordinate frame
x'_c, y'_c	Camera fixed homogeneous coordinates
x''_c, y''_c	Undistorted camera fixed homogeneous coordinate frame

$\mathbf{R}, \vec{t}$	Coordinate rotation and translation between model coordinates and camera coordinates
CDF	Cumulative Distribution Function
CFD	Computational fluid dynamics
DAQ	Data acquisition
FOV	Field of view
FRL	Flight Research Lab
FTE	Flight test engineer
IR	Infrared
KIAS	Knots indicated airspeed
KSWT	Klebanoff–Saric Wind Tunnel
PDF	Probability density function
PnP	Position and point
RMS	root mean square
RMSE	Root-mean-square error
RTD	Resistance temperature detector
SEM	Standard error of the mean
SWIFT	Swept Wing In Flight Testbed
SWIFTER	Swept Wing In Flight Testing Excrescence Research
SWIFTEST	Swept Wing In Flight Testing Excrescence Stability Theory
T-S	Tollmein-Schlichting
TAMU	Texas A&M University

1. INTRODUCTION

1.1 Motivation

If a significant amount of laminar flow can be maintained on a traditional transport aircraft, a drag savings on the order of 15% is to be expected Arnal & Archambaud (2009). Because of this, a practical laminar flow aircraft would show significant improvements in fuel consumption and/or range. Additionally, there would be a corresponding reduction in operating cost and emissions. However, realistic aircraft have 2-D excrescences in the form of skin panel seams, leading edge high lift devices, anti-icing devices, etc. These steps can lead to early transition, nullifying the effects of an otherwise viable laminar flow wing. The prevailing practice is to impose tight tolerances on these types of excrescences based off of earlier empirical data. These tighter tolerances directly lead to increased production costs. Additionally, for some devices, it is impractical to reduce the step size sufficiently to meet these criteria. However, if the mechanisms behind this transition phenomena can be understood, appropriate tolerances can be developed, resulting in more practical designs with much lower cost of development and production.

1.2 Reynolds Number Nomenclature

Before further discussion, some clarification of notation is necessary. For these types of experiments, R_h, Re_k, Re_{kk}, among others, have been used to name various non-dimensional parameters. Frequently, it is ambiguous exactly what is being referred to by each, and the meaning often varies from paper to paper. For clarity, this paper is written in terms of Re_{mn} where m is the reference length, and n is the boundary layer height at which properties are measured, as shown in Eq. 1.1. As presently defined, k is step height, e is the boundary-layer-edge height, and ∞ is freestream. For example, Re_{kk} would be the Reynolds number with reference length k, computed using velocity and viscosity at boundary-layer height k; Re_{ke} uses reference length k, referenced to boundary layer edge velocity and viscosity; $Re_{k\infty}$ uses reference length k, calculated using freestream velocity

and viscosity. It is important to note that when referencing to values at the step height, the velocity is measured normal to the step.

$$Re_{mn} = \frac{u_m n}{\nu_m} \tag{1.1}$$

1.3 Literature Review

1.3.1 Historical Literature

There have been several experiments studying the effects of excrescences of various forms on laminar flow. One of the first surface imperfection studies was performed by Hood in the NACA eight-foot wind tunnel, and published in 1939 (Hood, 1939). This study centered around drag measurements on a NACA 23012 airfoil influenced by numerous simulated manufacturing imperfections, including multiple types of rivets, welds, and skin joints. A study by Tani et al. (1940) later investigated the effects of wires stretched along the surface of an airfoil on transition. This study developed an empirical relationship for these types of roughness and made note of the fact that favorable pressure gradients made the flow more stable to these wire excrescences. Fage (1943) published a study on the effects of dips, humps, and rectangular profile strips. Braslow & Knox (1958) also developed a criterion for critical roughness height using strips of distributed roughness, which indicate critical Re_{kk} values between 250 and 600. Smith & Clutter (1959) attempted to reconcile many of the previous studies, along with some additional experiments with the intent of examining what exactly roughness induced transition is sensitive to. They indicated a critical Re_{kk} between 40 and 600 depending on roughness type and speed regime. Since both spanwise wires and distributed roughness appeared to behave similarly over a wide range of speed and configuration, the criterion developed by Smith and Clutter, and Braslow and Knox are frequently used to indiscriminately approximate the behavior of roughness in general. However, as was later discovered, transition due to 2-D excrescences behaves fundamentally differently from roughness induced transition.

In the early 1980s, there were a pair of experiments on an X-21 and a T-34C investigating the effects of forward facing steps (Holmes et al., 1985). These experiments found the critical R_h, defined in this paper as $Re_{k\infty}$, to be approximately 1800. Zuniga et al. (1994) and Drake et al. (1996) tested three step-gap combinations on a fin attached to an F-104. This test used two Stanton gauges to determine which of three regimes transition was occurring in. This, along with the step-gap combinations make this particular test's results difficult to compare to the present studies.

1.3.2 Contemporary Literature

Recently, there have been a set of tests performed by the Northrop Grumman Corporation (NGC) investigating the effects of both forward and aft facing steps at 15% x/c on transition for unswept flat plates and wedges. These studies have been performed in both conventional low-disturbance wind tunnels, and in a towing wind tunnel (Bender et al., 2007; Drake et al., 2008; Drake & Bender, 2009; Drake et al., 2010). These test show $Re_{k,crit}$, defined in this paper as $Re_{kk,crit}$, to be on the order of 2100 for forward facing steps, and 900 for aft facing steps. Lastly, recent work by Duncan (2014); Duncan et al. (2014a,b) has extended the NGC results to account for sweep using a 30° swept wing with a similar pressure gradient and an adjustable height step at 15% x/c. These tests were conducted both in a low disturbance wind tunnel, and in flight. The model used is called SWIFTER (Swept Wing In Flight Testing Excrescence Research). The SWIFTER test found $Re_{kk,crit}$ to be roughly between 2000 and 1300 for forward facing steps, and between 1500 and 300 for aft facing steps, depending on freestream Reynolds number.

1.4 Theory

For these types of boundary layer experiments, there are four basic instabilities that can arise; leading-edge instability / attachment line contamination, Görtler instability, Tollmein-Schlichting (T-S) instability, and crossflow instability. Leading-edge instability / attachment line contamination can be easily avoided by constraining the attachment-line momentum-thickness Reynolds number to a sufficiently small value by limiting the

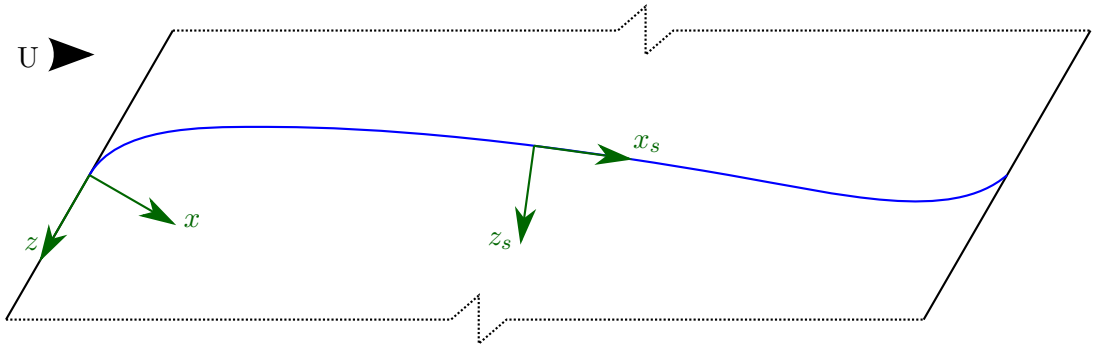

Figure 1.1: Notional crossflow streamline

leading edge radius. The Görtler instability can also be easily avoided by avoiding concave curvature within the region where laminar flow is desired. A favorable pressure gradient stabilizes the T-S instability, and as such can also be avoided by the careful design of the airfoil pressure distribution. The only remaining instability is crossflow. Unfortunately, crossflow is not so easily avoided.

1.4.1 Crossflow

Crossflow is destabilized by a favorable pressure gradient in the presence of sweep. For the transonic speeds typically obtained by transport aircraft, the trade-off of reduced wing sweep results in an increase in wave drag. Pressure gradient can be reduced to mitigate crossflow, but cannot be made adverse without rapidly inducing breakdown due to the T-S instability, or worse, inducing separation. As such, crossflow cannot be readily avoided, and must instead be managed.

The combination of pressure gradient and sweep results in a spanwise pressure gradient relative to the fluid flow. This pushes the streamlines in an S-shaped path similar to that shown in Figure 1.1, and induces a spanwise velocity component to the boundary layer profiles as shown in Figure 1.2. This spanwise velocity component becomes inflected and introduces streamwise vorticity into the flow. This streamwise vorticity manifests as streamwise co-rotating vortices and results in a spanwise periodic modulation to the mean flow, inducing the characteristic crossflow structure. This structure appears as streaking

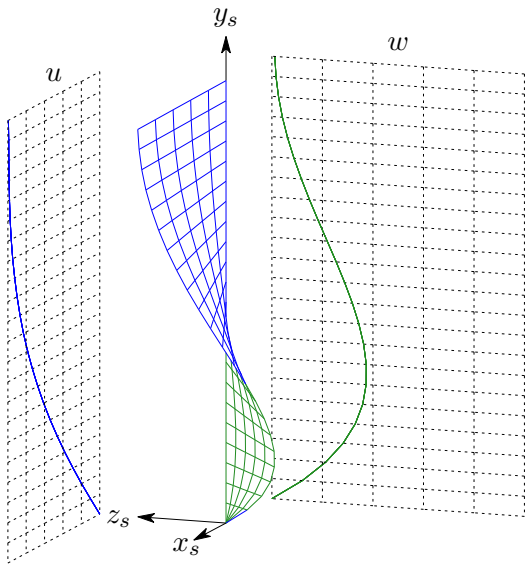

Figure 1.2: Notional crossflow profile

in visualization and measurement techniques such as IR thermography and naphthalene due to the resulting periodic upwelling of low-momentum fluid and subduction of high-momentum fluid. Eventually this mean-flow modulation creates two inflection points in the streamwise velocity profile resulting in rapid onset of high-frequency secondary instabilities and subsequent breakdown to turbulence.

1.4.2 Step-induced Separation

The main source of instability introduced by a 2-D excrescence is the entrained separation bubbles. For the aft-facing step case, a single separation bubble is entrained as shown in green in Figure 1.3. The forward-facing step case can exhibit two separated regions as indicated in green in Figure 1.4.

There is not a large quantity of literature to date on the flow in the neighborhood of 2-D excrescences in a boundary layer. Most of the work focuses either on steps in channel flow, or on the influence of the steps upon the T-S instability. Since T-S is not a significant factor in the present experiments due to the strong favorable pressure gradient, both of these scenarios are of limited direct applicability. However, those studies can be examined

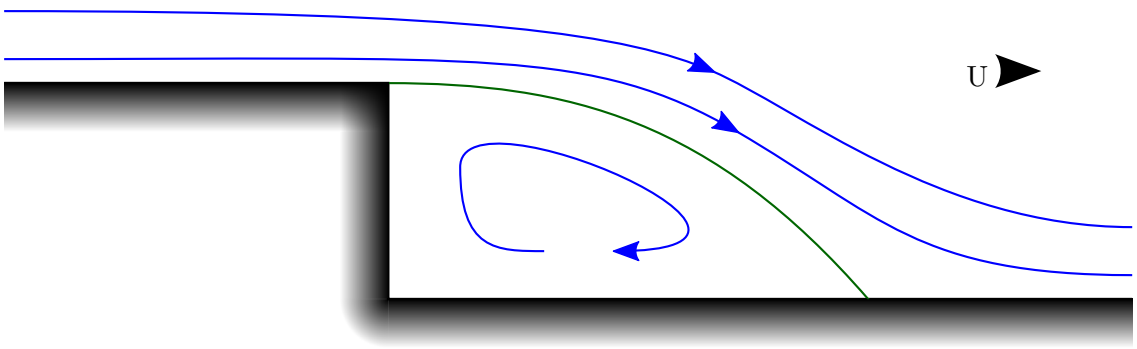

Figure 1.3: Notional aft-facing step flow. Streamlines in blue, separated region bounded in green.

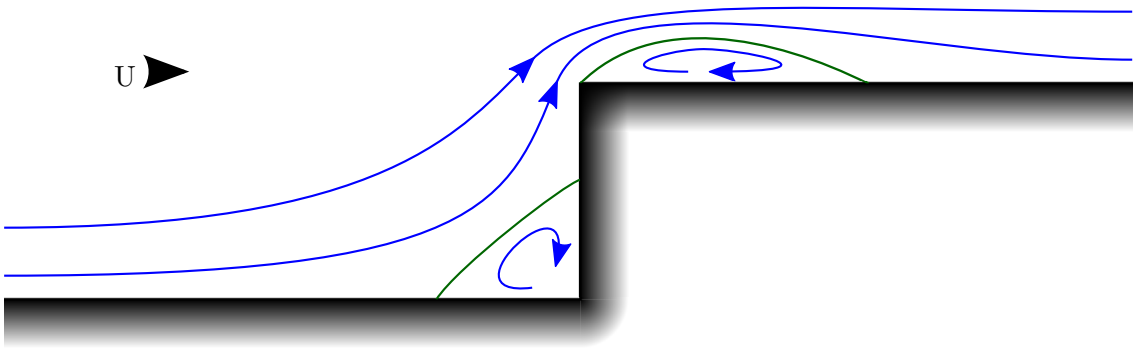

Figure 1.4: Notional forward-facing step flow. Streamlines in blue, separated regions bounded in green.

for secondary behaviors that could be applicable. Sesco et al. (2014) recently performed a set of computations on an unwept flat plate with an aft-facing step and found that the step acts as a receptivity source for both vorticity and sound on the T-S instability. In a recent computational study by Barkley et al. (2002), unswept aft-facing steps in channel flow were found to exhibit an onset of three-dimensionality at $Re_{kk} = 748$. While the flow regime is very different, it is likely that the separation bubble aft of the step would exhibit similar behavior to the boundary layer case since both are separated regions in a corner driven by a shear layer. The indication of the onset of three-dimensional behavior is particularly interesting for the present studies due to the potential for interaction with the crossflow instability.

1.4.3 Crossflow–Separation Interaction

The interplay of this spanwise-periodic instability with a step-induced shear layer is interesting on two fronts. Firstly, there is a possibility that the modulated mean flow impinging on the excrescence could stabilize or destabilize the entrained separated regions. Secondly, it is possible that the separated regions could induce or modify the spanwise disturbances, resulting in a modification of the downstream crossflow behavior. Recent work by Eppink (2014) on a swept flat plate with a wall-liner-imposed pressure gradient found evidence of such an interaction. While this interaction has been postulated and observed, it is still relatively poorly understood and has not been significantly studied until recently. One of the purposes of these experiments and companion computational effort is to further understand these interactions so that they may be modeled properly in future laminar-flow aircraft design.

2. EXPERIMENTAL SETUP

2.1 Model Modifications

The present work is an extension of the previous excrescence work at 15% x/c by Duncan et al. (2014b,a); Duncan (2014). These experiments utilize the same base model, called SWIFTER. An exhaustive explanation of SWIFTER's inner workings and design is available in Duncan (2014). This section will focus on the modifications required for testing of steps at 1% x/c as well as the specific features from SWIFTER that are directly applicable to these tests. For these experiments, a new leading-edge part was fabricated to allow for forward- and aft-facing steps to be induced at 1% x/c. The new configuration is called SWIFTEST (Swept Wing In Flight Testing Excrescence Stability Theory). Figure 2.1 shows SWIFTEST in flight. The polished portion on the right side of the image is the new leading edge part. As with SWIFTER, the first 15% of SWIFTEST is highly polished to reduce the effects of roughness so that the other parameters can be studied without interference. The RMS roughness of the polished region is 0.09 µm.

Figure 2.1: SWIFTEST in flight

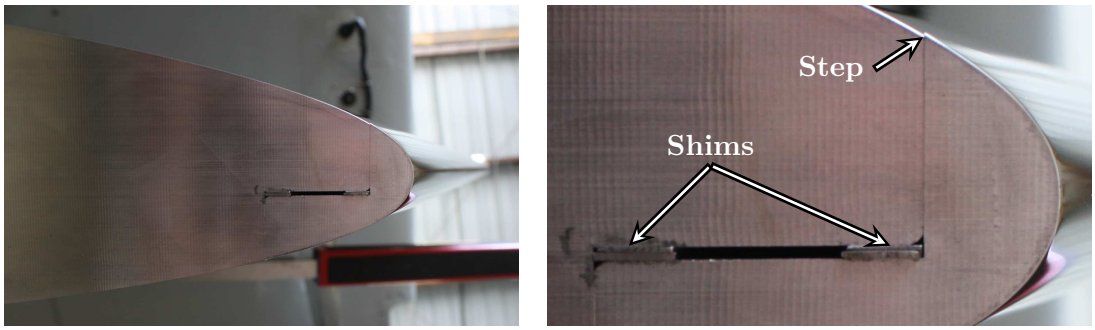

Figure 2.2: SWIFTEST leading edge with shims installed

2.1.1 Step Adjustment

SWIFTEST utilizes the same main body as SWIFTER (aft of 15% x/c), but with a new leading-edge part. The new leading-edge part does not have any flight movable parts; as such, adjustments to its step height are performed on the ground before each test. The leading-edge part is split into a main body and an adjustable tip piece as shown in Figure 2.2. The spacing between the adjustable tip piece and main body is fixed by a set of interchangeable steel shims indicated in the figure. Thicker or thinner shims can be installed in order to induce a forward- or aft-facing step, respectively, at 1% x/c. A set of 25, 51, 127, 254, 508, and 787 µm shims can be used in any combination to allow for steps between 1323 µm aft facing, and 1983 µm forward facing in 21 µm increments, with an RMSE of approximately 7 µm. A full list of all possible shim configurations and their associated uncertainties is available in Appendix C. The shims are manufactured from off-the-shelf steel shims stock which has been cut down to size using a sheet metal shear and filed to remove the burrs.

Figure 2.3 shows a picture of the non-test-side (NTS) of SWIFTEST installed in the wind tunnel, with a handful of key features highlighted. Alignment between the tip and main body is maintained by a set of three guide shafts with sleeve bearings (circled in green). Once the shims are installed, a set of eight cap screws are used to fix the adjustable tip to the main body (circled in blue). In order to separate the tip from the body in order

Figure 2.3: SWIFTEST installed in the wind tunnel, with key features highlighted

to swap shims, there are a pair of push-off holes (circled in maroon) where a threaded knob can be inserted and used to separate the halves. In order to prevent suction or blowing through the seam from corrupting the results, all exposed seams and holes on the root, tip, and NTS are covered with Kapton tape after the shims are installed.

2.1.2 Step Uncertainty

Several shims were measured using a micrometer at approximately 25 mm intervals across the entire length of the shim. The RMSE of the thickness of the shims compared to their specified thickness was approximately 2 µm; this is significantly better than their rated specification. As such, more exotic shims were not pursued. The uncertainty after repeated assembly and test was found to be approximately 7 µm. That uncertainty is a combination of machining uncertainty and any non-repeatability between shim reinstalls. In order to test that uncertainty, the non-contact surface profilometer developed in house was used to take measurement passes across the step every 1 mm for a handful of different shim configurations. Plots for two different steps are shown in Figure 2.4. The target step is marked as a dashed line, while the measured value is in solid black. The details of the profilometer itself, along with its associated data reduction techniques are available in Crawford et al. (2014).

2.2 Flight Testing

For the flight testing portion of this research, the model is mounted under the port wing of a Cessna O-2A Skymaster as shown in Figure 2.5. This aircraft is particularly suited to this type of work due to its existing hardpoints. These hardpoints were designed to carry heavy ordnance when the plane was flown by the Air Force. With minimal modification, they have been repurposed to carry flight experiments. Additionally, the O-2A has places for four crew. For these experiments, only three crew are utilized (pilot, co-pilot / safety observer, and flight test engineer (FTE)). The fourth seat is removed, and a FLIR SC-8100 IR camera is installed in its place; it faces out of the open port window, as indicated in Figure 2.5. This IR camera is utilized for detailed global transition measurements, and

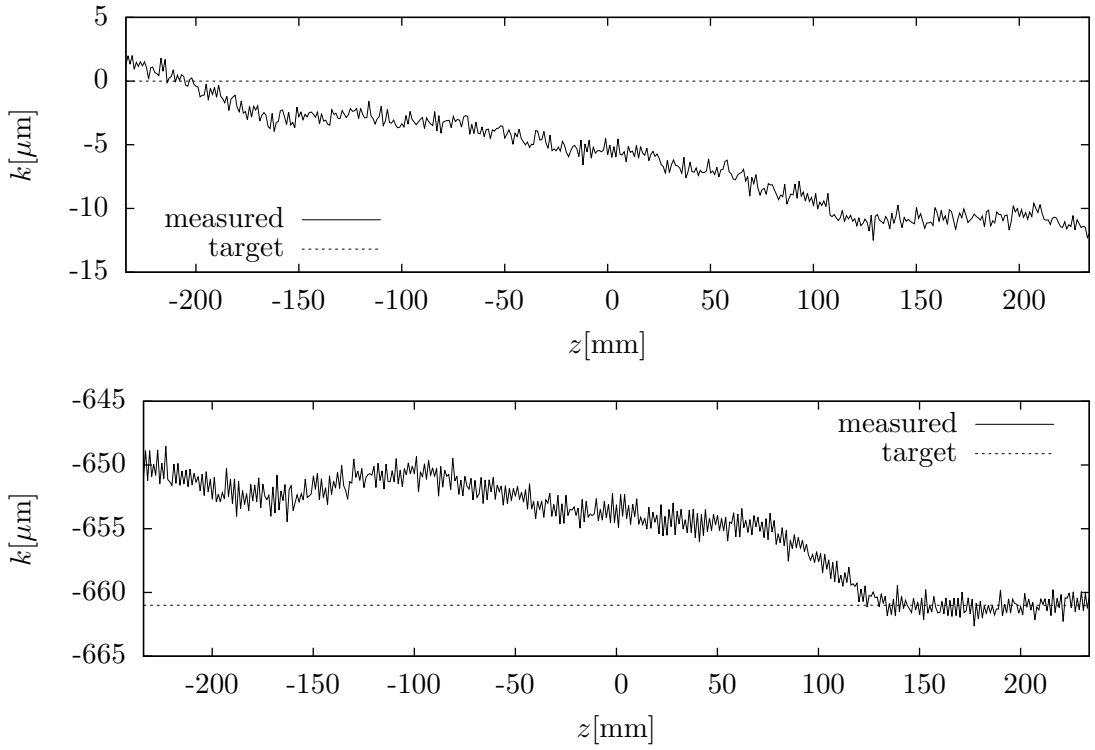

Figure 2.4: Measured step height for $k = 0\,\mu\text{m}$ (top) and $k = -661\,\mu\text{m}$ (bottom)

Figure 2.5: SWIFTEST installed on a Cessna O-2A Skymaster

is the primary measurement technique for these flight tests. The technique for extracting detailed transition location is explained further in section 3.1. The O-2A is capable of achieving unit Reynolds numbers of $2.2 - 6.0 \times 10^6$/m. However, due to the high angle of attack required to hit the low Reynolds numbers (resulting in large deviations in the effective sweep of the vertical model), the useful test regime is $4.0 - 6.0 \times 10^6$/m.

2.2.1 Safety Analysis

A detailed structural analysis and flutter / handling-qualities test was performed on the original SWIFTER test article before the start of its testing campaign. Full details of these analyses and tests can be found in Duncan (2014). For SWIFTEST, only the leading edge was replaced. As such, the safety analysis for this test concentrated on the effects of the relatively minor modification.

The new leading edge is 2.4 kg heavier than the previously used leading edges. This brings the overall weight of SWIFTEST to 109 kg. However, this is still lighter than SWIFT at 112 kg, which was flown successfully as the predecessor to SWIFTER. This additional weight also results in a 3% increase in the model's pitch moment of inertia about the reference point on the aircraft pylon, and a 10 mm forward shift of the model CG compared to SWIFTER. The resulting pitch moment of inertia for the model is slightly (less than 1%) lower than the largest ordnance originally cleared for this aircraft by the Air Force. Flutter qualities were not significantly impacted due to the fact that the most critical flutter mode is the symmetric empennage bending mode, which is noted to be insensitive to wing store configuration, as per Cessna report S-M337-27-3 (Cessna, 1968). In order to further mitigate risk, a clearance flight was performed with the same procedures used to clear both SWIFT and SWIFTER. During the clearance flight, there was no discernible difference from the previous results obtained from the clearance of SWIFTER.

Structurally, the new leading edge is stronger than the original leading edges. The new leading edge is made from 7075-T651 aluminum, which is the same material as the original leading edges. Both principal moments of area and the polar moment of area of the cross-section of the new leading edge are larger than those of the original leading edges. This is to

be expected due to the additional material needed for the step system. The cross-sectional schematics on the previous page show this additional structure. The additional mass does incur some additional loading on the internal components. However, since the lift load on the leading edge is much higher than the inertial load of the leading edge, the extra load is minor. The worst-case component factor-of-safety on the sleeve bearings that hold the leading edge part is reduced from 5.0 to 4.9 due to the additional mass of the leading edge, where component factor-of-safety is defined as ratio between the rated load capacity of the off-the-shelf part and the maximum expected load applied. Additionally, the worst-case component factor-of-safety to yield on the existing rail guides is reduced from 7.0 to 5.7. This design was presented to and approved by an Air Force Technical Review Board (TRB) and Safety Review Board (SRB).

2.2.2 Air Data

Model angle-of-attack, effective sweep, and velocity, and static pressure are all measured via an Aeroprobe 5-hole probe attached to a set of three differential and one absolute Honeywell FP2000 pressure transducers. The transducers are mounted inside a temperature controlled enclosure inside the SWIFTER main body in order to mitigate uncertainty due to temperature drift. An extensive calibration of the 5-hole probe was performed by Aeroprobe and processed into a very accurate set of calibration curves in house. Details of the calibration curves can be found in Duncan et al. (2014b). The 5-hole probe is mounted to the non-test-side of the model on a set of standoffs at midspan. It is visible in Figure 2.1. Freestream static temperature is measured using a SpaceAge Control 4222-05 temperature probe. The resulting uncertainties are listed in Table 2.1. These values were obtained through a thorough uncertainty analysis of this system as documented in Duncan (2014). The systemic uncertainty includes all sensor and calibration uncertainties. The typical total uncertainty includes the standard deviation of the measurements over a typical one-second data-burst on-condition, and is a function of pilot skill and atmospheric conditions.

One of the main improvements to the DAQ system between SWIFTER and SWIFTEST is the inclusion of hardware time synchronization between the IR camera and air data

Table 2.1: Flight air data system uncertainties

Variable	Systemic	Typical Total
α	0.10°	0.13°
Λ	0.22°	0.24°
Re'	0.02×10^6/m	0.02×10^6/m

system to within 40 ms. This allows for much shorter stabilization times. For a datum point to be considered good, it must be held on condition for one second with a total uncertainty of better than 0.05×10^6/m for Re' and 0.25° for α. When the data are processed, the first 0.1 second is thrown out to account for stabilization, and the remaining 0.9 seconds is processed. Previously, the software synchronization was only good to the nearest second. As such, three seconds were required on condition, and the middle one second was processed to insure the IR data was within the on-condition region. This reduction in required time makes holding the aircraft steady for a data point significantly easier.

The other associated modification was a loosening of the target conditions for the pilot. Previously, the FTE requested a condition, and the pilot aimed for that exact condition, and only that condition was collected. For SWIFTEST, the FTE requests a condition, but the data acquisition system is always watching for any stable condition, regardless of what it is. As such, if the FTE requests $\alpha = -6.5^\circ$, but the DAQ system detects a stable 1 second burst at $\alpha = -6.3^\circ$, the system pulls that point anyway. The result is a cloud of essentially free data around each targeted data point. Previously, a typical flight would capture 30-60 test conditions in a fairly regular grid. With this new technique, flights typically capture 300-500 test conditions each in a cloud over the entire test regime.

2.2.3 Typical Flight Profile

During a typical flight, the crew takeoff and depart towards one of two possible test areas, at the discretion of the FTE, and climb to 6500 ft (2000 m) MSL. Once at altitude, the co-pilot reads off the pre-dive checklists. Once the checklists are complete, the dive

begins. The throttles are pushed to full open, and elevator is used to control Re', while the rudder trim controls α. The rudder trim allows an α as low as $-7.5°$. Beyond that point, rudder pedals must be used, which are significantly less steady than the trim wheel. Above $-5.5°$, SWIFTER and SWIFTEST are fully laminar for the Re' ranges tested; as such, α is tested between $-5.5°$ and $-7.5°$. Below $Re' = 4.0 \times 10^6$/m, the aircraft angle-of-attack becomes high enough that the effective sweep of SWIFTER/EST drops below 28°; because of this, lower speed testing is not performed in flight. The upper limit on Re' is generally 5.7×10^6/m in the summer, but can be as high as 6.0×10^6/m in the winter due to the cooler weather. The limiting factor is the upper limit on airspeed of 175 KIAS due to aircraft structural limitations with wing stores installed. The current Re' and α are displayed on a small screen attached to the pilot's yolk, along with their target values. While the pilot attempts to maintain the requested conditions, the FTE monitors the quality of incoming data, and requests the next condition when sufficient data are acquired at the present point. Since the pilot and FTE are occupied managing the test, the co-pilot monitors the traffic and engine vitals. The co-pilot also calls out the altitude in 1000ft (300m) increments. Once 3000ft (900m) MSL is reached, the FTE calls to terminate the test, and the climb / dive process is repeated until all test points are collected, or fuel gets too low. Since α is more difficult to control and maintain, it is typically held constant, while Re' is incremented from slowest to fastest. At the beginning of the next dive, a new α is selected as necessary.

2.3 Wind Tunnel Testing

The SWIFTER/SWIFTEST model is also designed to be mountable in the Klebanoff-Saric Wind Tunnel (KSWT). The KSWT is a low-disturbance wind tunnel facility at Texas A&M University. The turbulence intensity at the speeds tested is between 0.017% and 0.030%, bandpassed from 1 Hz to 10 kHz (Downs, 2012). It has a 1.4 m by 1.4 m test section, and is capable of unit Reynolds numbers of $0.5 - 1.5 \times 10^6$/m for extended periods. The KSWT is capable of closed loop Reynolds number control, and has an overall unit Reynolds number uncertainty of 0.005×10^6/m. Additional information about the KSWT

can be found in Hunt et al. (2010).

When SWIFTER or SWIFTEST are installed in the KSWT, the model must be inverted in order to be oriented correctly with the flow and with the test side facing the control room. For these experiments, SWIFTEST is mounted at an angle-of-attack of -2.0° measured normal to the leading edge (-1.73° relative to the streamwise direction). This angle-of-attack was chosen to provide a global pressure gradient over the test region that is similar to that seen in the center of the flight test regime. The angle-of-attack is markedly different from the flight configuration due to a combination of the vertical-wall effects in the wind tunnel as well as the tip effects in flight. Additionally, this configuration is near zero lift for the airfoil, and as such, the ideal wall liners have a relatively flat shape. Initial testing on SWIFTER was performed without wall liners, and it was found that this allowed for an acceptably spanwise-uniform pressure gradient.

There are three interchangeable test section windows: a glass one for optical access, an acrylic one with viewing ports for IR thermography access, and an articulated viewing window to accommodate the hotwire traverse. The first round of SWIFTEST testing utilized the IR viewing window and camera to rapidly map out the transition behavior. Once the transition behavior was mapped, the hotwire was utilized to examine the boundary layer in more detail.

Figure 2.6 shows the IR camera installed in the KSWT. Five viewing ports are available. For these tests, the IR camera was installed in the middle port. In order to avoid issues with IR transparency, an open port is utilized. The IR camera is placed in the open port as in the top of Figure 2.6, and the pressure box is then sealed around the camera as shown in the bottom image, in order to avoid flow through the open IR viewing port. As with flight, the FLIR SC-8100 camera is utilized in conjunction with SWIFTER's internal heating sheet. Details of this procedure are provided in section 3.1.

For hotwire testing, the articulated window and associated hotwire traverse system was installed as shown in Figure 2.7. The top image shows the hotwire in its calibration location. The articulated window utilizes a zipper that is attached to the traverse in order

Figure 2.6: SWIFTEST in the KSWT with IR camera installed in middle port

to provide a movable opening for the sting. Since the zipper does not provide a fully air-tight seal, the pressure box is also utilized for the hotwire configuration. The bottom image shows the hotwire traverse carriage system, window actuators and pressure box.

The wires utilized are 1.25 mm long, 5 µm diameter tungsten welded to Dantec Dynamics boundary layer and freestream probes. They are driven by an AA Labs AN-1003 10 channel constant temperature anemometer. The output of the anemometer is directly recorded to obtain the DC component and also passed through a KEMO dual two-channel filter, bandpassing the signal from 1 Hz to 5 kHz to obtain the AC component. The KEMO filter also applies a 20 dB gain to the boundary layer probe, and a 30 dB gain to the freestream probe. Details of the subsequent testing and processing are provided in section 3.2.

2.4 Coefficient of Pressure

The model has a two rows of static-pressure taps located at 234 mm inboard and outboard of midspan. There are 16 ports in each row, 14 on the test size, and two on the non-test-side for verification of loads analysis. No ports were placed in the leading edge in order to avoid disturbing the test region. In order to avoid a changes in c_p due to a moving transition front, the boundary layer is intentionally tripped in front of the pressure taps. Pressure measurements were performed using an ESP-32HD pressure scanner with a ± 2.5 kPa range. Figure 2.8 shows the experimentally determined c_p with the according uncertainties plotted alongside the CFD solution computed by Matthew Tufts. The CFD solution agrees well with the experiment, providing confidence that both the model is set up as intended, and that the CFD solution is accurately modeling the problem. The CFD solution is utilized for boundary layer profiles for computing Re_{kk} as well as to reference local c_p since the CFD solution can provide an accurate pressure at arbitrary location, particularly near the step locations since a pressure tap cannot be placed in the step effectively. Additionally, the CFD solution can compute pressure data at midspan. Furthermore, it is not possible to measure the boundary layer velocity profiles in flight due to the lack of a hotwire traverse or other similar apparatus. As such, the CFD solution is utilized when

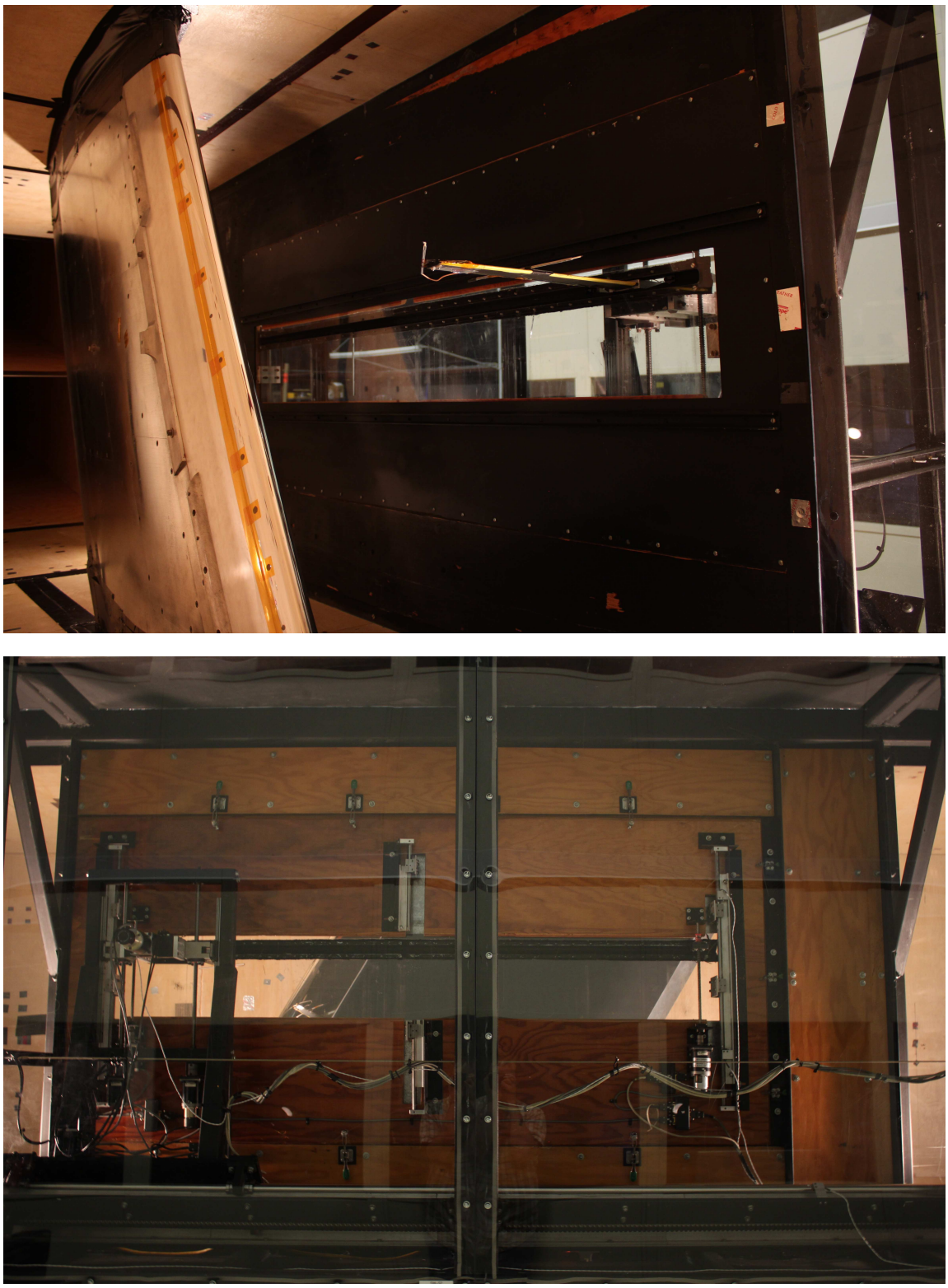

Figure 2.7: SWIFTEST in the KSWT with IR camera installed in middle port

such values are required.

Figure 2.9 shows a comparison of the CFD solution pressure distributions. The c_p in the KSWT is slightly higher, and the pressure gradient is slightly more uniform across the middle portion of the model, as compared to the flight cases. The overall pressure gradient for the KSWT installation is similar to that of the $\alpha = -6.5°$ flight case. However, as will be discussed later in the results, the pressure gradient local to the step appears to be more significant. Figure 2.10 shows the pressure gradient near 1% x/c. At 1% x/c, the KSWT has the highest pressure gradient of any of the configurations. Counterintuitively, at 1% x/c, the less-negative α have higher pressure gradient. This is due to the steepening of the pressure gradient at the forward portion of the airfoil, while the pressure gradient is reduced over the majority of the airfoil, as α is made more positive.

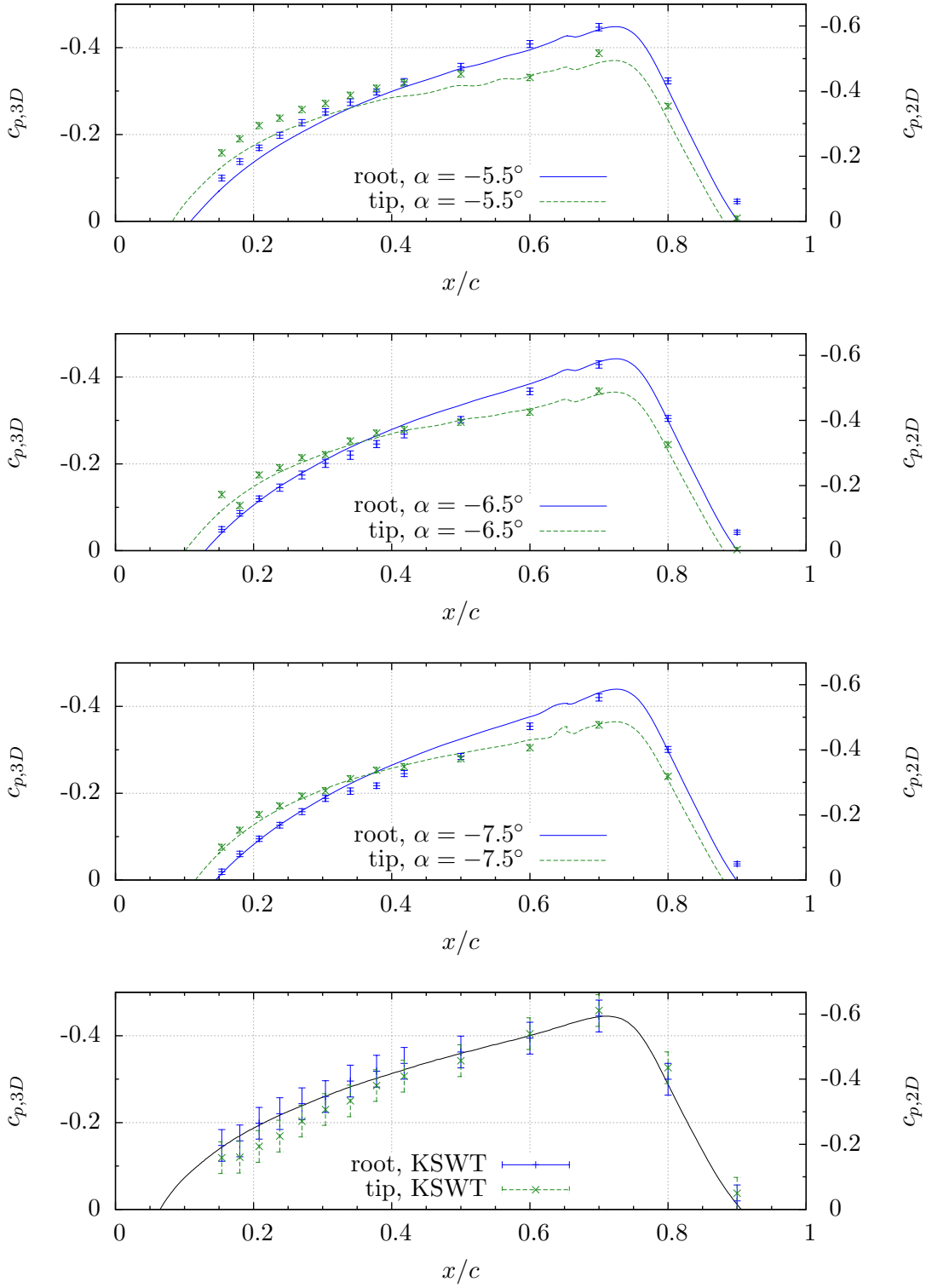

Figure 2.8: Experimental coefficient of pressure

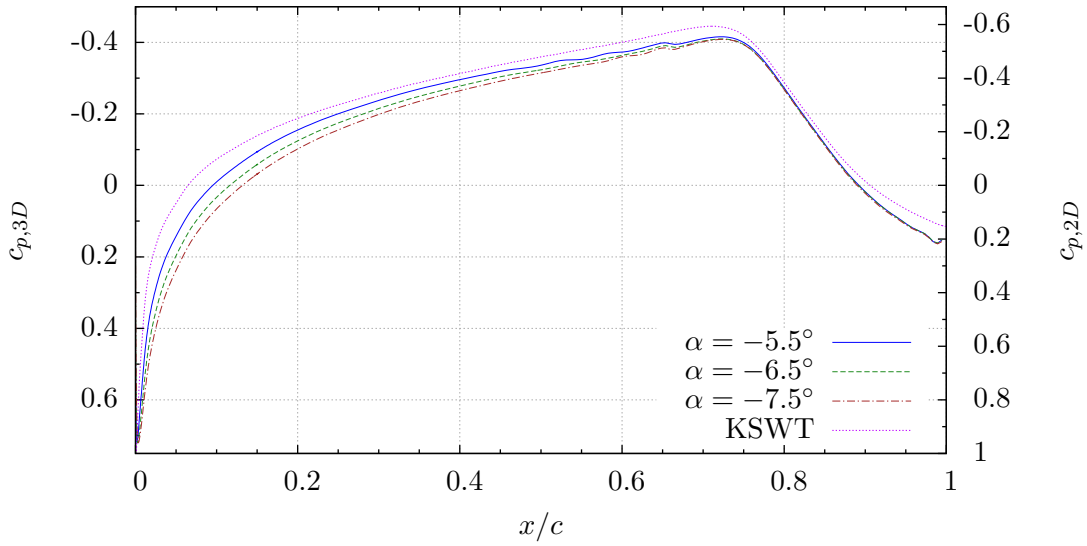

Figure 2.9: Coefficient of pressure

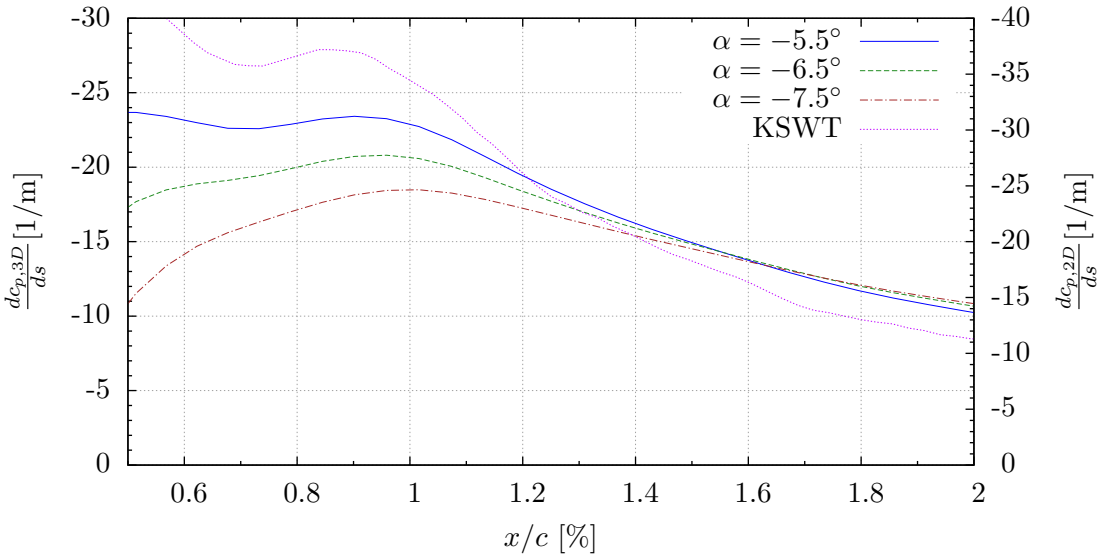

Figure 2.10: Local pressure gradient near 1% x/c

3. EXPERIMENTAL TECHNIQUES

3.1 IR Thermography

Infrared (IR) thermography has been commonly used for global detection of laminar-turbulent transition fronts. This transition-detection technique exploits the fact that shear stress correlates directly with the convection rate. Given a non-zero heat transfer rate through the skin of the model under study, a temperature differential will develop between the laminar and turbulent regions. This differential can be effectively imaged with the use of an IR camera. Once the surface temperature field is measured, these data must then be interpreted in some manner to extract the transition location.

Traditionally, this has been done visually by a human. Unfortunately, humans are notorious for inducing bias error when subjectively evaluating images. Additionally, in a crossflow dominated environment, the transition front is typically quite jagged. In effect, the human interpreting the images must read some single representative transition location from a very complex signal. In general, measurements taken in this fashion can only be trusted to accuracy on the order of $\pm 5\%$ chord. Furthermore, IR images are not solely functions of shear stress. Variations in heating or cooling, surface emissivity, internal conduction due to structural members, reflections from nearby hot bodies, and numerous other phenomena induce not insignificant noise into the IR image. Finally, since each image must be analyzed by hand, a significant amount of time is required to adequately reduce the data from a significant number of images. In a typical 1.5 hour SWIFTEST flight, approximately 300 test points are measured. If a skilled person is reducing the data, 6 seconds per image is a reasonable pace. At that rate, reducing 300 images takes about half an hour. In practice, bursts of approximately 20 images are used to get more accurate measurements. This would take approximately 10 hours to reduce just one flight worth of data. Due to all of these factors, a more rigorous computer automated analysis technique was developed.

3.1.1 Experimental Setup

IR thermography has two key experimental requirements: there must be heat transfer through the surface being studied, and the surface must be capable of holding a crisp temperature gradient.

3.1.1.1 Temperature Differential Generation

In order to generate a measurable temperature gradient for IR thermography, the model under study must be either heated or cooled to drive the laminar-turbulent surface temperature differential. Generally, this temperature differential must be induced by an external means. One option is to either heat or cool via means such as heating wire or water cooling. The other option is to heat or cool the freestream fluid, whether by rapid altitude changes in flight, or via cycling of the cooling system in a wind tunnel. Only a few degrees of heating or cooling is required to obtain a very clear image. This can be thought of as a $T_w/T_{w,adiabatic}$ variation on the order of one percent for most conditions. Such minimal temperature variation does not significantly affect the boundary layer stability for most phenomena. Verification of this fact can be readily achieved by disabling the heat/cooling source, and carefully watching for motion of the transition front as the model approaches equilibrium.

For the SWIFTER/SWIFTEST model, internal electric heating wire was used, along with an internal insulating blanket, to direct the majority of the heat transfer through the test surface of the model. Figure 3.1 shows a notional graphic of the configuration used. The power density required to achieve sufficient temperature differential at a flight $Re' = 6.0 \times 10^6/\text{m}$ was approximately $300\,\text{W/m}^2$. Off-the-shelf heating wire designed for use heating hardwood and tile floors is ideal for this purpose. It is both cheap and readily available. It also achieves these power densities with 25 mm wire spacing, which results in fairly uniform heating through a 3 mm aluminum skin. Furthermore, the wire is already shielded and sheathed, which serves as both a safety precaution against nicking and shorting, as well as electrical shielding which helps reduce any interference with neighboring

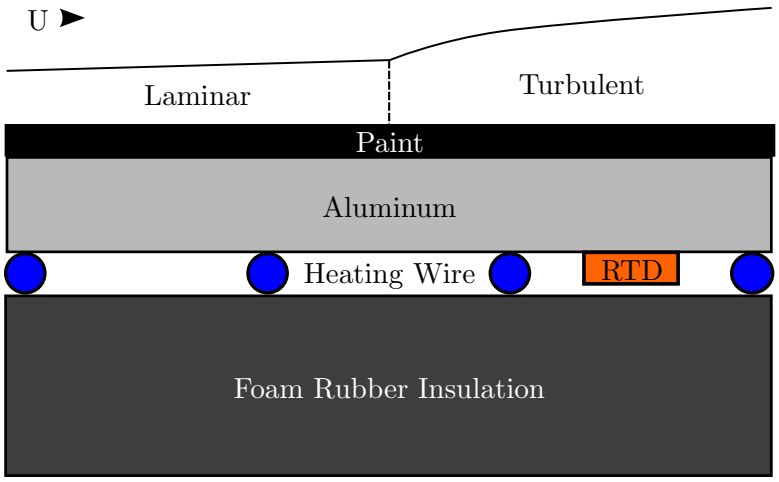

Figure 3.1: Heating sheet diagram

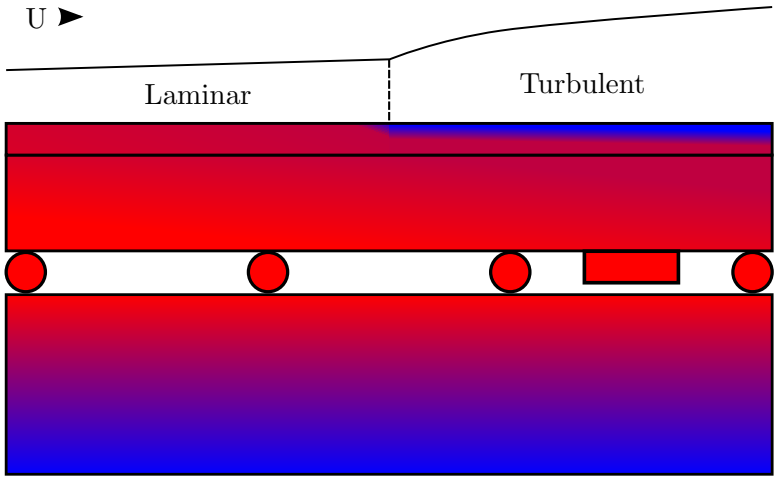

Figure 3.2: Notional temperature map

electronics when the wire is switched on and off to control the temperature. Closed-loop temperature control is easily achieved using an off-the-shelf process controller and a pair of RTDs, one on the inside of the heated surface of the model, and the other on the unheated side of the model. The second RTD serves as a reference temperature, so that temperature differential relative to an unheated wall can be maintained, rather than absolute temperature. This allows for operation in widely varying freestream temperatures without user intervention.

3.1.1.2 Surface Coating

The other primary requirement for IR thermography is a surface coating with high emissivity in the IR band being imaged, as well as a low thermal conductivity. Additionally, the coating must be at least on the order of 300 µm thick to support a crisp temperature gradient. However, it is also advantageous for the underlying substrate to be highly thermally conductive when using internal heating/cooling in order to help distribute the heat for a more uniform internal temperature. A notional drawing of the temperature gradients involved is shown in Figure 3.2. Most of the thermal gradient is in the paint itself, while the underlying aluminum substrate is much more uniform in temperature, and serves to spread out the heat from the discrete wires. The high emissivity of the coating is required in order to accurately read the surface temperature using an IR camera, as well as to reduce reflections on the surface due to neighboring hot or cold bodies.

To fulfill the coating requirements on the SWIFTER/SWIFTEST model, six coats Sherwin Williams F93 lusterless black aircraft paint, conforming to MIL-PRF-85285 Type 1, Class H, were applied to the model over the corresponding recommended primer. This particular paint has the added benefit of being representative of what would be applied to a typical military transport aircraft. Furthermore, it is both relatively inexpensive and readily available through most aircraft paint suppliers. It is important to note that the surface must not be sanded. Even the lightest sanding destroys the high emissivity properties of the paint.

3.1.2 OpenCV

The OpenCV library is utilized to dramatically simplify many of the operations used in the following image processing processes. OpenCV provides functions for many generic filtering operations, as well as a relatively thorough model for handling camera and lens distortion. Several functions for estimating position and point (PnP) are also provided, utilizing the aforementioned camera model. The image filtering is fairly straightforward; however, the camera model and PnP estimation deserves some brief explanation for clarity since they are used heavily throughout the following algorithm. A much more thorough treatment of these algorithms can be found in the OpenCV manual.

The camera model utilized is nonlinear, and accounts for variables including image sensor geometry, lens distortion, and perspective transformation. The full model is as follows:

$$\begin{bmatrix} x_c \\ y_c \\ z_c \end{bmatrix} = \mathbf{R} \begin{bmatrix} X \\ Y \\ Z \end{bmatrix} + \vec{t} \tag{3.1}$$

$$\begin{bmatrix} x'_c \\ y'_c \end{bmatrix} = \frac{1}{z_c} \begin{bmatrix} x_c \\ y_c \end{bmatrix} \tag{3.2}$$

$$r = \sqrt{x'^2_c + y'^2_c} \tag{3.3}$$

$$x''_c = x'_c \frac{1 + k_1 r^2 + k_2 r^4 + k_3 r^6}{1 + k_4 r^2 + k_5 r^4 + k_6 r^6} + 2p_1 x'_c y'_c + p_2 \left(r^2 + 2x'^2_c\right) \tag{3.4}$$

$$y''_c = y'_c \frac{1 + k_1 r^2 + k_2 r^4 + k_3 r^6}{1 + k_4 r^2 + k_5 r^4 + k_6 r^6} + p_1 \left(r^2 + 2y'^2_c\right) + 2p_2 x'_c y'_c \tag{3.5}$$

$$\begin{bmatrix} u \\ v \end{bmatrix} = \begin{bmatrix} f_x & 0 \\ 0 & f_y \end{bmatrix} \begin{bmatrix} x''_c \\ y''_c \end{bmatrix} + \begin{bmatrix} c_x \\ c_y \end{bmatrix} \tag{3.6}$$

Eq. 3.1 defines the standard rotation–translation transformation between the model

coordinates (X, Y, Z) and the camera coordinates (x, y, z). Eq. 3.2 transforms the camera coordinates into homogeneous camera coordinates (x', y'). Eq. 3.3, 3.4, and 3.5 remove the distortion due to camera lens effects. The variables k_{1-6} are the radial distortion coefficients, while p_{1-2} are the tangential distortion coefficients. These coefficients are determined a-priori via imaging multiple fiducial grids of known geometry at different orientations. Solving for the coefficients then becomes a non-linear least-squares optimization problem, which is readily solved using the Levenberg-Marquardt algorithm. Eq. 3.6 is a standard pinhole camera model, which takes the undistorted homogeneous coordinates, (x'', y''), and transforms them into their image sensor coordinates, (u, v). The f_x and f_y coefficients are the focal depth of the camera, and the c_x and c_y coefficients are the image sensor origin, in pixel coordinates. These values are readily available in the spec sheet of the FLIR SC-8000 camera and its lenses. However, to help account for manufacturing tolerances, these values were solved for using the same technique as the lens distortion coefficients.

Once the camera is fully calibrated, the unknown rotation matrix, $\mathbf{R}$, and translation vector, $\vec{t}$, can be solved for using non-linear least-squares given at least six corresponding image-sensor-coordinate to model-coordinate pairs. The OpenCV function that performs this calculation is called *solvePnP*.

3.1.3 Image Filtering

The data directly from the SC-8100 camera is in the form of raw integrated sensor counts that relate nominally to the intensity of the IR signal received. Before every test, a uniform cold plate is imaged, followed by a uniform warm plate. These calibration images are used to normalize the gain and offset of the entire sensor on a per-pixel basis. This removes much of the static noise from the image sensor due to pixel-to-pixel variation in sensitivity. Additionally, these images are used to identify any dead, stuck, or flickering pixels for later removal. Periodically, a more in-depth temperature calibration is also performed. This calibration consists of imaging several plates of different known uniform temperatures. These known temperature plates are used to develop a set of calibration

curves transforming the raw sensor counts into radiance values, and then from radiance into temperature.

When processing these data, the span and offset correction from the two plate test is first applied to the raw data. These corrected data are then converted into temperature readings using the multi-plate calibration curves. Next, any damaged pixels are reconstructed by interpolating from neighboring good pixels. Up to this point, the process is identical to that performed by the off-the-shelf FLIR ExamineIR software provided with the camera. The freestream temperature from a freestream RTD probe is then subtracted from the image. A copy of the image is then spatially low-passed using a Gaussian filter. The original image is then divided by the low-passed copy. The result is the local percent variation in heat transfer. In dividing by the low-passed temperature, any spatially slow-varying phenomena such as heating sheet variation and varying heat transfer rate due to structural members are suppressed. All that remains is the local variation in heat transfer due to shear stress. Since shear stress is directly proportional to convection rate, the percent variation in convection rate is also the percent variation in shear stress. As such, the image is now in terms of local percent-variation in shear stress. It should also be noted that this conversion to percent variation in shear stress is completely agnostic of whether the model is heated or cooled. It is also largely independent of the degree of heating or cooling. The only constraint is that if the degree of heating or cooling is too low, the denominator becomes small, and the signal becomes small, causing the remaining sensor noise to dominate, thereby washing out the signal; however, a few tenths of a degree differential is sufficient for a clear image.

3.1.4 Image Coordinate Mapping

This first step in rigorously detecting quantitative transition location from an IR image is to map each pixel on the camera's image sensor to the corresponding model coordinate that it is measuring. In general terms, one must first track some identifying features on the model, such as fiducials. These fiducials are then used to determine the position and point (PnP) of the camera. The image is finally undistorted using a combination of the known PnP of the camera relative to the model, in addition to the a-priori knowledge about the

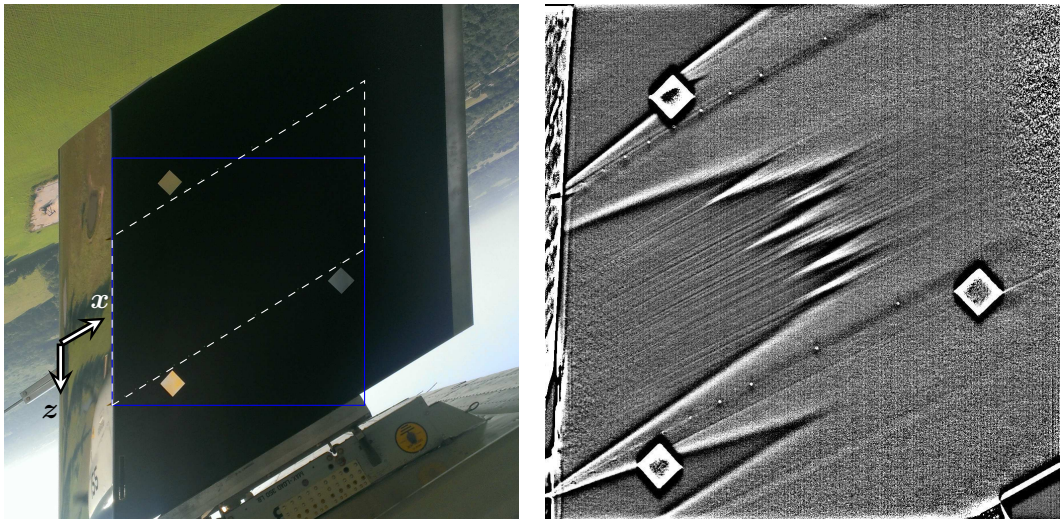

Figure 3.3: SWIFTEST in flight (left), rotated to match IR camera coordinates; IR camera FOV in solid blue; Region of interest in dashed white. Sample IR image (right)

geometry of the model, the geometry of the camera sensor, and the distortion caused by the non-ideal behavior of the camera lens.

Figure 3.3 shows a visible spectrum image of the SWIFTEST model in flight on the left, with the corresponding IR image on the right. The image is rotated such that flow is from lower left to upper right in order to avoid confusion as the images are transformed into their final coordinate system with flow from left to right. This keeps the images consistent in orientation between the flight, wind tunnel, and CFD solutions. The approximate field of view of the IR camera is outlined in solid blue, and the region of interest for these tests is outlined in dashed white. Once the undistortion process is complete, the output image is bounded by the dashed white line, and referenced to the $x-z$ coordinate system indicated. The fiducials to be tracked are visible in the image on the left as three silver squares, and as three white squares in the IR image.

3.1.4.1 Fiducial Tracking

The fiducials used for this experiment are three 51mm squares of silver mylar tape. These fiducials were chosen to have a very low emissivity to provide a sharp contrast with

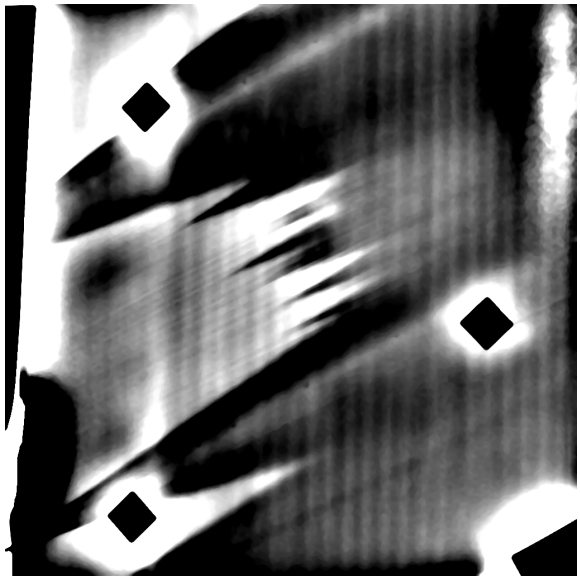

Figure 3.4: Filtered fiducial tracking image

the high-emissivity surface of the model. These fiducials were placed in a triangle configuration just outside the region of interest on the model. Their locations were determined relative to the known pressure tap locations on the model to within 100 µm using calipers. This provides four vertices of known location per fiducial for a total of 12 vertices to be tracked with known locations in the model coordinate space.

In order to facilitate tracking of the fiducials, a copy of the image of interest is first spatially high-passed on the scale of the fiducials themselves. This removes any features in the image larger than the fiducial which makes the fiducials themselves significantly easier to track. Additionally, the image is spatially median filtered to remove much of the high-frequency noise present in the IR sensor itself, while preserving the edges of the fiducials. Finally, a Gaussian filter is used to further remove any high-frequency noise. The result is shown in Figure 3.4. After filtering, the magnitude of the spatial gradient is taken using a Sobel filter, and stored for later use.

At this point, a coarse set of fiducial locations is generated by thresholding the image into black and white at a low threshold. Any closed contours are stored, and the process is

repeated for a slightly higher threshold. This process continues until the image is completely black. The resulting set of closed contours is then reduced to quadrilaterals using the Ramier-Douglas-Peuker algorithm. Any contours that exhibit large error when reduced to quadrilaterals are discarded. If a resulting quadrilateral is convex, it is also discarded, as there is no orientation of a concave fiducial that would result in a convex projection in the image space. Finally, any highly-skewed quadrilaterals are discarded, as the model is not expected to be at a highly-oblique angle.

The resulting quadrilaterals are then further refined using the previously computed gradient data. The first step of the refinement consists of marching along each side of the quadrilateral on a per-pixel basis and taking a slice from the image normal to the side. The coordinate of the maxima of this slice is then stored. Once all of the local maxima locations are computed along the side, a linear least-squares fit is computed for that side. This results in four lines per quadrilateral. The four intersections are computed from these lines, and those are stored in floating point as the exact vertex locations. Since the entire side of the fiducial is examined in aggregate, sub-pixel accuracy can be obtained. Additionally, this method is robust to peeling and/or damaged corners on the fiducials.

3.1.4.2 Model Tracking

At this point, the locations of the fiducial vertices are known in both model space and in image-sensor space. However, each vertex in model space must still be matched to its corresponding vertex in image-sensor space. Since the fiducials are not labeled, they must be identified by their relative location. This is complicated by the fact that the model is currently in a completely unknown orientation. This problem can be broken into two separate sub-problems. First, the three fiducials must be identified. Second, each vertex of each fiducial must be identified relative to the fiducial itself.

In general, there are six permutations mapping three fiducials to between the two systems. If the convention of numbering the fiducials counter-clockwise about their collective centroid is assumed, the number of possible mappings is reduced from six to three since the fiducials cannot be viewed through the back of the model. Next, the affine transform

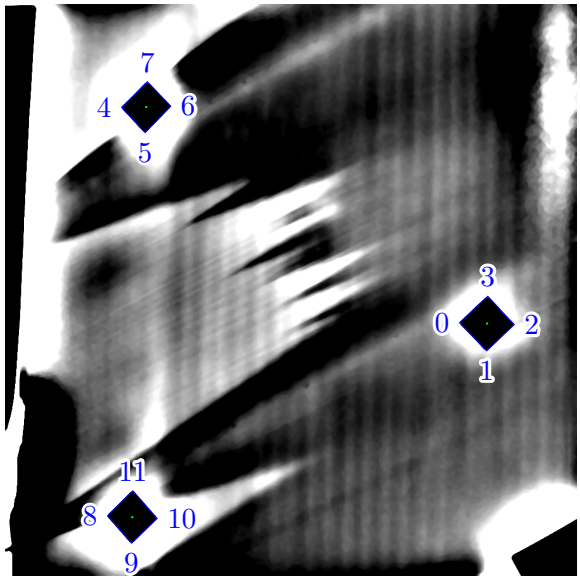

Figure 3.5: Filtered fiducial tracking image with fiducials in arbitrary order

is computed that maps the three fiducials from the image coordinates of their centroids, to the known span/chord coordinates for each of the three remaining permutations. If the sum of the products of the square portion of the affine matrix is taken for each of the three transforms, the value will only be positive for the case where the spanwise leg of the triangle formed by the three fiducials is within $\pm 45°$ of the spanwise direction. This value will only be positive for one of the remaining permutations, provided that the first two fiducials are approximately vertical with respect to each other within the camera frame. Given that one constraint on camera placement, the fiducials are now identified. The result is shown overlaid on the image in Figure 3.6.

Each individual fiducial has 24 possible permutations mapping the four vertices between the two systems. If the vertices are defined to be numbered counter-clockwise about the individual fiducial's centroid, similarly to the fiducials themselves. The number of permutations is thereby reduced from 24 to 4. Next, an arbitrary permutation is chosen for each of the fiducials. The normal vector from the camera to each fiducial's centroid is then computed using the camera model. Then, the *solvePnP* function is used on each

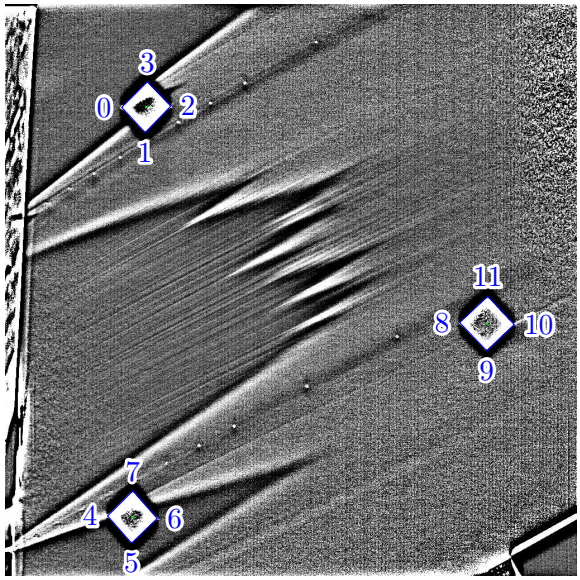

Figure 3.6: Image with fiducials ordered

fiducial individually. Since a random permutation of the four viable options was chosen, the rotation matrix is likely incorrect, and the translation vector is likely in the wrong coordinate system. However, the magnitude of the translation vector will be correct due to the fact that the fiducial is only incorrect by a rotation. The magnitude of each fiducial's translation vector is then applied to the respective normal vectors. This corrects the rotation, and gives a good estimate of the location of the three fiducials in three-dimensional camera coordinates. The Triad method is then applied to the three fiducials to obtain an estimate rotation matrix. Next, the rotation matrix is calculated for each of the four permutations for each of the fiducials individually. Whichever of the four permutations that results in the closest match to the rotation matrix calculated by the Triad method is the the correct permutation. Once this step is complete, each vertex in the image is matched to its corresponding coordinate in model space, as shown in Figure 3.7.

At this point, *solvePnP* is used one remaining time to solve for all 12 coordinate pairs simultaneously. This gives the final, refined translation and rotation values. The model location, and thereby the full non-linear transform from image sensor coordinates to model

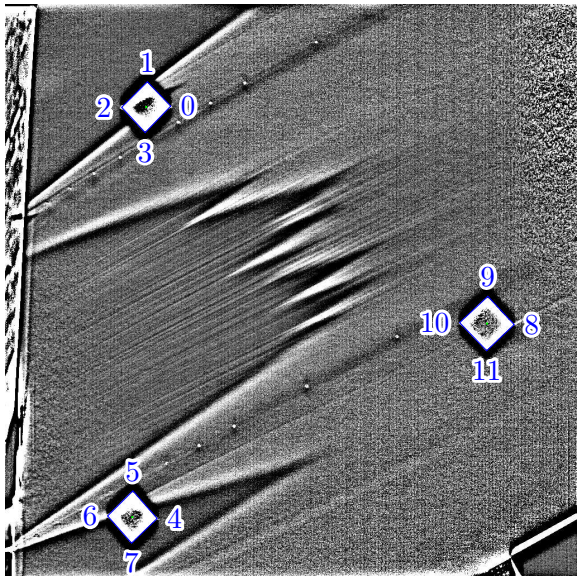

Figure 3.7: Image with fiducials and verticies ordered

coordinates is now known.

3.1.4.3 Undistortion

Once the full transform is computed, the next step is to use it to undistort the image from the sensor. First, a uniform grid of desired span/chord points is chosen. For SWIFTER/SWIFTEST a grid at 0.5 mm pitch between 205 mm and 1029 mm in the streamwise direction, and ±203 mm along the span ±234 mm measured parallel to the attachment line) is chosen. This grid pitch was chosen to be a round number slightly smaller than the finest physical pixel pitch on the model (~ 0.9 mm in order to interpolate, rather than decimate, the sensor data. This grid of coordinates is then transformed using the camera model in order to obtain a grid of coordinates in image sensor coordinates. The output image is then generated by retrieving the interpolated sensor value at each of the grid points. Lanczos resampling is used to perform the interpolation.

Figure 3.8 shows an example un-cropped undistorted image from flight on the left, and the wind tunnel on the right. Even though the flight configuration has a relatively straight view of the model at optimal range, there is still a fairly visible amount of distortion. The

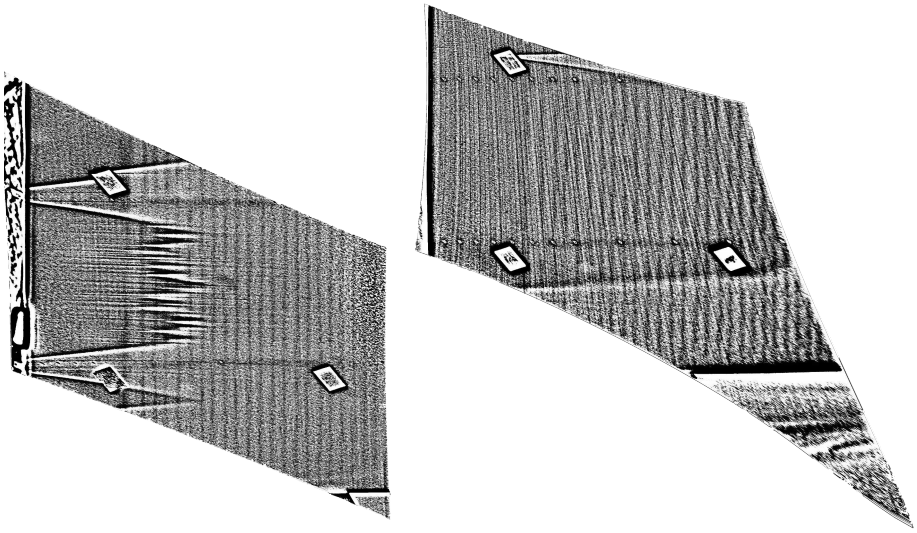

Figure 3.8: Sample flight (left) and wind tunnel (right) undistorted images

wind tunnel corrections show a significantly more extreme case. Due to tunnel geometry constraints, the camera must be placed close to the model, at an oblique angle, with a wide angle lens. This results in images that are difficult to orient by eye due to the heavy distortion, but makes little difference to the automated undistortion algorithm presented. In either case, the result is an accurate, distortion-free image.

3.1.5 Transition Detection

Now that a clean image with uniform pixel spacing in span/chord coordinates has been obtained, a copy is made, which will be operated on for transition detection. First, the image is histogram equalized. This operation linearizes the cumulative distribution function (CDF) of the histogram, which in effect provides a non-linear, but still monotonic, mapping from percent shear stress into a normalized zero to one intensity value. The main benefit of this operation is that it strongly enhances small gradients in the image, making the

transition front much easier to detect. Next, the result is median filtered and low-passed at on the order of a 2 mm cutoff wavelength. This is done to even further remove any residual sensor noise since the next step (Sobel gradient) is highly sensitive to high frequency noise. Additionally, there is no worry of destroying useful small features in the image at this point due to the fact that the operations are currently being performed on a copy, and the only feature currently of interest is the transition front, which occurs on a much longer scale. The Sobel gradient of the image is then taken in both the x_{fs} (streamwise) and z (spanwise) directions, giving an approximation of the vector gradient of the image. The result is then projected onto the characteristic transition propagation direction(s). For crossflow in the favorable pressure gradient present on SWIFTER, this is approximately $\pm 10°$. For T-S dominated transition, 90° would be a pragmatic choice. Alternately, a polar function selecting for both 90° and $\sim \pm 7°$ (depending on pressure gradient) may be necessary in order to select for both T-S and for breakdown due to bypass or other phenomena. The easiest way to find the desired value is to retrieve a raw image, and measure the propagation angle of the phenomena of interest directly. This technique will function well as long as the measurement is within several degrees of the true characteristic angle(s) for the test conditions of interest. The purpose of this projection is to heavily select for any gradients related to the transition front, and suppress all other gradients. In practice, for cases such as crossflow where there are two characteristics (positive and negative), the absolute value of the z gradient is taken, and the positive projection is then used, thereby selecting for both characteristics. The top image of Figure 3.9 shows an example output of this process.

The high intensity values of this result are likely to be locations of transition. However, there is also a fair degree of noise and interference from features such as exhaust flare and sun reflecting off the model. Since these effects have been reduced by choosing an appropriate model coating, the highest intensity points will correspond to transition locations with high certainty. These points are marked as likely transition locations, and any point between and upstream or downstream of the characteristic lines cast by turbulent wedges, plus some offset to account for any uncertainty in the characteristic lines, is reduced in

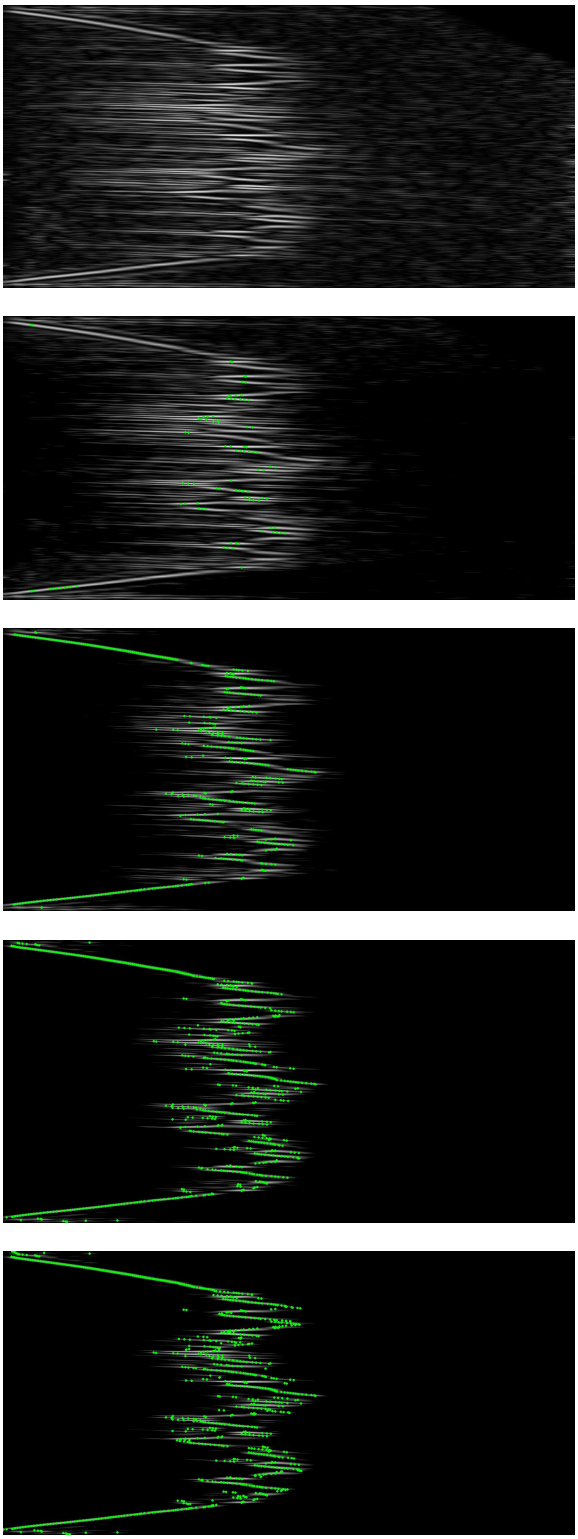

Figure 3.9: Transition detection at five selected iterations

intensity as transition is unlikely in those areas. The process is repeated for successively lower intensity points, until the transition front is fully defined. Figure 3.9 shows this process from top to bottom at five uniformly spaced iterations. For clarity, the chosen high intensity points are shown highlighted in green. As the images progress from top to bottom, the penalizing of regions inside the characteristic lines of the previously selected points is visible as a significant reduction in intensity of those regions. It should be noted that if T-S is of interest, the characteristic lines cast by turbulent wedges should still be chosen in case there is some unintended trip in the flow. Once a full transition front is obtained, a mild median filter is applied to remove outliers where some feature other than the transition front was selected.

3.1.6 Human Readable Image Generation

At this point, processing of the images into a quantitatively usable state is complete. The images are spatially co-located to sup-pixel precision, allowing multiple images at similar conditions to be averaged together to remove sensor noise without compromising the clarity of the physical phenomena. Additionally, the magnitude of the images is equivalent to the local variation in shear stress. This allows for multiple useful measurements. One example is spatial FFTs with meaningful relative amplitudes that can be used to measure growth rates of crossflow. High and low speed streaks from isolated roughness are also clearly visible, and can be measured as well.

Visually, the resulting images no longer exhibit a distinction between the laminar and turbulent regions due to the effective low-passing of the image during the conversion to local percent-variation in sheer stress. Instead, there is a sharp rise in the local variation in shear stress as the transition location is approached, followed by a sharp drop after transition occurs. While this is useful when processing the images quantitatively, an image with the DC component added back in is more visually intuitive. In order to generate an approximation of this DC component, the transition front is used to generate an image where the laminar region is zero and the turbulent region is a value chosen to correspond with the approximate difference in the shear stress between the laminar and turbulent

regions. This image is then low-passed with the parameters previously used to high-pass the original image. The result is then added to the original images depicting the local variation in sheer stress. The result is an image that still depicts an accurate variation in local sheer stress, but also includes an approximation of the global sheer stress variation, making the image visually intuitive. These images have a dynamic range significantly higher than the human eye can perceive, let alone be represented by a 16-bit image. To map these values from their floating point representations to a 16-bit grayscale value, while visually preserving the high dynamic range, histogram equalization is utilized once again. This serves to enhance small variations in the image, such as crossflow streaking, while keeping the already strong gradients near transition acceptably strong.

Bursts of 20 processed images are then taken at each test point at constant conditions and averaged together. Since the camera and model are vibrating, the camera view will vary. Due to the undistortion process, any real features inherent to the model or flow remain spatially fixed. However, any features inherent to the camera sensor itself, such as static sensor noise, will move with the camera. This average, therefore has the desirable effect of washing out the noise, but leaving the physical phenomena intact. Furthermore, since the images are co-located to sub-sensor-pixel-size precision, when the images are interpolated onto the finer grid, and then averaged together, features smaller than individual sensor pixels can be resolved. This technique is called superresolution, and is also suitable for use on the non-human-readable images. Figure 3.10 compares a single processed IR image to the corresponding averaged burst of 20 images. In the unaveraged (top) image, there is a significant amount of high frequency sensor noise apparent, which results in the image appearing much more muted. The high frequency noise also somewhat obscures the crossflow streaking. In the averaged image (bottom), much of the noise is eliminated by the averaging, resulting in a much clearer image, including finer details of the crossflow streaking.

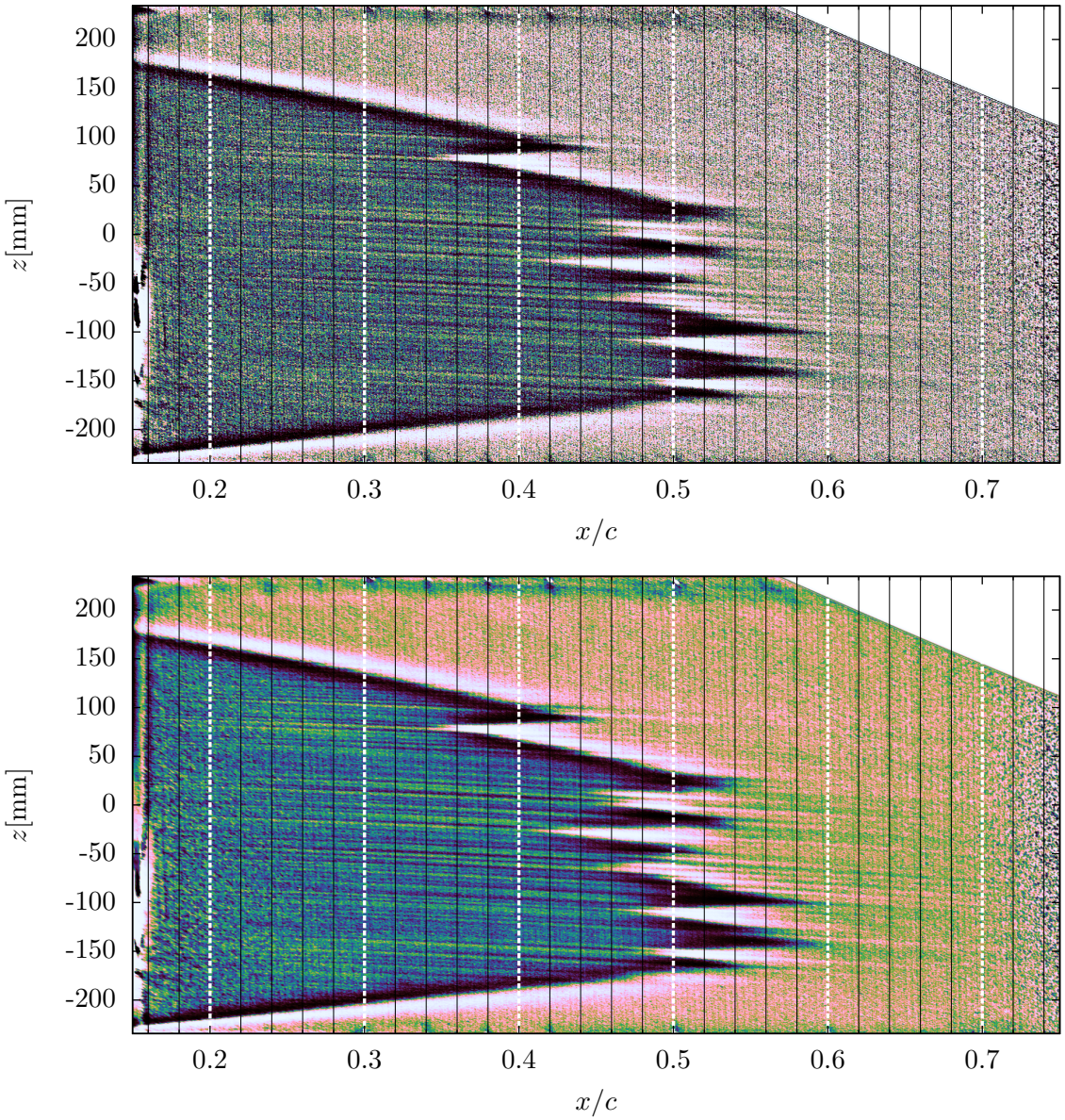

Figure 3.10: Example single processed IR image (top) compared to averaged burst of 20 images (bottom)

3.1.7 Statistical Quantification

Once a transition front has been located as a function of span, one of the most basic measurements desired is a single representative transition location. This allows different conditions to be compared by a single number. The most obvious metric is a mean transition location. However, real test data frequently has imperfections such as bugstrikes that can contaminate part of the span. Since the mean considers the whole data set blindly, a single bugstrike or other similar contaminant will distort the measurement. Median is the next logical metric. It is more robust to these sorts of contaminants. However, it is still not immune.

A more robust metric is required. The probability density function (PDF) fills this requirement. The PDF can be considered analogous to the probability that transition has occurred near a streamwise location. The abscissa of the maxima of the PDF is therefore the most probable location of transition. In order to compute the PDF, the transition data is first sorted from most forward to most aft. The data are then uniformly numbered from zero to one in fractional increments. This value as a function of the transition location is called the cumulative distribution function (CDF). The derivative of the CDF is the PDF. Figure 3.11 shows the previously presented example IR image on bottom, with the corresponding PDF aligned in the top graph. The image is an averaged burst of 20 images. Transition detection is performed on each of the 20 images individually, and the individual PDFs are plotted as colored lines. Additionally, all of the transition data is combined into a single PDF, which is plotted in black. The aggregate PDF is used to compute the presented dominant transition location, while the SEM (standard error of the mean) of the results of the 20 individual PDFs is used, in conjunction with the estimate uncertainty in fiducial alignment, is then used to compute the displayed uncertainty. It should be noted that this is simply a detection uncertainty; it does not take into account any transition location uncertainty due to variation in environmental factors such as angle of attack or Reynolds number.

In the event of a contaminated data set, the resulting wedge will either stretch one of

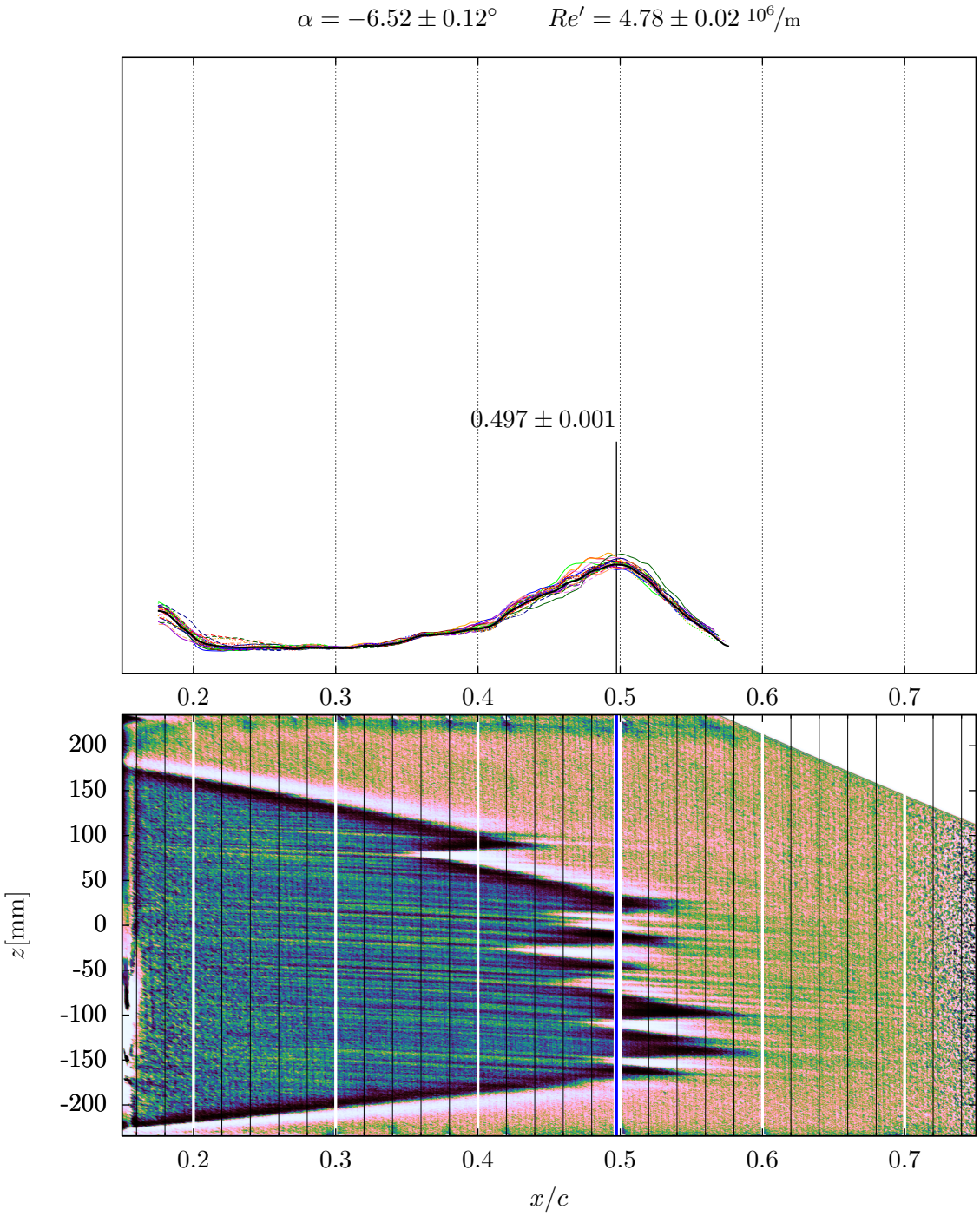

Figure 3.11: Processed IR image with PDF

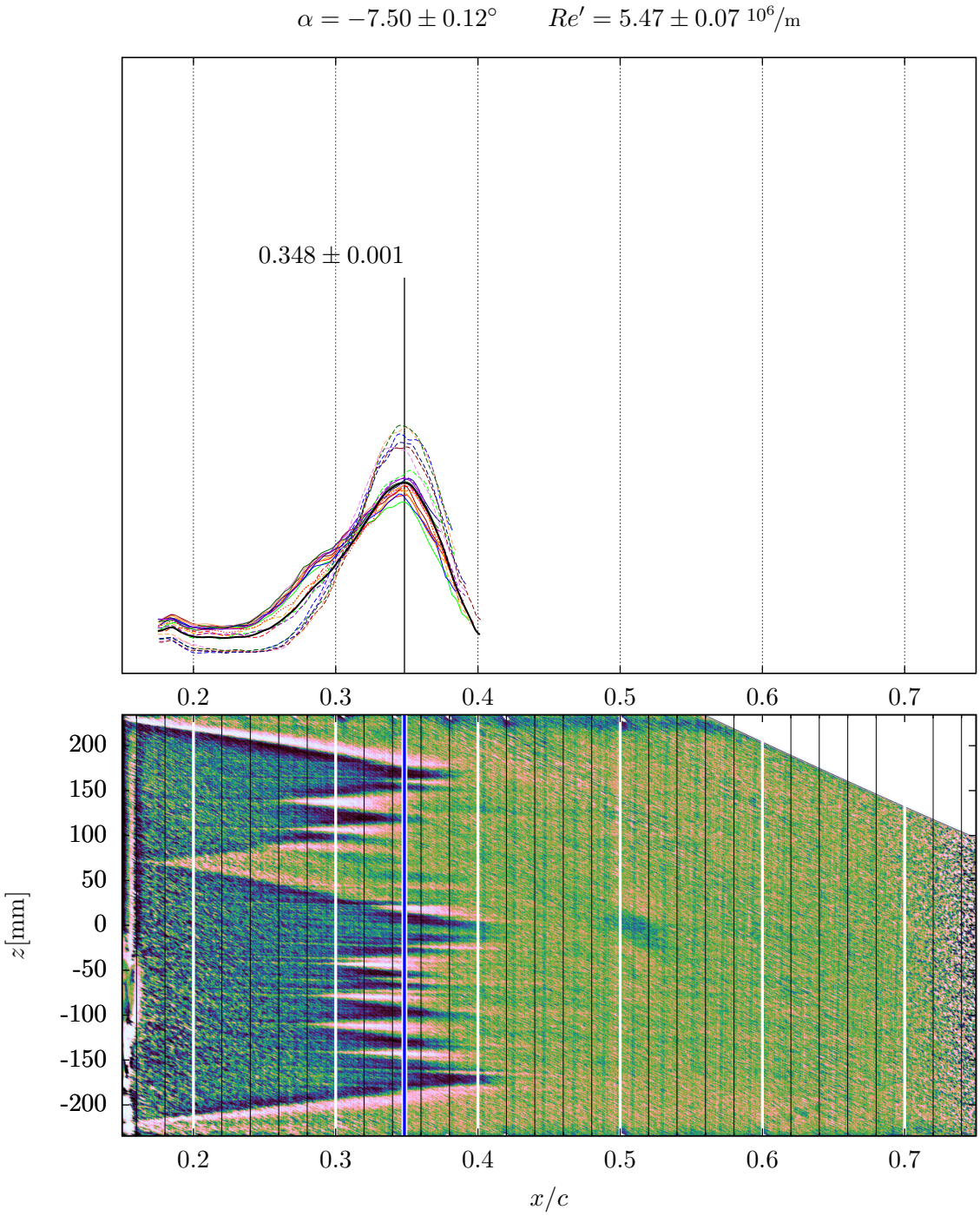

Figure 3.12: PDF with bugstrike

the tails of the function, or even induce an additional peak. However, the dominant peak remains unmoved. As such, the PDF inherently rejects contamination with no user input or bias. Figure 3.12 shows a typical IR image with a bugstrike. Visually, the center of the wedge structure is at approximately 0.34 x/c. The PDF indicates that transition occurs at 0.348 x/c, whereas the mean transition location is 0.304 x/c and the median transition location is 0.323 x/c. As to be expected, the average is heavily moved forward by the bugstrike and the median is also dragged forward to a lesser extent. However, if the clean region of $z = 0\,\text{mm}$ to $-150\,\text{mm}$ is analyzed, the mean, median and PDF all indicate a transition location of 0.346 x/c, which is agrees well with the PDF of the entire front. As such, it is highly desirable to utilize PDF for these comparisons due to its robustness to these environmental disturbances.

3.2 Hotwire Traverse

3.2.1 Calibration

In order to obtain quantitative velocity measurements from the hotwires, they must first be calibrated. A new calibration must be performed any time any connection is broken and re-mated between the anemometer and the wire itself, or any time any component is replaced. Additionally, the system drifts slowly with time, and as such, calibrations must be repeated at regular intervals. Generally, once every morning is sufficient.

Hotwires are sensitive to both velocity and temperature. Since the KSWT is not temperature controlled, the dependence on temperature must be calibrated out of the hotwires. To obtain a calibration, the hotwire traverse is moved into its calibration location in the test section. Before calibration, a pitot probe is used to measure the ratio of the local velocity at the calibration position for each hotwire relative to the permanently installed reference pitot probe that measures the tunnel freestream velocity. This accounts for any model and wall effects on the local velocity at the calibration location. All calibration velocities are compensated by these ratios to obtain the velocity at the hotwire being calibrated. This ratio only needs to be measured once per model configuration.

The calibration consists of first running the tunnel through a set of 13 RPM increments and measuring the velocity and corresponding voltage for the hotwires at each RPM. Fixed RPM is chosen to allow for quicker stabilization and acquisition of these points since the particular velocity is irrelevant. The only requirements are that the velocity is constant at each point and accurately measured, and they span the velocity range of interest. The motor is then commanded to 1000 RPM, and left at that speed for 20 minutes in order to heat up the tunnel. After 20 minutes, the tunnel is commanded to repeat the velocities measured previously from fastest to slowest. The end result is 13 pairs of points at 13 velocities. Each pair has a hot point and a cold point. Eq. 3.7 is then fitted to these data in order to obtain the a_T, b_T, and n_T coefficients. Next, Eq. 3.8 is fitted to these data to obtain the a_u, b_u, and n_u coefficients. This fully defines the hotwire calibration for both temperature and velocity. Additional detail on this calibration procedure can be found in Downs (2012).

$$c_T(u) = (T - T_{ref})\left(a_T + b_T u^{n_T}\right) \tag{3.7}$$

$$u = \left(a_u + b_u\left[E^2 + c_T(u)\right]\right)^{n_u} \tag{3.8}$$

Since the hotwire calibration for velocity depends on velocity, one cannot simply plug in a voltage, E, and obtain a velocity. Instead, a velocity is guessed. Typically the last processed velocity is kept in memory for this purpose, but the initial guess has no effect on the final solution. The velocity is then computed using this guess in the temperature calibration. The resulting velocity is then used in place of the guess, and the process is repeated. This continues until the velocity converges. These equations are well behaved and converge quickly and stably. For arbitrary guesses in velocity, the velocity converges to within machine precision in under 10 iterations. Typically only one or two iterations are necessary if the previously measured velocity is used for the initial guess when taking

subsequent measurements in the boundary layer.

3.2.2 Wall Finding

When taking boundary layer scans using a hotwire traverse system, the location of the wall is not known a-priori. Additionally, the probe cannot touch the wall as it would damage both the hotwire itself, as well as the highly polished surface of the model. During a typical boundary layer scan, the boundary layer probe is started outside the boundary layer. A set of data is then taken simultaneously from both the boundary layer and freestream hotwires. The ratio of the mean velocities between the two probes is then calculated and stored. The hotwire probe is then incremented towards the wall. At each point, the ratio between the boundary layer and freestream probes is taken and normalized by the ratio taken at the beginning of the profile. This results in the u/u_e value at that point, adjusted to account for any slight temporal variation in the freestream velocity. The increment towards the wall is then computed as a function of the current u/u_e and the desired start and end step size. This results in a clustering of points as the probe approaches the wall, providing more fidelity where the shear is higher. Once the probe reads $u/u_e < 0.20$, the profile is considered complete and the probe is returned to its position outside the boundary layer, and the process repeats for the next profile. Stopping at $u/u_e = 0.20$ avoids issues with striking the model with the probe. Values as low as $u/u_e = 0.15$ have been tested in similar configurations in this tunnel, but below $u/u_e = 0.20$, the risk of striking the wall rises dramatically. For these tests, $u/u_e = 0.20$ occurs approximately 100 µm away from the surface.

Wall finding is then performed in post-processing, after the test is complete. For each profile, the data from $u/u_e = 0.20$ to $u/u_e = 0.50$ is retrieved and a second order polynomial is fitted. For zero pressure gradient, a linear fit would be sufficient, but the proverse pressure gradient results in a slight curvature in the profile. This fit is then used to extrapolate to the point where $u/u_e = 0$, giving the approximate location of the wall. The uncertainty in this extrapolation is approximately 10 µm, which is reasonably acceptable considering that the wire itself is 5 µm in diameter.

3.2.3 Grid Scans

Each boundary layer grid scan consists of 100 boundary layer profiles taken at 1 mm increments in span, measured parallel to the leading edge, at constant x/c. The scans start 10 mm outboard of midspan and end 90 mm inboard of midspan. This corresponds to the lower portion of the traverse's spanwise travel. This region was chosen to minimize vibrations in the traverse system. Each of these profiles has approximately 40 points in the y direction inside the boundary layer, and approximately 5 points outside the boundary layer. The distribution of points is clustered towards the wall. Once the boundary layer probe reads $u/u_e = 0.20$, the profile is stopped and the traverse moves on to the next profile.

At 5% x/c, the boundary layer is on the order of 1 mm thick. At the Reynolds numbers tested, at this chordwise location, the last data point in the profile at $u/u_e = 0.20$ is only 100 µm away from the surface. If the 1.25 mm wide hotwire probe is more than that amount out of parallel with the surface, the hotwire probe will strike the surface, damaging both the hotwire and the highly polished metal surface. Since the hotwire must be aligned to the surface by hand and by eye, measurements this far forward are pushing the bounds of what is feasible. Additionally, the uncertainty in the wall finding technique on the order of 10 µm results in a significant uncertainty in the disturbance amplitudes measured. As such, no scans were conducted forward of 5% x/c, which is approximately 48 mm downstream from the step, measured normal to the step.

3.2.4 Disturbance Amplitude

Once a grid of boundary layer scans is obtained, it is useful to compute a handful of metrics to compare one grid to another. In particular, it is useful to quantify the disturbance amplitude. Locally, the steady disturbance amplitude, $\bar{a}$, is computed using Eq. 3.9. Essentially, it is the standard deviation of the local velocity at that boundary layer height and chord location. Steady disturbance amplitude is a measure of the time invariant modulation of the boundary layer in span. Similarly, the local unsteady disturbance amplitude,

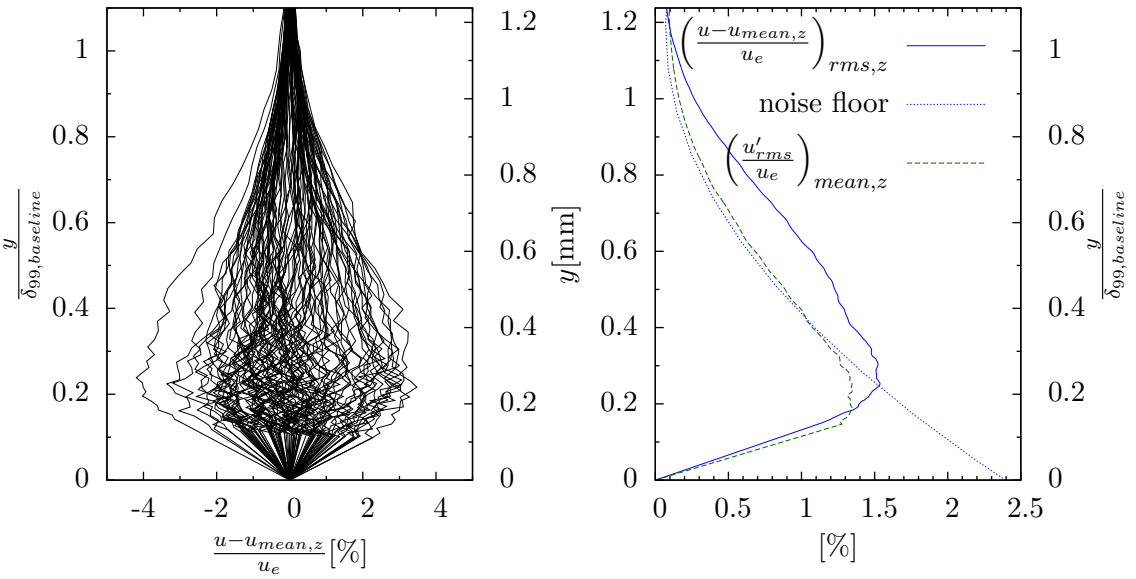

Figure 3.13: Baseline, $x/c = 5\%$, $Re' = 1.389 \times 10^6$/m

a', is computed using Eq. 3.10. The local unsteady disturbance amplitude is a measure of the local temporal fluctuation in velocity about the steady state result.

$$\bar{a} = \left(\frac{u - u_{mean,z}}{u_e}\right)_{rms,z} \tag{3.9}$$

$$a' = \left(\frac{u'_{rms}}{u_e}\right)_{mean,z} \tag{3.10}$$

An example of these calculations is shown in Figure 3.13. The left chart shows the raw percent variation of each boundary layer profile relative to the mean profile. The right chart shows the steady disturbance amplitude in solid blue along with the unsteady disturbance amplitude in dashed green. Additionally, the noise floor for the steady disturbance amplitude is shown in dotted blue. The majority of this uncertainty is due to the previously discussed 10 µm uncertainty in wall finding. The uncertainty in the measured velocity is also included, but is a relatively minor effect comparatively.

$$A = \frac{1}{\delta_{99}} \int_0^{\delta_{99}} \bar{a} \, \mathrm{d}y \tag{3.11}$$

$$N_{exp} = \ln\left(\frac{A}{A_0}\right) \tag{3.12}$$

Additionally, the local steady disturbance amplitude can be integrated, as per Eq. 3.11 to obtain the disturbance amplitude for the entire boundary layer slice. The noise floor can also be integrated in similar fashion to compute the noise floor for these integrated quantities. The integrated disturbance amplitude can be used to compute an experimental N-factor by taking the natural log of the ratio of disturbance amplitude, A, to some reference amplitude, A_0, as defined in Eq. 3.12. It should be noted that the experimental N-factor is analogous, but not identical to the computational N-factor obtained from stability calculations.

It should be noted that noise floor is a somewhat loose description of these uncertainties. It is possible to obtain measurements below the noise floor as the "floor" is based off of the typical wall-finding uncertainty. Such measurements cannot be concluded to have low disturbance amplitude, but rather have unusually low wall-finding uncertainty. This noise floor should be viewed as the approximate lower bound of trustworthy measurements.

4. RESULTS

The results are broken into two regimes, flight and wind tunnel. The flight regime spans Reynolds numbers from $3.7 - 5.7 \times 10^6$/m. For the flight environment, IR thermography is the only boundary-layer diagnostic utilized. The wind tunnel results span $Re' = 1.0 - 1.6 \times 10^6$/m, and utilize both IR thermography and the hotwire traverse.

4.1 Flight

In the flight environment, a total of 13 shim heights were tested: the zero step, eight aft-facing steps, and four forward-facing steps. The specific steps tested are listed in Table 4.1. These configurations were chosen to bracket the region of useful test data. The majority of laminar flow is preserved for the two smallest steps ($-128\,\mu$m and $192\,\mu$m), while at the two largest steps ($-469\,\mu$m and $533\,\mu$m), the flow transitions to fully turbulent near the minimum valid Reynolds number of 4.0×10^6/m. Below $Re' = 4.0 \times 10^6$/m, the effective sweep angle of the model drops below 28°, due to the lower freestream velocity requiring a higher aircraft angle of attack to maintain the proper descent rate. As such, flight testing at lower Reynolds numbers is avoided. The upper bound on Reynolds number is fixed by the maximum operating airspeed of the aircraft. The intermediate steps were chosen to fill the matrix as uniformly as possible, while using as few shims as possible in order to minimize the step height uncertainty. Additionally, thin shims were avoided due to practical concerns with shim durability and repeatability. More aft-facing steps were tested than forward-facing steps, because the aft-facing steps were tested first. The initial data from the aft-facing steps was then used to make a more educated decision on which forward-facing steps would yield the most useful results, resulting in a more efficient test matrix for the forward-facing steps.

4.1.1 Critical Step Height

In the flight environment, two distinct regimes are apparent. Below a certain critical step height, as the step height is increased, the transition front slowly moves forward, and

Table 4.1: Shim configurations tested in flight

thickness 10^{-3} in	thickness µm	k µm	σ_k µm	n	shim list 10^{-3} in
-22	-559	-469	7	2	020 020
-19	-483	-406	7	2	018 025
-17	-432	-363	7	2	020 025
-13	-330	-277	7	2	018 031
-12	-305	-256	7	2	025 025
-11	-279	-234	7	2	020 031
-8	-203	-170	7	3	018 018
-6	-152	-128	7	2	025 031
0	0	0	7	2	031 031
9	229	192	7	3	020 020 031
14	356	299	7	3	020 031 025
18	457	384	7	3	018 031 031
21	533	448	7	4	018 025 020 020

increased crossflow streaking is observed in the IR images. Above a certain step height, transition rapidly moves forward of 15% x/c. When this occurs, the tip transitions first, and over the span of approximately 0.2×10^6/m in Re', the turbulent region envelopes the entire span. An example of this spanwise non-uniform transition front is shown in Figure 4.1. The non-uniform transition is believed to be a result of the slight spanwise non-uniformity of the pressure gradient in flight. Since all reference boundary layer properties are referenced to mid-span, Re_{kk} is considered critical when the transition front passes midspan. This critical Re_{kk} was found to exhibit a mild trend in freestream Reynolds number, and a moderate trend in angle of attack. These critical points are plotted in Figure 4.2, along with contours from a planar fit in both freestream Reynolds number and angle of attack.

As angle of attack is increased, the critical behavior appears to be destabilized. Since the step location is very far forward on the airfoil, the increasing negative angle of attack counter-intuitively corresponds to a less favorable pressure gradient. This is shown graphically in Figure 4.3. As such, it appears that at an increase in pressure gradient is

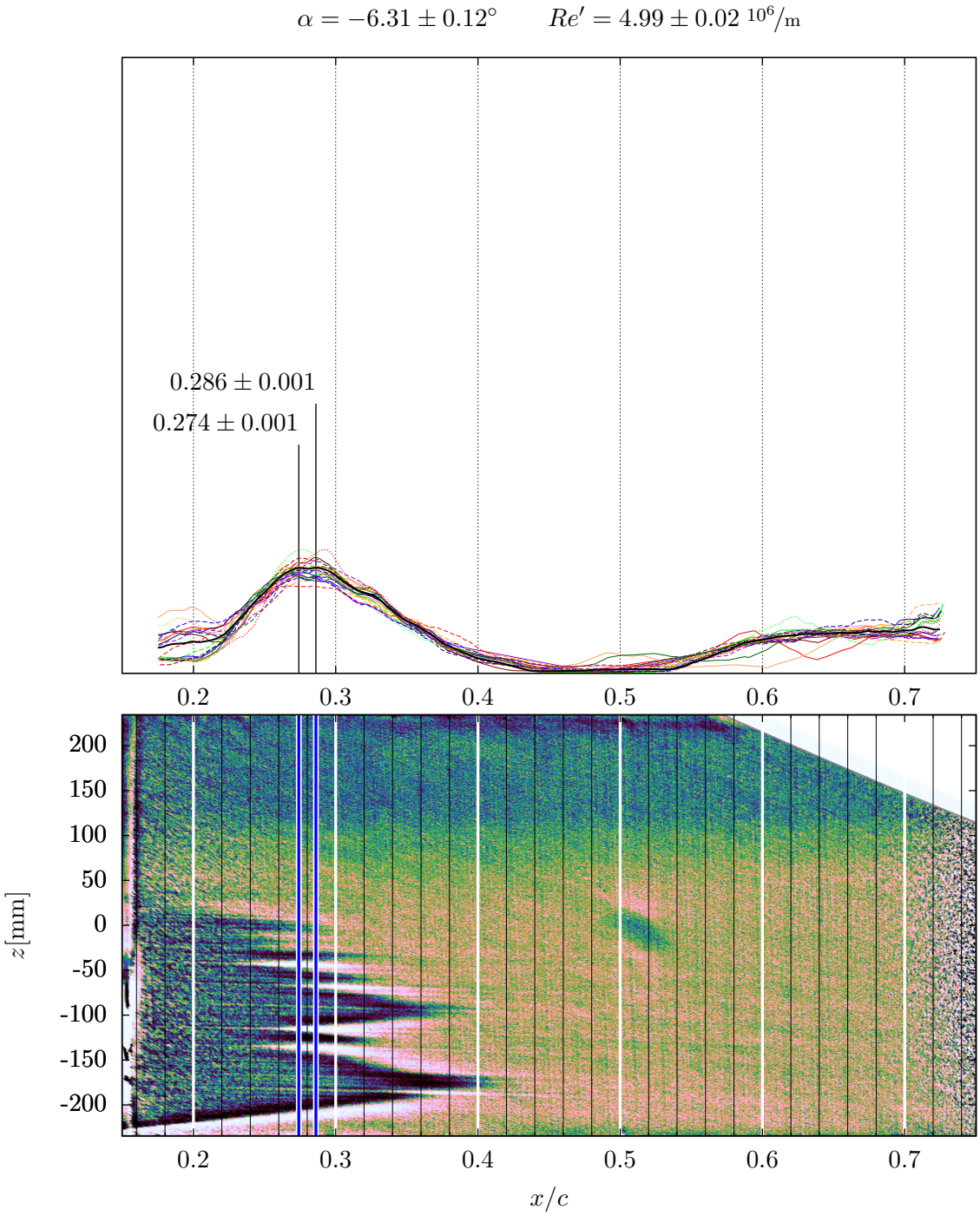

Figure 4.1: Example critical IR image

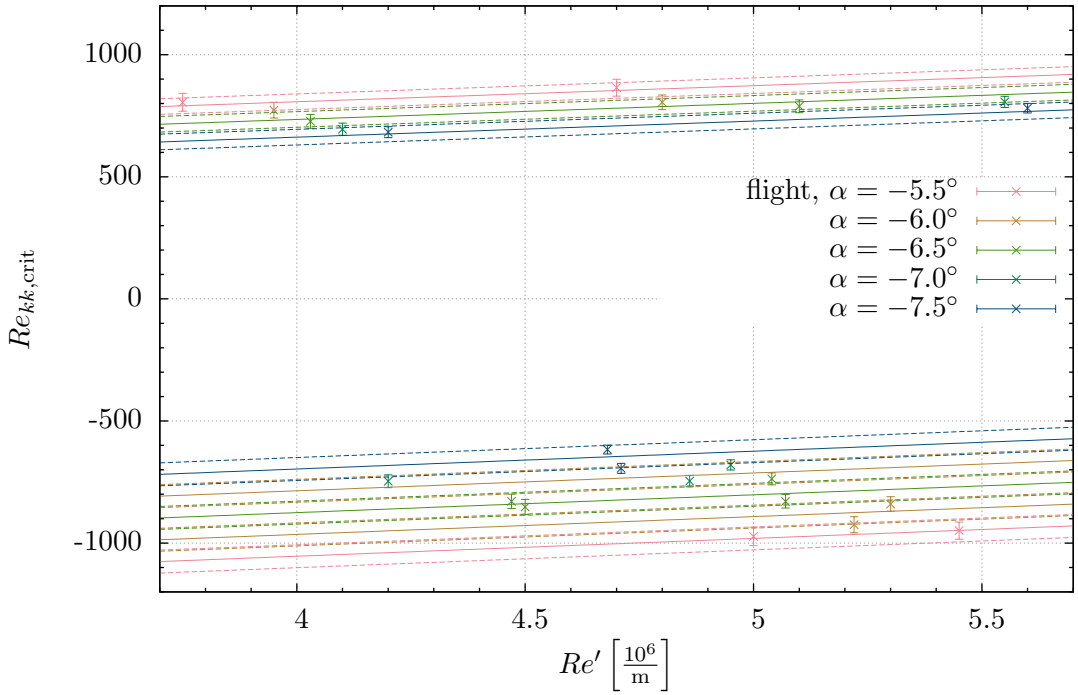

Figure 4.2: Critical step height in flight

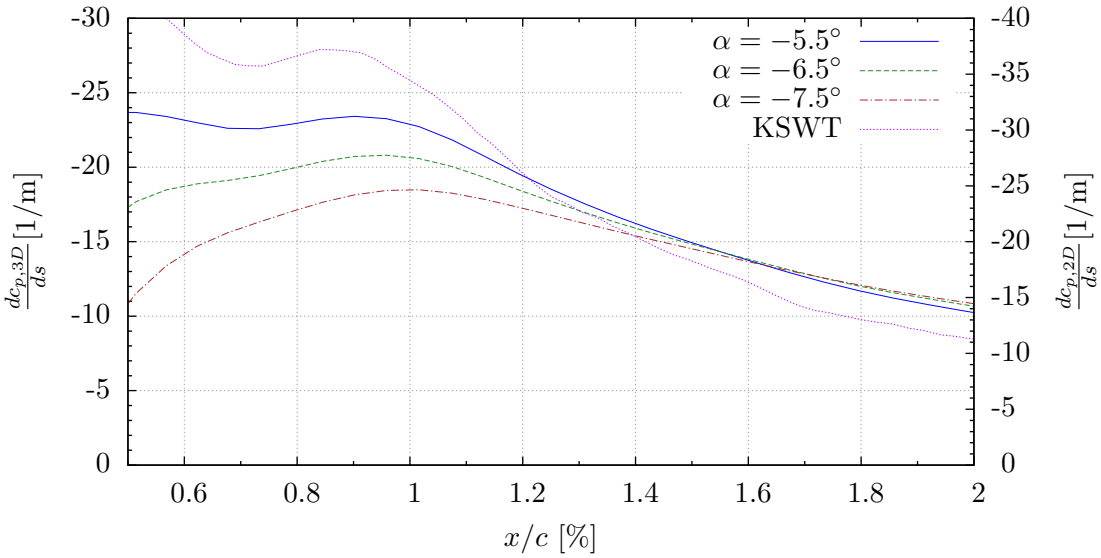

Figure 4.3: Local pressure gradient near 1% x/c

stabilizing.

4.1.2 Subcritical Behavior

In the subcritical regime, transition moves slowly forward of the baseline transition location. As the transition front moves forward, crossflow streaking becomes increasingly strong in the IR images. Figure 4.4 shows a fully laminar baseline image. Figure 4.5 shows an image at similar conditions with an aft facing step of 299μm. In Figure 4.5, dramatically more crossflow streaking is visible, and transition has moved into the test area. In order to quantify this effect, a second order surface as a function of Reynolds number and angle of attack was fitted to the baseline transition location. For each data point at a non-zero step, the baseline transition location is then retrieved from the curve fit and used to normalize the transition location. This is defined as the laminar fraction, which varies from zero to one, where zero indicates no laminar flow remains, and one indicates that the transition location is the same as the baseline configuration. Figure 4.6 shows a plot of the resulting laminar fraction as a function of Re_{kk} and Re' for a single α slice of $-6.5 \pm 0.25°$. Appendix A contains the full data set of all five α slices, ranging from $-5.5°$

to $-7.5°$ in $0.5°$ increments. In the figures, there are several subcritical data outside the critical lines. This is due to the fact that, for these points, the midspan region has fully tripped, but there are still enough untripped data beyond midspan to discern a reliable transition front. As angle of attack is made increasingly negative, the subcritical behavior is further destabilized. Additionally, freestream Reynolds number appears to have a slight destabilizing effect on the subcritical transition behavior.

4.2 Wind Tunnel

In the wind tunnel environment, 12 step heights were tested: zero step, three aft-facing steps, and eight forward-facing steps. The specific steps tested are listed in Table 4.2. The limiting factor on the low Reynolds number bound is the step capability of the model, at $-1575\,\mu m$ and $2362\,\mu m$ for forward and aft steps, respectively, measured normal to the chord line. These amount to 5% and 7.5% of the local thickness of the model, respectively. For larger steps, the implicit assumption of an undisturbed airfoil shape would be implausible. There is no utility in testing much below the critical Reynolds number at these steps since the flow ceases to be meaningfully modulated by the excrescence. The upper bound on Reynolds number in the wind tunnel is fixed by the maximum operating RPM of the KSWT's fan.

4.2.1 Critical Step Height

In the wind tunnel, there is a similar critical step height where transition suddenly moves forward. However, rather than transitioning steadily from tip to root as seen in the flight environment, turbulent wedges begin flickering throughout the IR image. As Re_{kk} is increased, the flickering becomes more frequent and more pervasive throughout the entire test region, finally resulting in a fully turbulent test region. The critical step height is defined as the Re_{kk} at which the onset of flickering turbulent wedges occurs. The critical Re_{kk} as a function of Re' is shown in Figure 4.7.

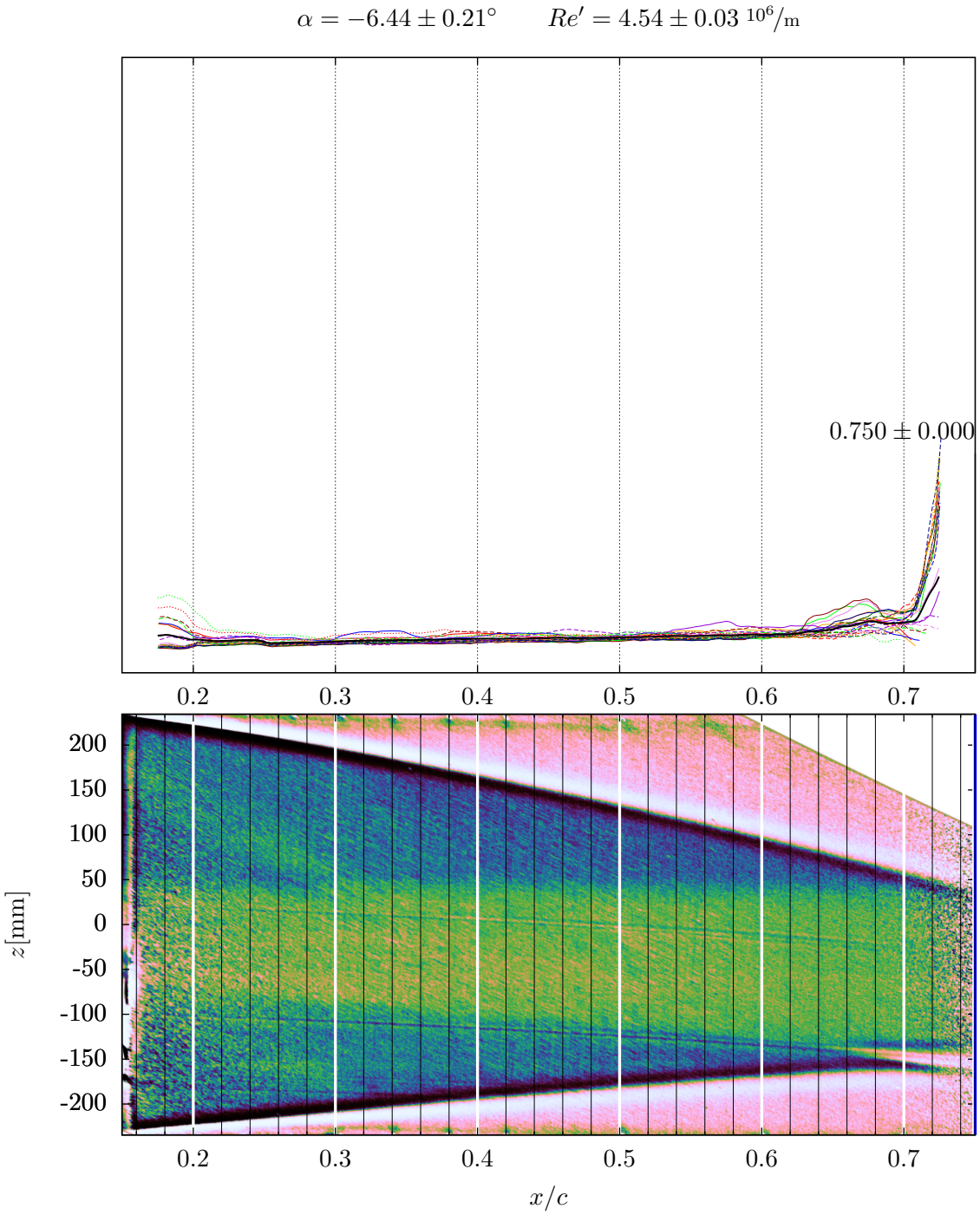

Figure 4.4: Example baseline IR image

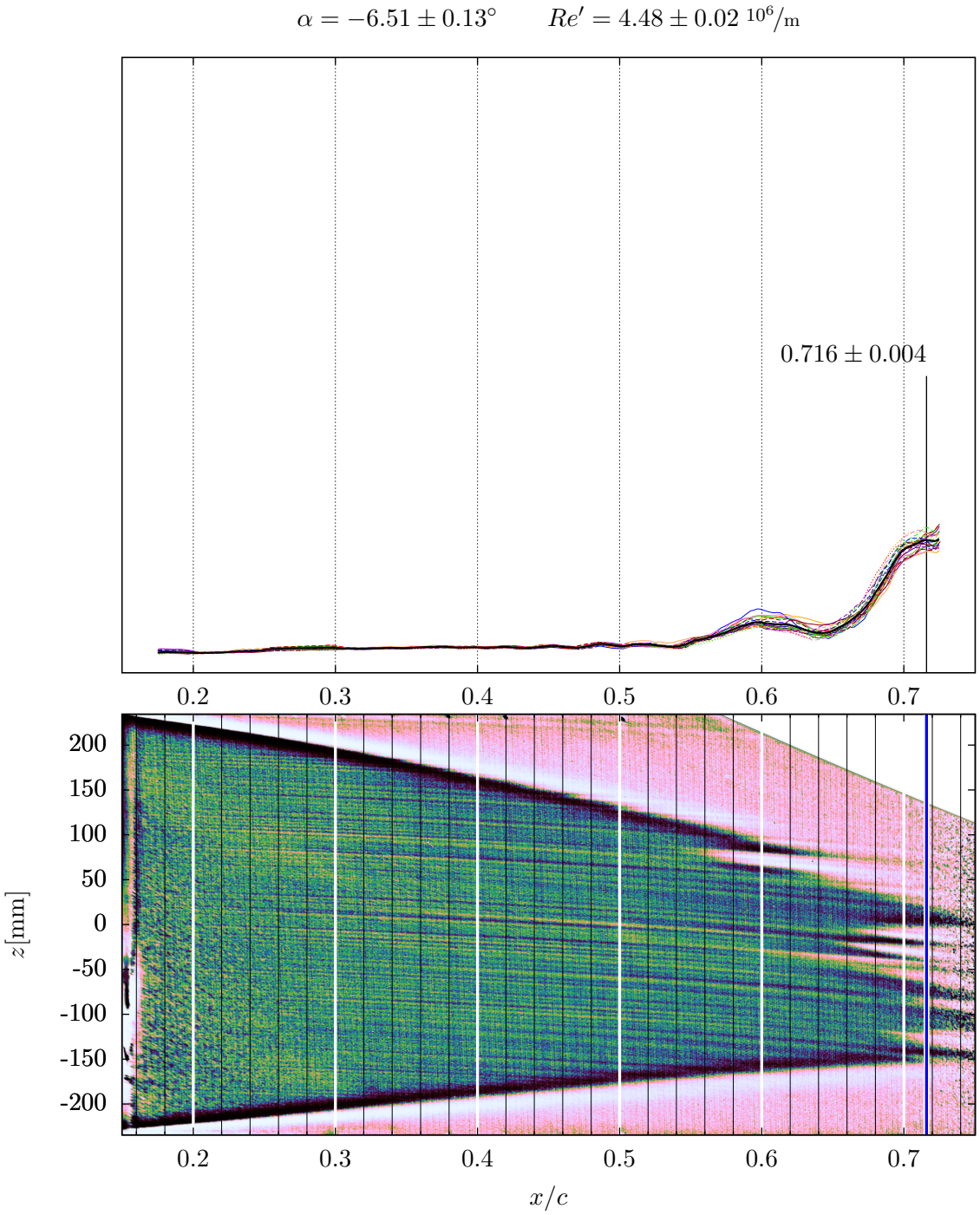

Figure 4.5: Example subcritical IR image

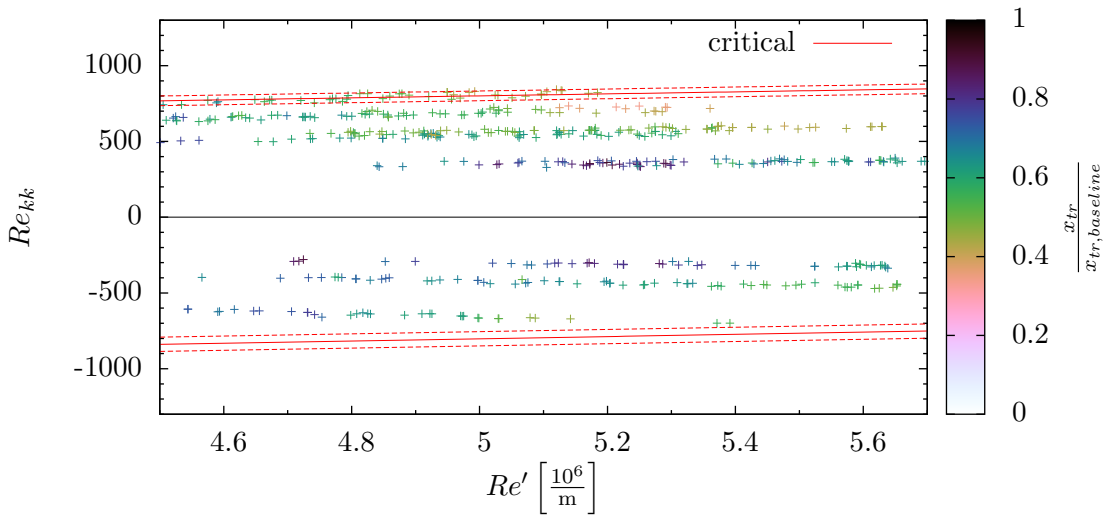

Figure 4.6: Transition fraction at $\alpha = -6.5°$

Table 4.2: Shim configurations tested in the KSWT

thickness 10^{-3} in	thickness µm	k µm	σ_k µm	n	shim list 10^{-3} in
-62	-1575	-1323	7	0	
-57	-1448	-1216	7	1	005
-52	-1321	-1109	7	1	010
0	0	0	7	2	031 031
56	1422	1194	7	4	025 031 031 031
62	1575	1323	7	4	031 031 031 031
67	1702	1429	8	5	018 018 031 031 031
71	1803	1514	8	5	020 020 031 031 031
76	1930	1621	8	5	020 031 031 031 025
82	2083	1749	8	5	020 031 031 031 031
87	2210	1856	8	5	025 031 031 031 031
93	2362	1983	8	5	031 031 031 031 031

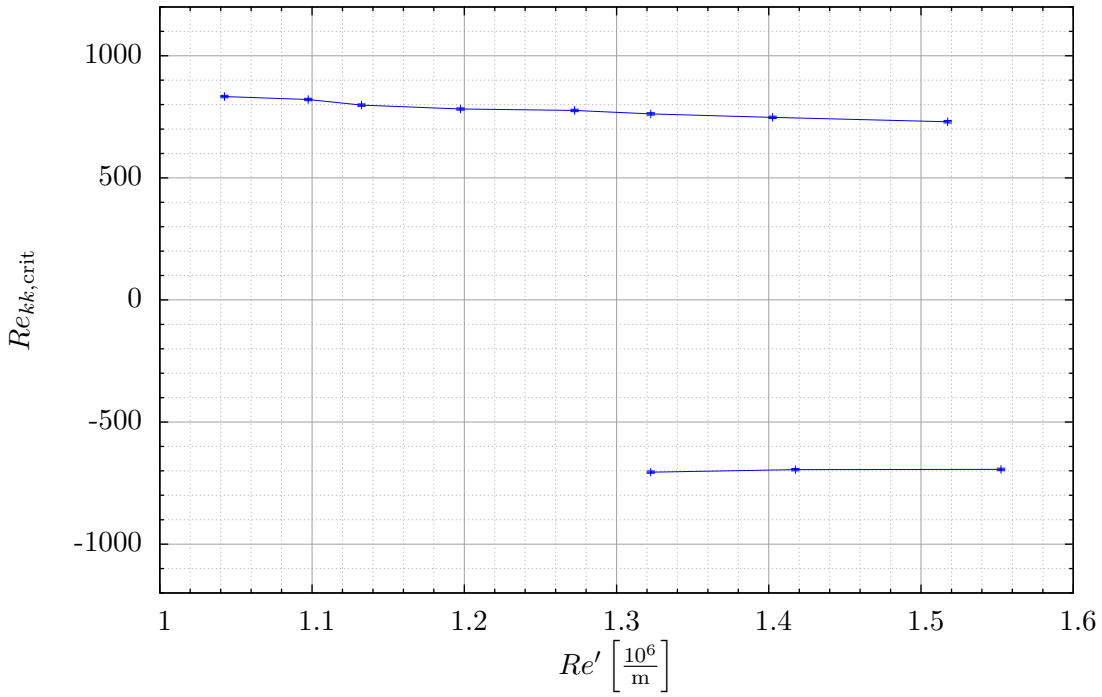

Figure 4.7: Critical step height in the KSWT

4.2.2 Subcritical Behavior

Before the onset of turbulent flickering wedges at the critical step height, no transition movement is observed in the IR thermography. Additionally, no streaking or other indication of instability is apparent in the IR images. In order to further examine the subcritical behavior, the hotwire traverse was used to map out the boundary layer. The first hotwire scan was completed at 90% of the $Re_{kk,crit}$ at 14% x/c for a 1323 µm forward-facing step. No significant boundary layer modification was observed. As such, all subsequent testing was completed at 99% of $Re_{kk,crit}$. It is not possible to test closer to $Re_{kk,crit}$ due to the fact that the uncertainty would overlap the critical region, causing intermittent turbulent wedges that would corrupt the measurements.

Figure 4.8 shows the baseline disturbance amplitudes at 5% x/c, as calculated using the techniques described in Section 3.2.4. Figures 4.9 and 4.10 show the corresponding profiles with a forward and aft facing 1323 µm step respectively. Both of the step configurations are at $Re_{kk}/Re_{kk,crit} = 0.99$, which corresponds to $Re' = 1.389 \times 10^6$/m for the forward facing case and $Re' = 1.306 \times 10^6$/m for the aft facing case. The baseline and aft facing steps show a steady disturbance amplitude near or below the noise floor. However, the forward facing case exhibits a small but measurable elevation above the noise floor. By 7% x/c the forward-facing steady disturbance amplitude has decayed back to near the noise floor, as shown in Figure 4.11. All of the hotwire scans are presented together in Appendix B. In all scans, the unsteady disturbance amplitude is positively correlated with freestream Reynolds number, but is unaffected by the step.

In order to compare these results in a more quantitative fashion, the integrated steady disturbance amplitudes are plotted as a function of x/c in Figure 4.12. As indicated previously, the largest forward facing step at 5% x/c has a disturbance amplitude mildly elevated above the noise floor, and all other points are near or below the noise floor.

Boundary layer thickness was also computed at each configuration and normalized to the δ_{99} obtained from the baseline CFD solution. Figure 4.13 shows these data plotted as a function of x/c. All of the scans match the CFD solution quite well. The only discrepancies

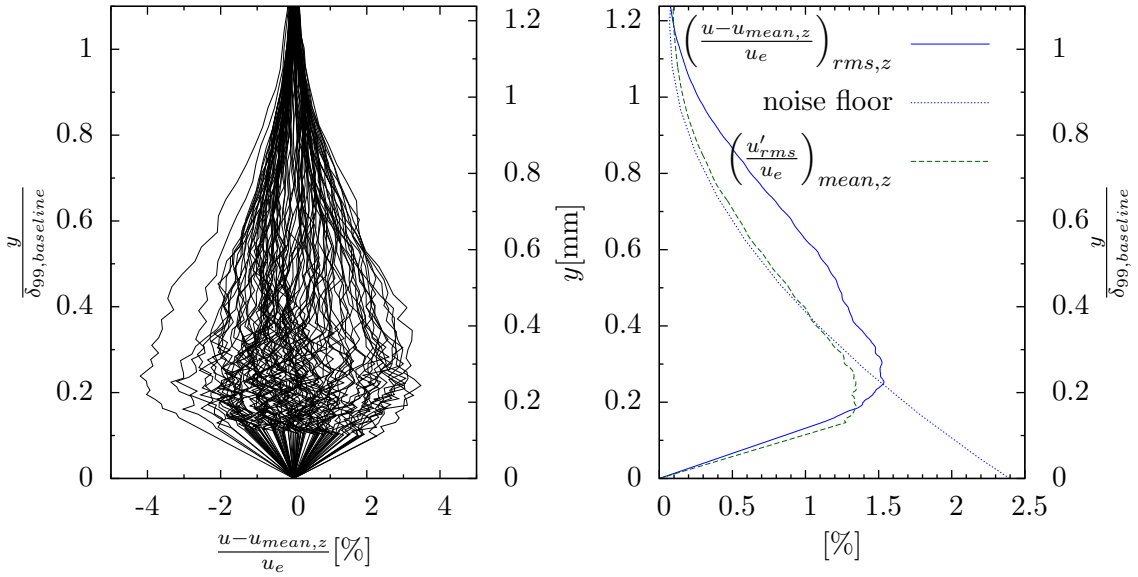

Figure 4.8: Baseline, $x/c = 5\%$, $Re' = 1.389 \times 10^6/\text{m}$

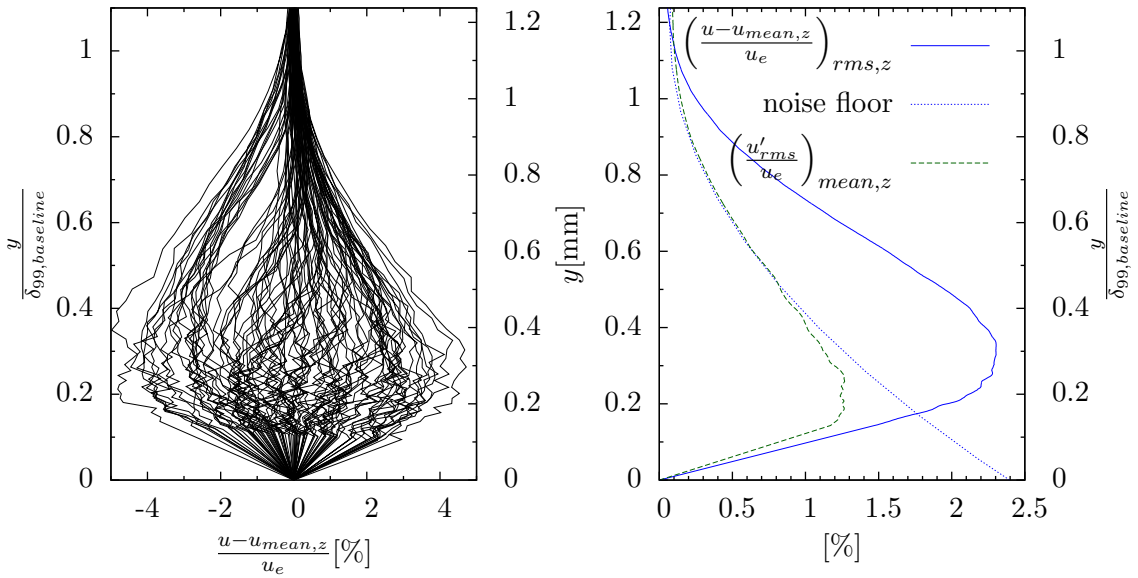

Figure 4.9: Forward-facing step, $k = 1323\,\mu\text{m}$, $x/c = 5\%$, $Re_{kk}/Re_{kk,crit} = 0.99$

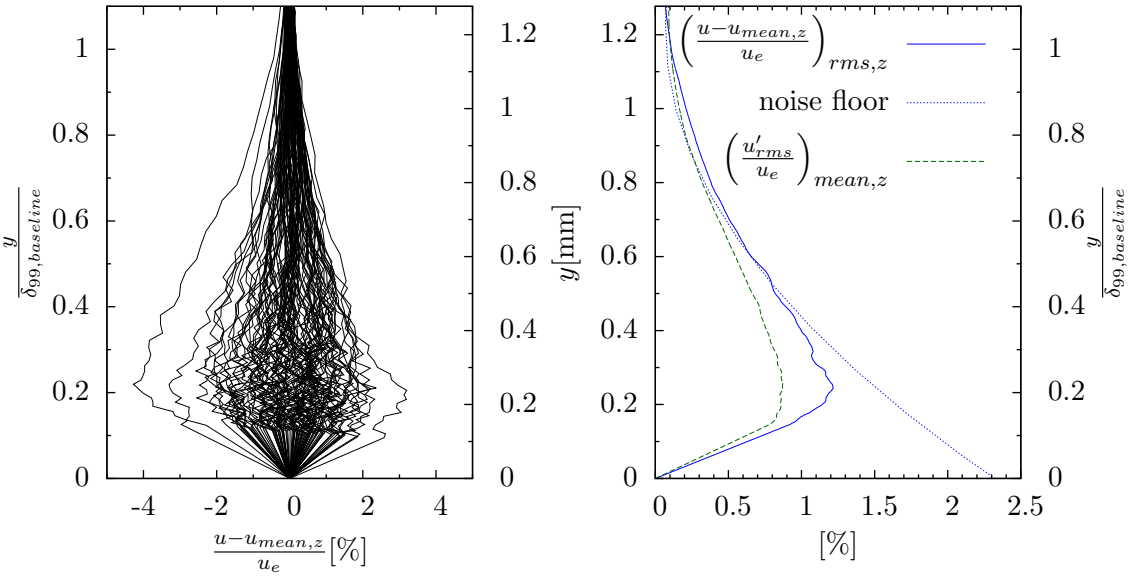

Figure 4.10: Aft-facing step, $k = -1323\,\mu\text{m}$, $x/c = 5\%$, $Re_{kk}/Re_{kk,crit} = 0.99$

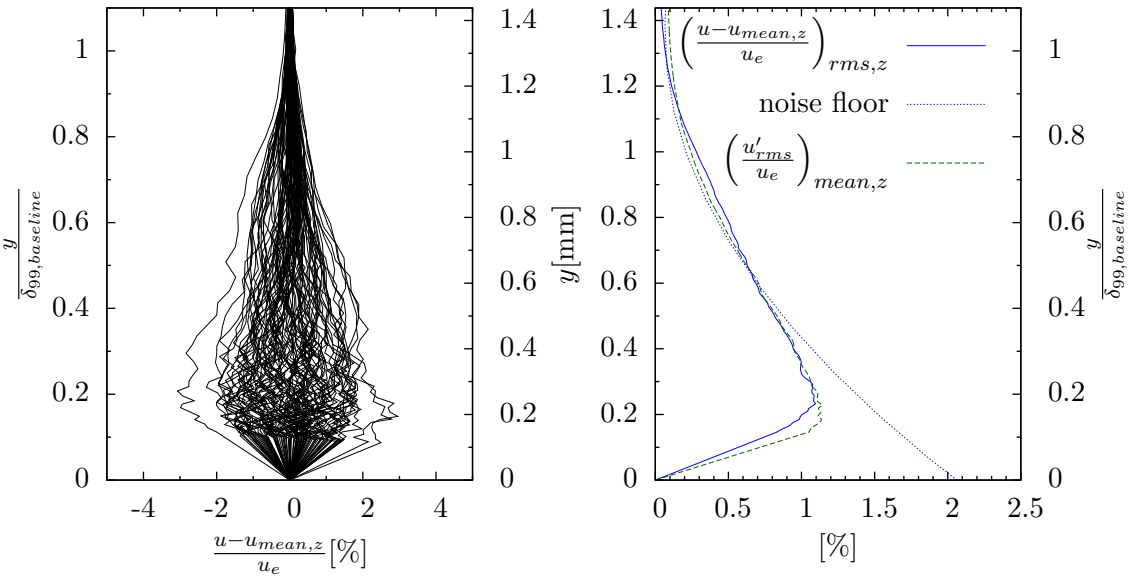

Figure 4.11: $k = 1323\,\mu\text{m}$, $x/c = 7\%$, $Re_{kk}/Re_{kk,crit} = 0.99$

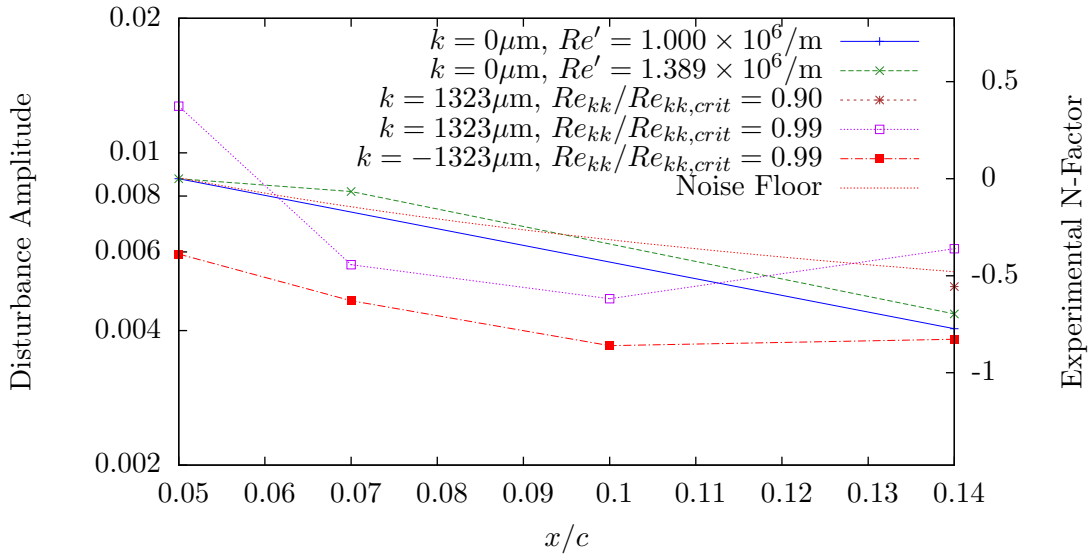

Figure 4.12: Disturbance amplitude vs x/c

are the slight thickening of the boundary layer at 5% x/c for the aft facing case, and a slight thinning of the boundary layer for the forward facing case at 5% x/c. By 7% x/c, the boundary layer has returned to baseline for both cases.

4.2.3 Acoustic Testing

Sensitivity to acoustical disturbance was also tested. A 1323 µm aft-facing step was tested at $Re_{kk}/Re_{kk,crit} = 0.99$, while the KSWT speaker wall was used to perform a frequency sweep from 100 Hz to 2000 Hz at 110 dB amplitude while the transition behavior was observed using the IR camera. No sensitivity to sound was observed. The test was repeated with a 1856 µm forward-facing step at $Re_{kk}/Re_{kk,crit} = 0.99$. Similarly, no sensitivity to acoustic disturbance was observed.

4.2.4 Dual Step Testing

A 1323 µm aft-facing step was introduced at 1% x/c while a step sweep was performed at 15% x/c using the SWIFTER actuators at $Re' = 1.0 \times 10^6$/m. The critical behavior for the 15% x/c step (both forward- and aft-facing) was not affected by the introduction of the

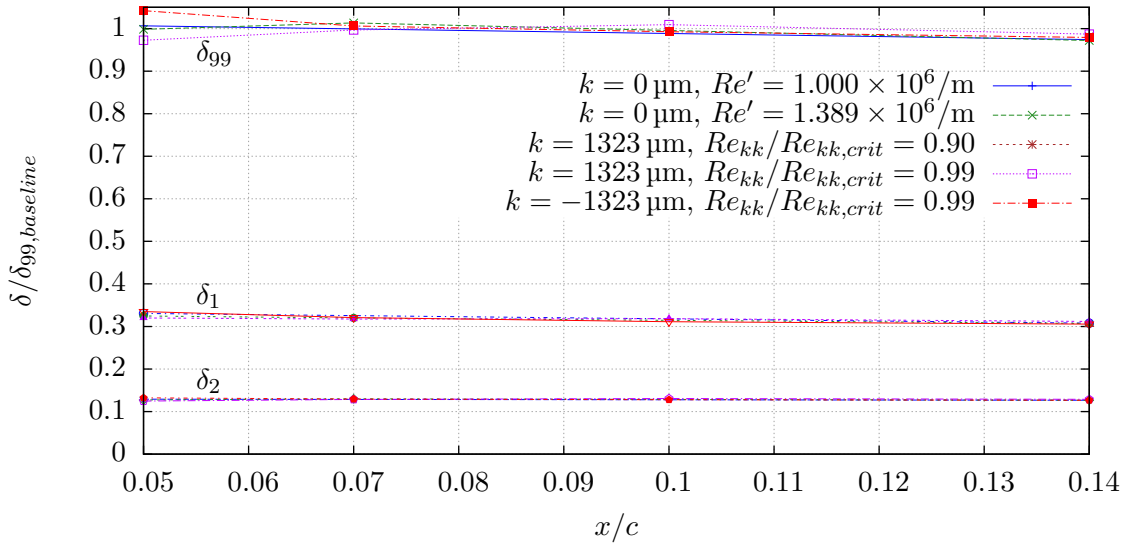

Figure 4.13: Boundary layer thickness comparison, normalized to baseline CFD δ_{99}

large, but subcritical, 1% x/c step. The test was repeated with an 1856 µm forward-facing step at 1% x/c. Similarly, no effect was observed on the critical behavior of the step at 15% x/c.

5. CONCLUSIONS

5.1 Subcritical Behavior

The previous studies on SETS by Drake et al. (2010) as well as the previous work on SWIFTER did not show any significant subcritical behavior. The wind tunnel testing of SWIFTEST also did not show any significant subcritical behavior in the IR thermography campaign. Figure 5.3 shows the steady disturbance amplitude of SWIFTEST as a function of x/c aft of the excrescence. As indicated by the IR thermography results, none of the configurations appear to be unstable in the subcritical regime, even at Re_{kk} of 99% of the critical value. However, a slight disturbance, which is quickly damped below the noise floor is observed at 5% x/c for the largest forward facing step. This indicates that the step does induce a small disturbance, but it is quite damped. This is not surprising since the neutral point for crossflow is well aft of the step for SWIFTEST at these conditions.

In the flight environment, however, the step is very near the neutral point for crossflow. As expected, the disturbance then grows rapidly and leads to early transition. This subcritical elevation in crossflow growth is visible as both stronger crossflow streaking in the IR thermography, as well as in early transition, as shown in Figure 5.2. The subcritical behavior is also destabilized by increasing the global pressure gradient as well as freestream Reynolds number, further supporting the theory that the step is acting as a receptivity source near the neutral point and elevating the crossflow initial amplitude.

It is likely that this disturbance is also present with SWIFTER. However, since crossflow is not very unstable in the Reynolds numbers tested in the KSWT for this model, no significant growth was observed. Additionally, since the 15% excrescence is well aft of the neutral point in flight, it is likely that a minor disturbance was introduced, but was not significant compared to the already present crossflow disturbance. As such, no significant subcritical behavior was evident.

As a general guideline, it would be advisable to avoid placing an excrescence in the

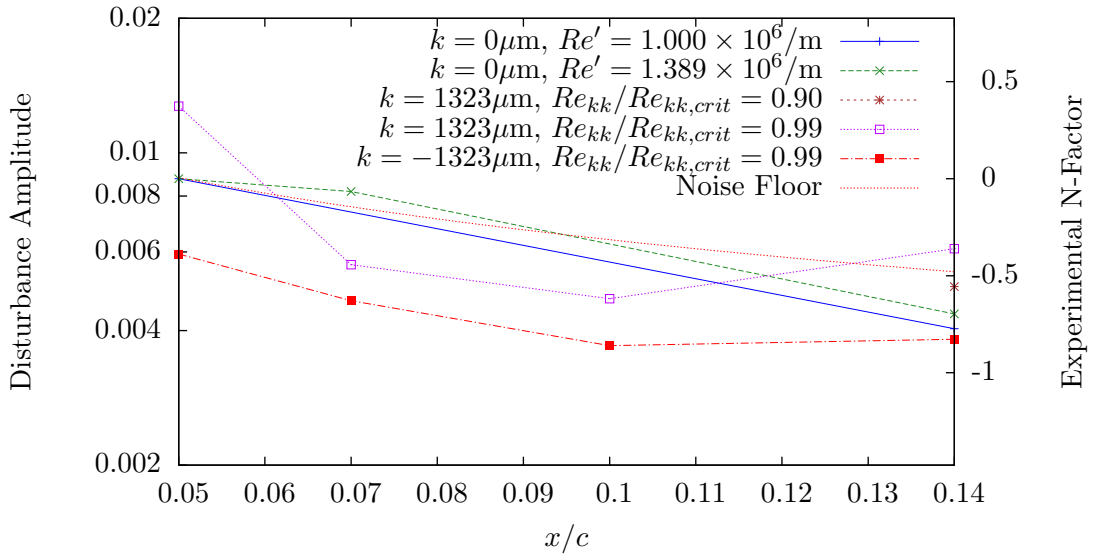

Figure 5.1: Disturbance amplitude vs x/c

neighborhood of the crossflow neutral point on a production aircraft, in order to avoid a partial loss of laminar flow due to these effects.

5.2 Critical Behavior

5.2.1 Comparison to Previous Studies

Historically, studies like Braslow & Knox (1958), and Smith & Clutter (1959) have been used to set general manufacturing tolerances for laminar flow wings. Some of their results are summarized in Table 5.1. To put those numbers in perspective, a strip of standard scotch tape on SWIFTEST at 0.15 x/c at $Re' = 5.5 \times 10^6$/m has an Re_{kk} of approximately 100 while a piece of masking tape in the same configuration has an Re_{kk} of approximately 500. Fortunately, the roughness types examined in those studies are rather poor analogs for two-dimensional steps. Those types of roughness do not exhibit the same breakdown due to a spanwise separation bubble, and as such, they should not be used to inform design decisions involving phenomena that do, such as pure 2-D steps.

Table 5.2 compares the more recent efforts examining pure 2-D steps. The table is divided into a top half and bottom half; the top half covers the moderate Reynolds numbers

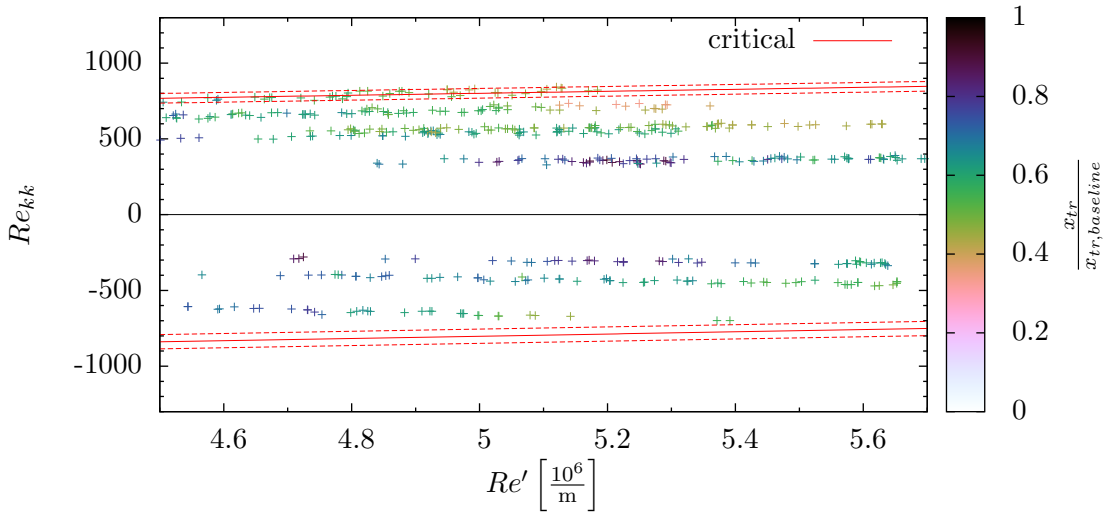

Figure 5.2: Transition fraction at $\alpha = -6.5°$

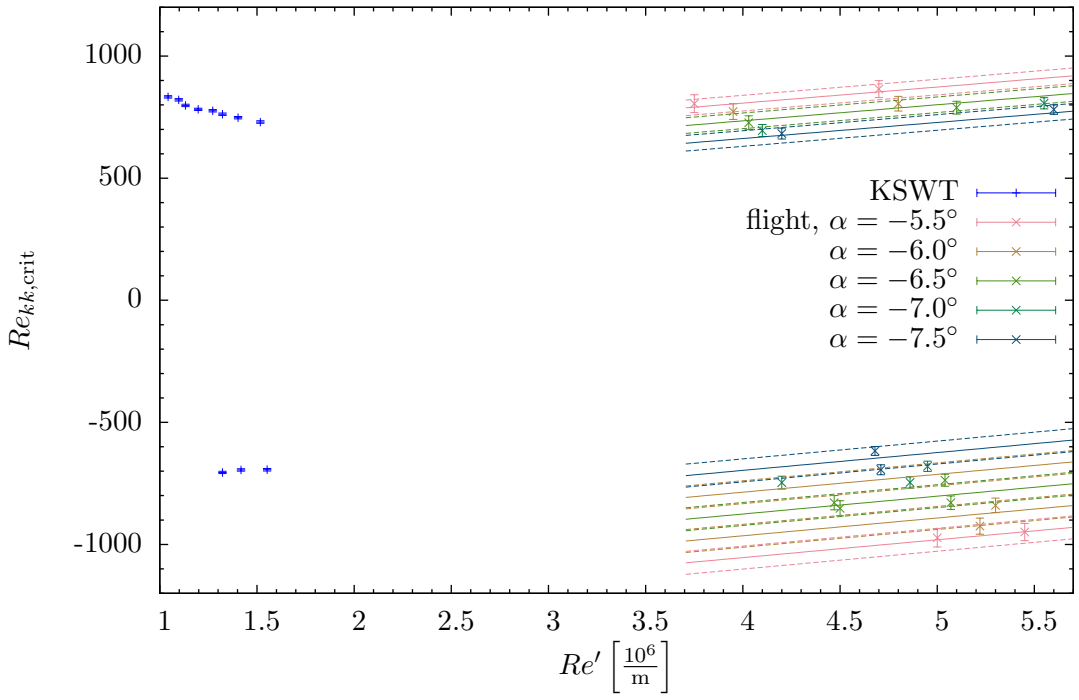

Figure 5.3: Critical step height

Table 5.1: Historical roughness $Re_{kk,crit}$

Reference	Condition	$Re_{kk,crit}$
Braslow & Knox (1958)	Distributed roughness	120-400
	Spanwise wires	40-260
Smith & Clutter (1959)	Row of spanwise 1.6 mm diameter disks	100-550
	Sandpaper-like roughness, 6.4 mm wide	178-330

Table 5.2: Comparison of $Re_{kk,crit}$ to previous studies; SETS (Drake et al., 2010), SWIFTER (Duncan, 2014)

Project	Re' 10^6/m	x_k/c -	Sweep deg	$\frac{dc_{p,3D}}{ds}$ 1/m	$Re_{kk,crit,aft}$ -	$Re_{kk,crit,fwd}$ -
SETS Grad Z	0.80 - 1.97	0.15	0	-0.1	-300	800
SETS Grad A	0.80 - 1.97	0.15	0	-0.6	-900	2100
SWIFTER	1.5	0.15	30	-1.1	-1040 ± 100	1560 ± 100
SWIFTEST	1.5	0.01	30	-25.5	-694 ± 5	730 ± 5
SWIFTER	5.5	0.15	30	-1.6	-280 ± 60	1290 ± 110
SWIFTEST	5.5	0.01	30	-18.5	-590 ± 50	760 ± 30
SWIFTEST	5.5	0.01	30	-20.6	-770 ± 50	830 ± 30
SWIFTEST	5.5	0.01	30	-22.7	-940 ± 50	910 ± 30

commonly seen in the wind tunnel environment, while the bottom half covers transport-aircraft-representative Reynolds numbers. The SETS Grad A results listed were performed by Drake et al. (2010) over the Reynolds number range listed. They found a mild trend in Reynolds number, but the numbers listed are fairly representative of that regime. The SWIFTER and SWIFTEST results also showed mild trends with Reynolds number in the individual regimes, and fairly significant trends between the wind tunnel and flight testing regimes. In order to better compare results, a single critical value was selected from each regime at the listed conditions. The $dc_{p,3D}/ds$ value listed for each experiment was taken at the excrescence location, in the baseline (zero step) configuration.

5.2.2 Sweep Effects

Sweep appears to be mildly destabilizing when comparing the SETS Grad A results from Drake et al. (2010) to the SWIFTER results from Duncan (2014). This effect is likely due to the introduction of spanwise-periodic non-uniformity in the mean flow due to crossflow growth, which could result in slightly earlier onset of the breakdown of the separated region entrained in the step.

The subcritical excitation of crossflow growth observed on SWIFTEST only appears to occur if the step is located near the crossflow neutral point, which will be influenced by sweep. Additionally, since it appears that this subcritical phenomena is a function of crossflow growth, it is likely that if sweep is increased or decreased, the effect will be more or less pronounced, respectively.

5.2.3 Reynolds Number Effects

In general, these experiments only show a slight influence with respect to freestream Reynolds number individually, and it is generally slightly destabilizing. The main exception is the forward-facing flight configuration for SWIFTER, which appears to be significantly destabilized by increasing Reynolds number, but is initially more stable than the wind tunnel test case at much lower freestream Reynolds number. In general, the forward-facing configurations appear to exhibit more unusual behavior than their aft-facing counterparts. In both the SWIFTER and SWIFTEST wind tunnel campaigns, the forward-facing steps appear to be slightly destabilized by increasing Reynolds number, while at flight Reynolds numbers, SWIFTEST shows a slight stabilizing effect with Reynolds number at the edge of the experimental uncertainty. Overall, it appears that the forward-facing-step experiments are significantly more complicated to model adequately. This is likely due to the interplay between the two separated regions (one in front of the step, and one on top of the step).

5.2.4 Pressure Gradient Effects

Pressure gradient appears to have a generally stabilizing effect on the critical behavior. The work on the SETS model by Drake et al. (2010) shows a significant stabilization be-

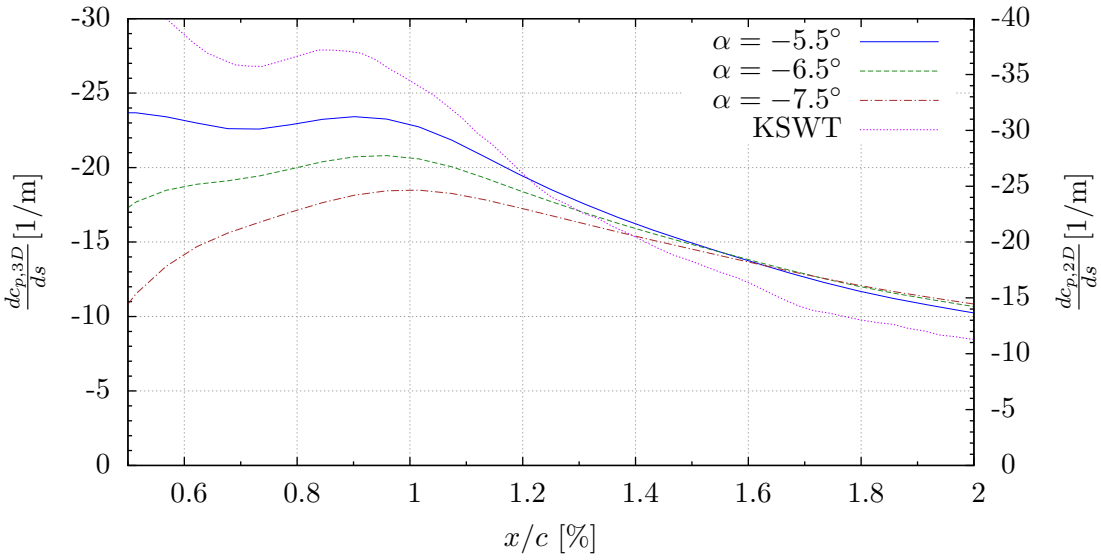

Figure 5.4: Local pressure gradient near 1% x/c

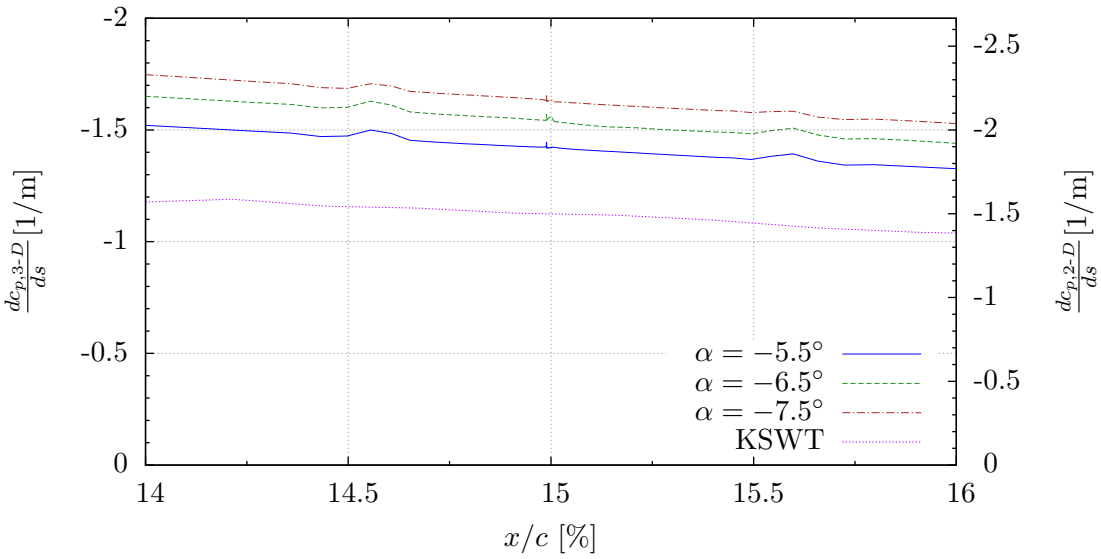

Figure 5.5: Local pressure gradient near 15% x/c

tween the Grad Z model and Grad A model. However, it should be noted that the results are potentially influenced by a slight suction peak in front of the excrescence. SWIFTEST also showed a significant stabilization due to increasing pressure gradient, as evidenced in both Table 5.2 and Figure 5.3. SWIFTER, on the other hand, exhibited no significant influence due to angle of attack. However, if the pressure gradient at the 15% x/c excrescence location from SWIFTER is compared to the 1% x/c excrescence location from SWIFTEST, there is a significant difference in the range of local pressure gradients. SWIFTER was primarily tested at $\alpha = -6.5°$ and $\alpha = -7.5°$ which corresponds to a range in $dc_{p,3D}/ds$ of -1.56 to -1.63 [1/m], as indicated in Figure 5.5; whereas SWIFTEST was tested essentially continuously between $\alpha = -5.5°$ and $\alpha = -7.5°$, which corresponds to $dc_{p,3D}/ds$ of -18.5 to -22.7 [1/m], as indicated in Figure 5.4. As such, it is unsurprising that SWIFTER exhibits minimal variation due to it's comparatively small variation in pressure gradient local to the excrescence. However, the excrescence appears to be less stable, in general, for the 1% x/c testing on SWIFTEST than the 15% x/c SWIFTER. Since the pressure gradient appears to be stabilizing for all other comparisons, it appears that there must be an additional sensitivity.

5.2.5 Acoustic Disturbances

SWIFTEST was tested for sensitivity to acoustic disturbances in the KSWT at frequencies from 100 Hz to 2000 Hz at 110 dB at both a large aft-facing and forward-facing step. No effect was observed. SWIFTER was also previously tested for influence by acoustic disturbances and was found to be insensitive as well (Duncan, 2014).

5.2.6 Multiple Excrescences

In the wind tunnel, critical step height measurements were taken at 15% x/c while large subcritical forward- and aft-facing steps were introduced at 1% x/c. No influence from the 1% x/c step was observed on the 15% x/c step critical behavior. This is unsurprising due to the fact that the subcritical excrescences at 1% x/c were found to have no effect aft of 7% x/c during hotwire testing. However, this is a useful finding to confirm from a practical

standpoint. There are many practical instances where there may be an excrescence such as a wing-skin junction followed by a second excrescence, such as a slat junction, some distance downstream. It appears that the excrescences can be modeled independently. If the first excrescence is critical, the second excrescence is irrelevant since laminar flow has already been lost. If the first excrescence is subcritical, the critical behavior of the second excrescence can be modeled as if the first excrescence did not exist, assuming the second excrescence is at least a few percent x/c downstream. This dramatically simplifies such problems.

5.2.7 Other Sensitivities

SWIFTEST, with the exception of the aft-facing flight tests, is less stable than SWIFTER. SWIFTEST's conditions at the step have three major differences from SWIFTER. The pressure gradient is higher, the curvature is higher, and the boundary layer is thinner. In all testing, pressure gradient appears to be stabilizing. As such, it is not likely the reason for the earlier transition. At present, there is not a test article capable of separating the effects of curvature and boundary layer thickness rigorously. Additionally, it is quite difficult to develop a set of airfoils that can separate those two effects, along with Reynolds number, without a contrived surface that may induce other instabilities into the system.

5.3 Future Work

Moving forward, these results along with the previous studies can be used to inform design decisions in the regimes they each correspond with, as well as provide insight in the general behaviors of these systems. However, the real strength of these studies is to serve as a set of validation cases for the companion computational effort currently under way by Matthew Tufts and Dr. Helen Reed. Once an appropriate computational model is developed for the general case, using these results and others as validation, the problem is no-longer one of empirical correlation, but rather using the gathered knowledge to solve the problem in a relatively direct fashion. As such, that is the best long term solution for evaluating these type of instabilities induced by 2-D excrescences.

REFERENCES

Arnal D, Archambaud JP. 2009. Laminar-turbulent transition control: NLF, LFC, HLFC. *Adv. in Laminar-Turbulent Transit. Model.*, AVT-151 RTO AVT/VKI Lecture Series. Rhode St. Genèse, Belgium: von Karman Institute for Fluid Dynamics. ISBN 978-92-837-0090-6

Barkley D, Gomez MGM, Henderson RD. 2002. Three-dimensional instability in flow over a backward-facing step. *J. of Fluid Mech.*, 473:167–190. doi:10.1017/S002211200200232X

Bender AM, Drake A, McKay VS, Westphal RV, Yoshioka S, Kohama Y. 2007. An approach to measuring the effects of surface steps on transition using a propelled-model. *22nd Int. Congr. on Instrum. in Aerosp. Simul. Facil.* Pacific Grove, CA. ISBN 978-1-4244-1600-4. doi:10.1109/ICIASF.2007.4380873

Braslow AL, Knox EC. 1958. Simplified method for determination of critical height of distributed roughness particles for boundary-layer transition at Mach numbers from 0 to 5. *Tech. Rep. NACA Technical Note No. 4363*, Langley Field, VA

Cessna. 1968. O-2A airplane vibration and flutter analysis. *Tech. Rep. Cessna Report S-M337-27-3*, Wichita, KS

Crawford BK, Duncan GT Jr, West DE, Saric WS. 2014. Large-span, non-contact surface profilometry for laminar-flow diagnostics. *30th AIAA Aerodyn. Meas. Technol. and Ground Test. Conf.*, AIAA Paper No. 2014-2940. Atlanta, GA. doi:10.2514/6.2014-2940

Downs RS III. 2012. *Environmental Influences on Crossflow Stability.* Ph.D. thesis, Texas A&M University, College Station, TX

Drake A, Bender AM. 2009. Surface excrescence transition study. *Tech. Rep. AFRL-RB-TR-2009-3109*, Wright-Patterson Air Force Base, OH

Drake A, Bender AM, Korntheuer AJ, Westphal RV, McKeon BJ, et al. 2010. Step excrescence effects for manufacturing tolerances on laminar flow wings. *48th AIAA Aerosp. Sci. Meet.*, AIAA Paper No. 2010-0375. Orlando, FL. doi:10.2514/6.2010-0375

Drake A, Bender AM, Westphal RV. 2008. Transition due to surface steps in the presence of favorable pressure gradients. *26th AIAA Appl. Aerodyn. Conf.*, AIAA Paper No. 2008-7334. Honolulu, HI

Drake A, Westphal RV, Zuniga FA, Kennelly RA Jr, Koga DJ. 1996. Wing leading edge joint laminar flow tests. *Tech. Rep. NASA-TM-4762*, NASA Ames Research Center, Moffett Field, CA

Duncan GT Jr. 2014. *The Effects of Step Excrescences on Swept-Wing Boundary-Layer Transition.* Ph.D. thesis, Texas A&M University, College Station, TX

Duncan GT Jr, Crawford BK, Tufts MW, Saric WS, Reed HL. 2014a. Effects of step excrescences on a swept wing in a low-disturbance wind tunnel. *52nd AIAA Aerosp. Sci. Meet.*, AIAA Paper No. 2014-0910. National Harbor, MD. doi:10.2514/6.2014-0910

Duncan GT Jr, Crawford BK, Tufts MW, Saric WS, Reed HL. 2014b. Flight experiments on the effects of step excrescences on swept-wing transition. *Int. J. Eng. Syst. Model. and Simul.*, 6(3/4):171–180

Eppink J. 2014. *The Interaction of Crossflow Instabilities and a Backward Facing Step in Swept Boundary Layer Transition.* Ph.D. thesis, Tufts University, Medford, MA

Fage A. 1943. The smallest size of a spanwise surface corrugation which affects boundary-layer transition on an aerofoil. *Tech. Rep. A.R.C., R.&M. No. 2120*, London, UK

Holmes BJ, Obara CJ, Martin GL, Domack CS. 1985. Manufacturing tolerances for natural laminar flow airframe surfaces. *SAE, Gen. Aviat. Aircr. Meet. and Expo.*, SAE Paper No. 850863. Wichita, KS. doi:10.4271/850863

Hood MJ. 1939. The effects of some common surface irregularities. *Tech. Rep. NACA Technical Note No. 695*, Washington D.C.

Hunt LE, Downs RS III, Kuester MS, White EB, Saric WS. 2010. Flow quality measurements in the Klebanoff-Saric wind tunnel. *27th AIAA Aerodyn. Meas. Technol. and Ground Test. Conf.*, AIAA Paper No. 2010-4538. Chicago, IL. doi:10.2514/6.2010-4538

Sesco A, Visbal M, Rizzetta D. 2014. Numerical study of boundary layer receptivity to free-stream disturbances and surface excrescences. *7th AIAA Theor. Fluid Mech. Conf.*, AIAA Paper No. 2014-2212. Atlanta, GA. doi:10.2514/6.2014-2212

Smith AMO, Clutter DW. 1959. The smallest height of roughness capable of affecting boundary-layer transition. *J. of the Aerosp. Sci.*, 26(4):229–245. doi:10.2514/8.8019

Tani I, Hama R, Mituisi S. 1940. On the permissible roughness in the laminar boundary layer. *Tech. Rep. NASA-TM-89802*, Tokyo, Japan

Zuniga FA, Drake A, Kennelly RA Jr, Koga DJ, Westphal RV. 1994. Transonic flight test of a laminar flow leading edge with surface excrescences. *Tech. Rep. NASA-TM-4597*, Moffett Field, CA

APPENDIX A

SUB-CRITICAL FLIGHT DATA

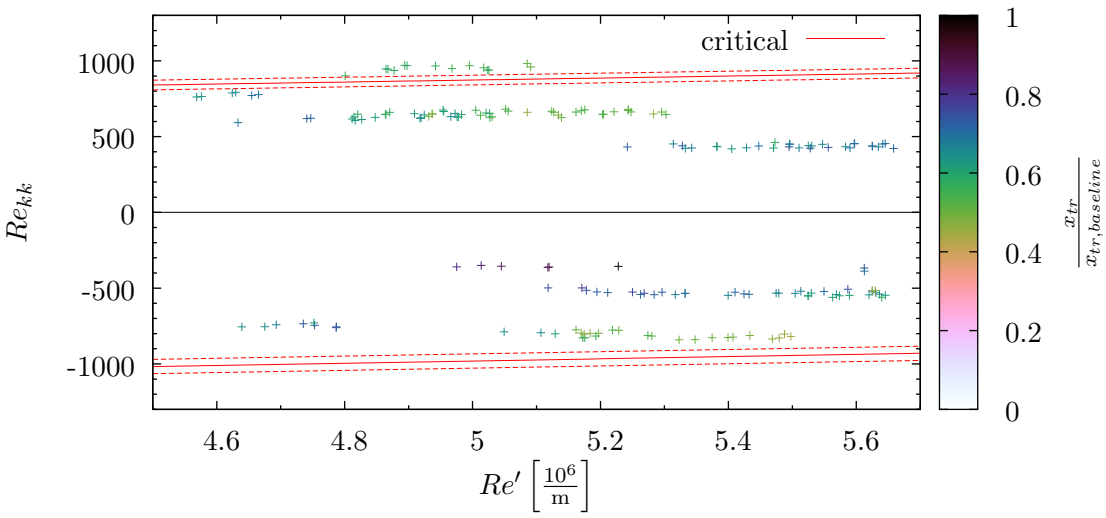

Figure A.1: Transition fraction at $\alpha = -5.5°$

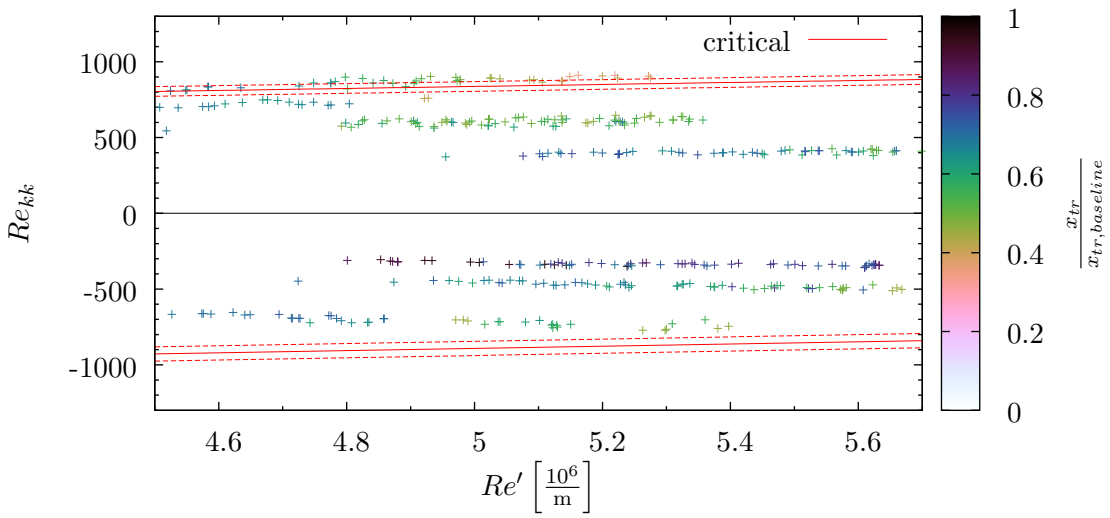

Figure A.2: Transition fraction at $\alpha = -6.0°$

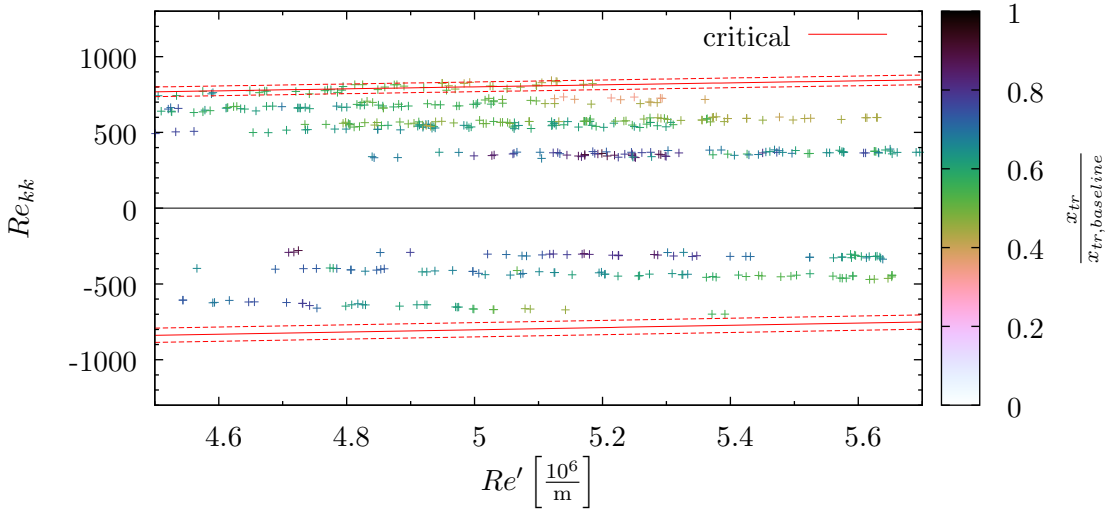

Figure A.3: Transition fraction at $\alpha = -6.5°$

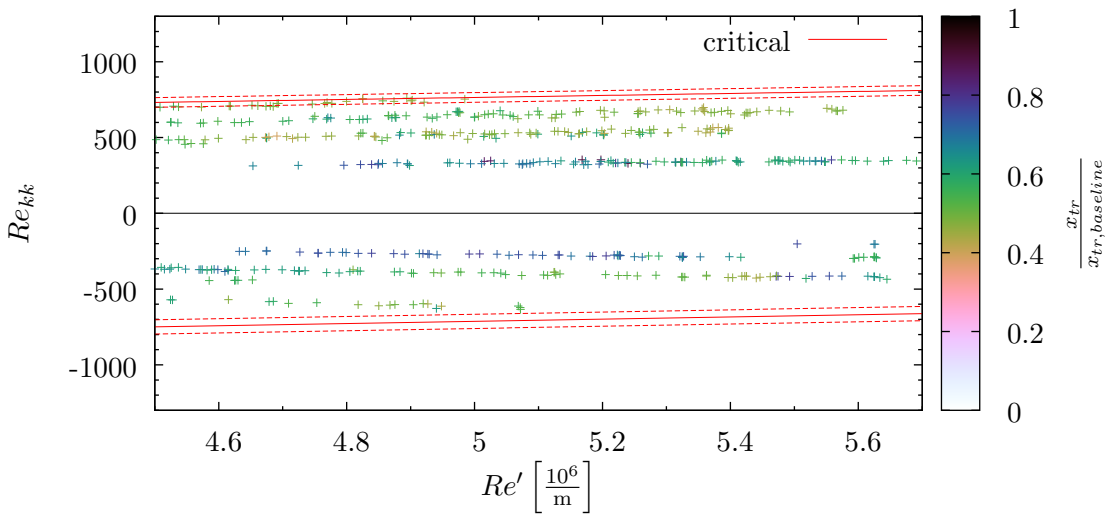

Figure A.4: Transition fraction at $\alpha = -7.0°$

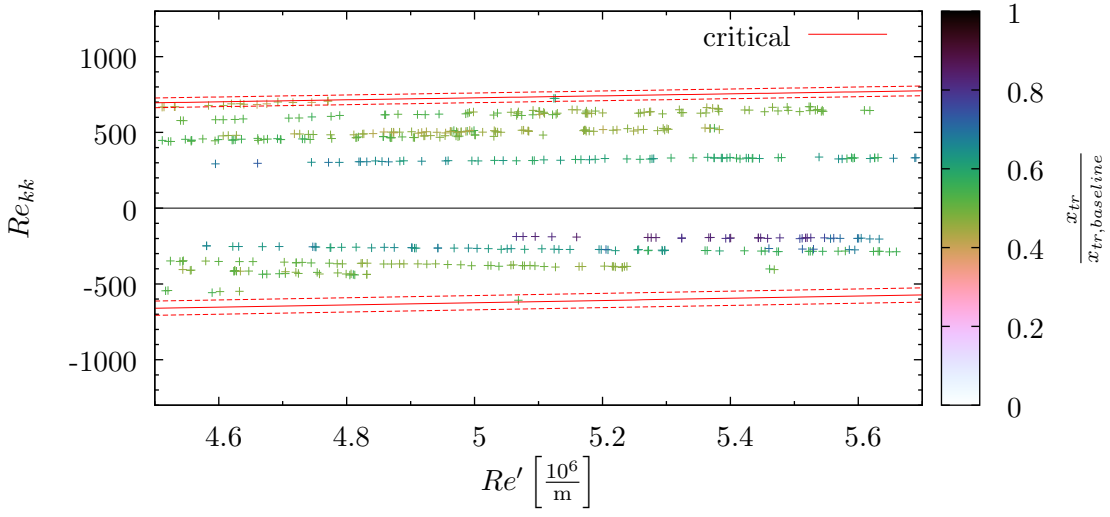

Figure A.5: Transition fraction at $\alpha = -7.5°$

APPENDIX B

HOTWIRE DISTURBANCE PROFILES

B.1 Baseline

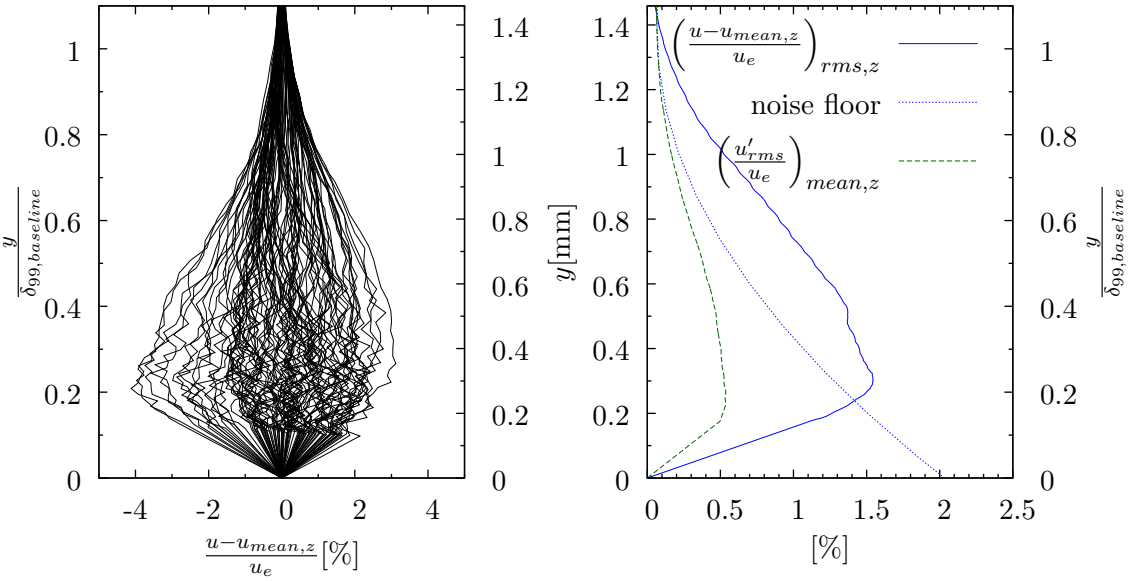

Figure B.1: $x/c = 5\%$ $Re' = 1.000 \times 10^6$/m

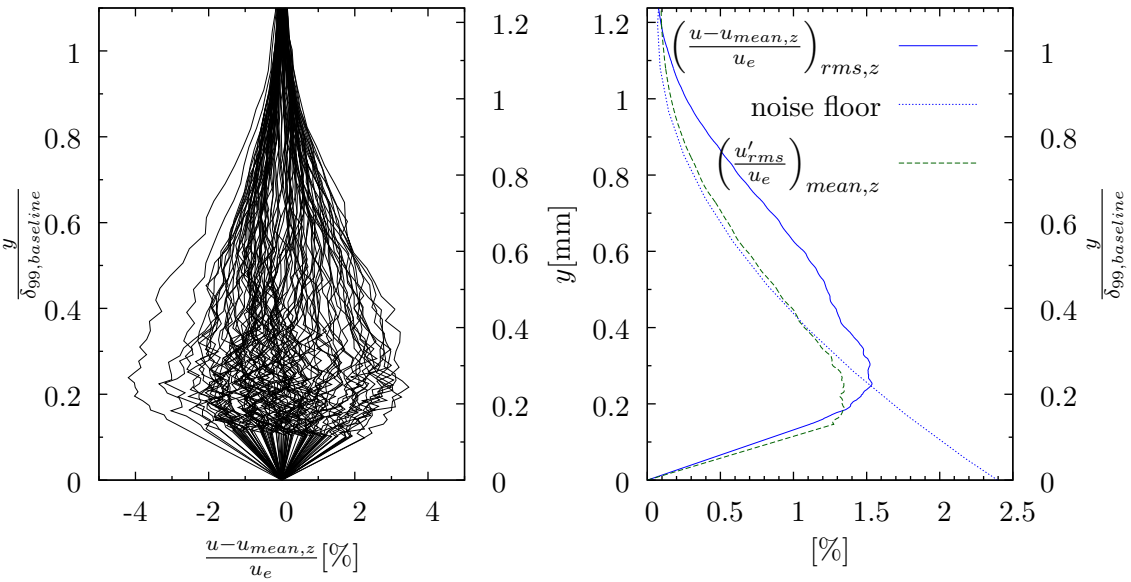

Figure B.2: $x/c = 5\%$ $Re' = 1.389 \times 10^6$/m

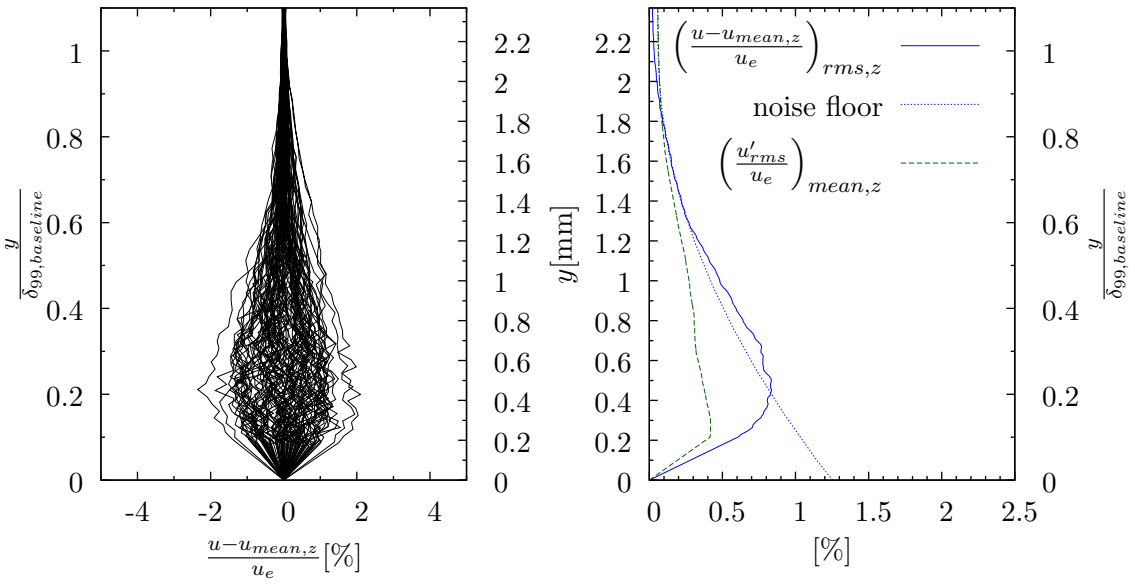

Figure B.3: $x/c = 14\%$ $Re' = 1.000 \times 10^6$/m

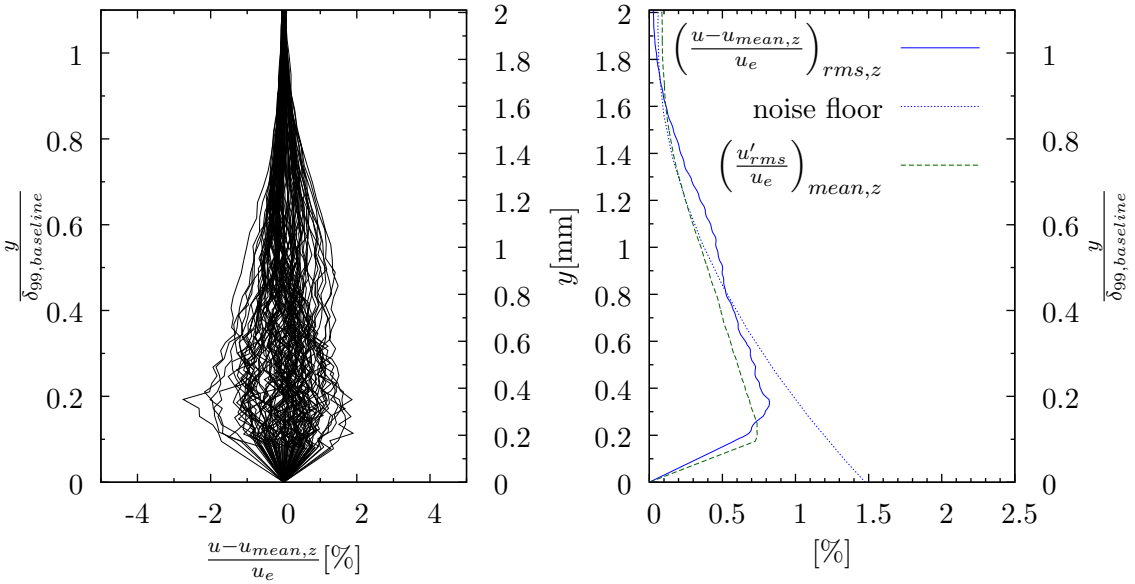

Figure B.4: $x/c = 14\%$ $Re' = 1.389 \times 10^6$/m

B.2 $k = 1323\,\mu m$ $Re_{kk}/Re_{kk,crit} = 0.99$

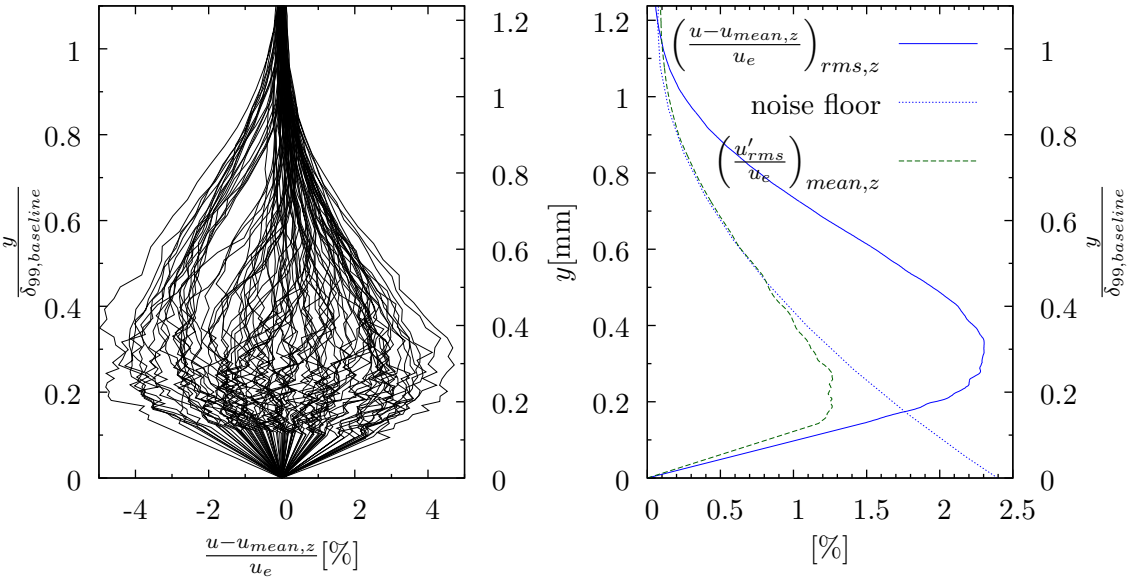

Figure B.5: $x/c = 5\%$

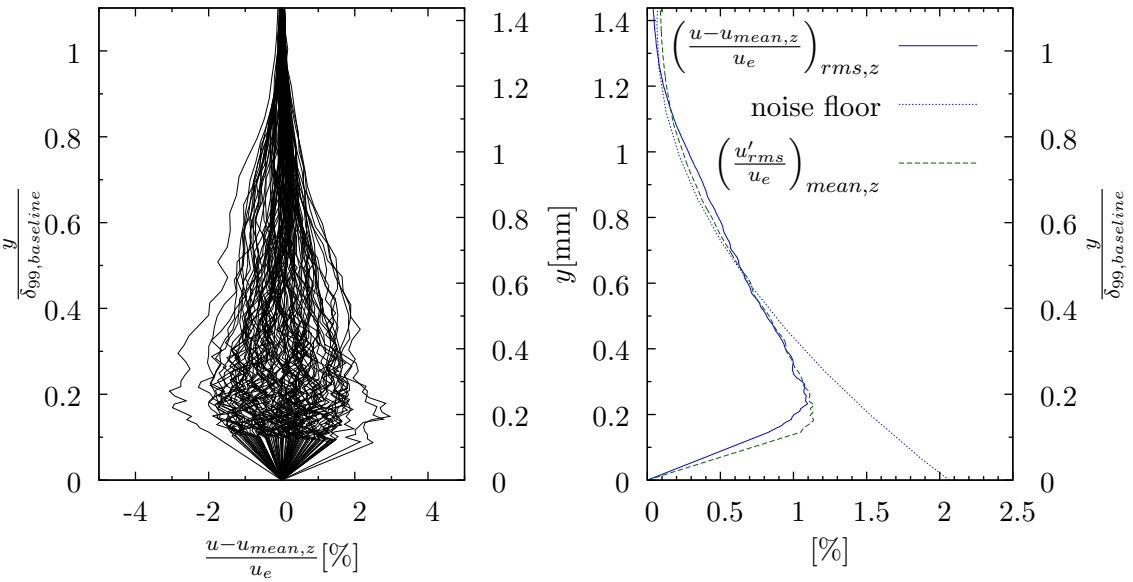

Figure B.6: $x/c = 7\%$

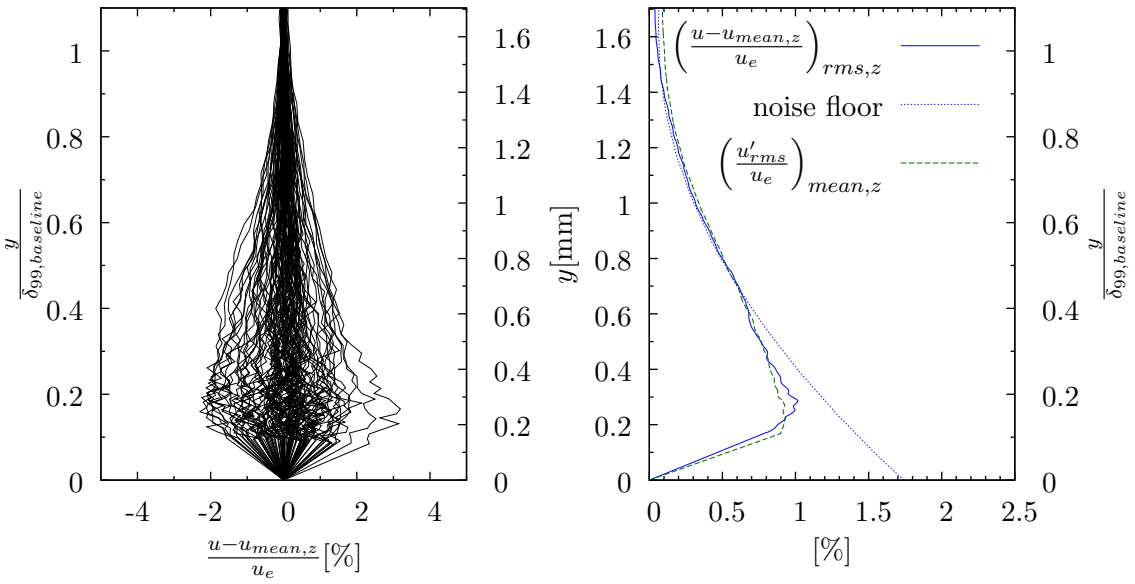

Figure B.7: $x/c = 10\%$

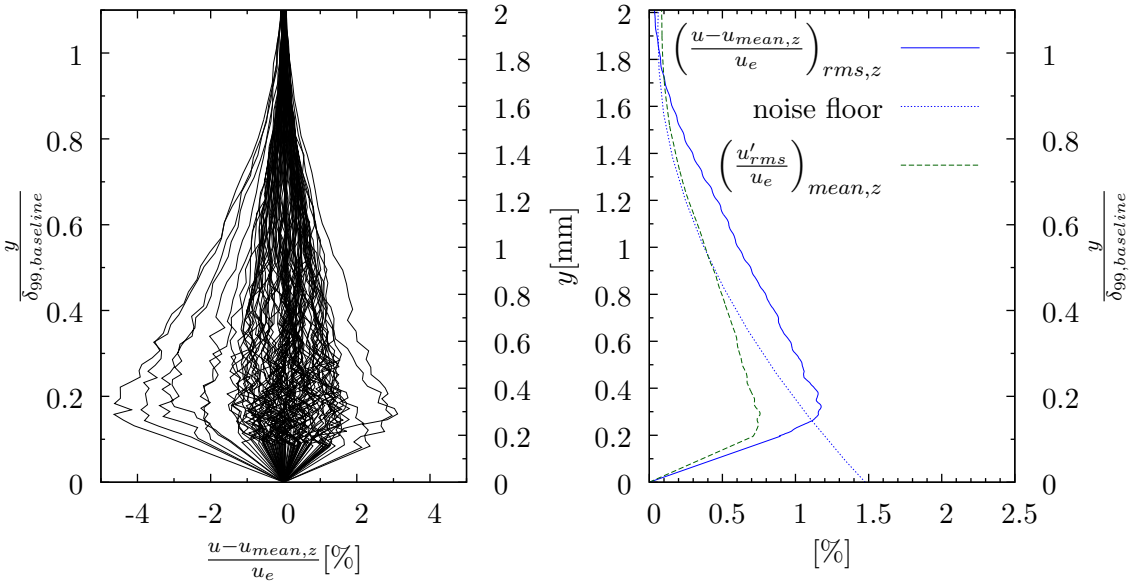

Figure B.8: $x/c = 14\%$

B.3 $k = -1323\,\mu m$ $Re_{kk}/Re_{kk,crit} = 0.99$

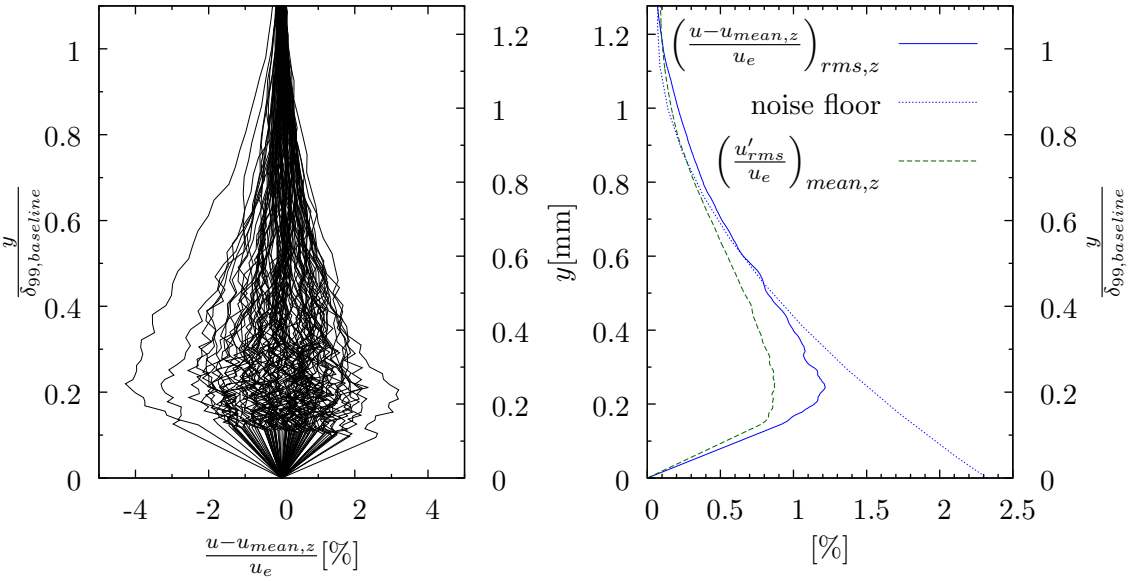

Figure B.9: $x/c = 5\%$

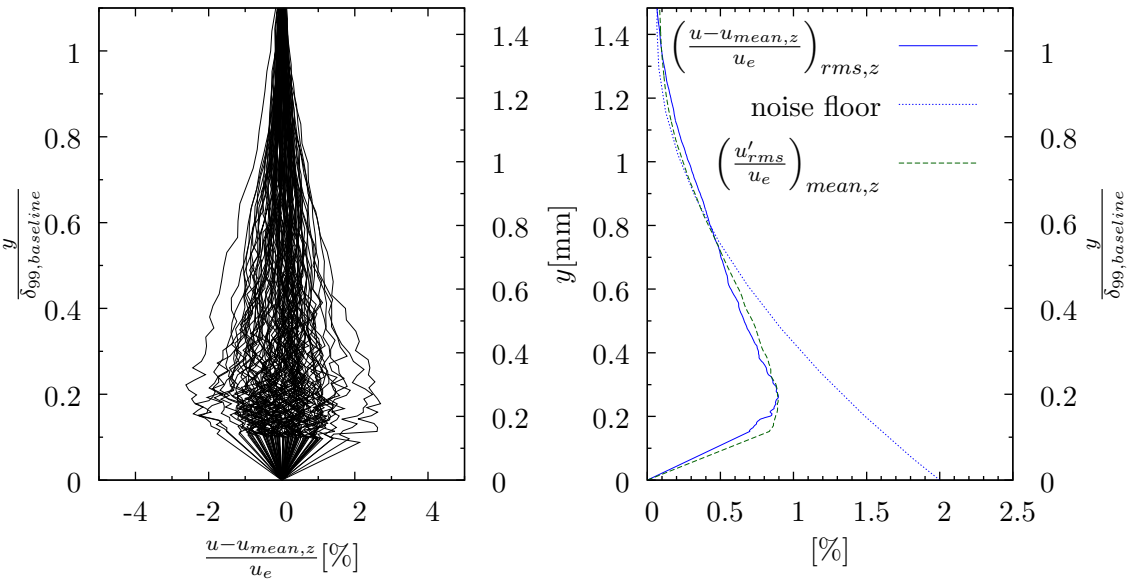

Figure B.10: $x/c = 7\%$

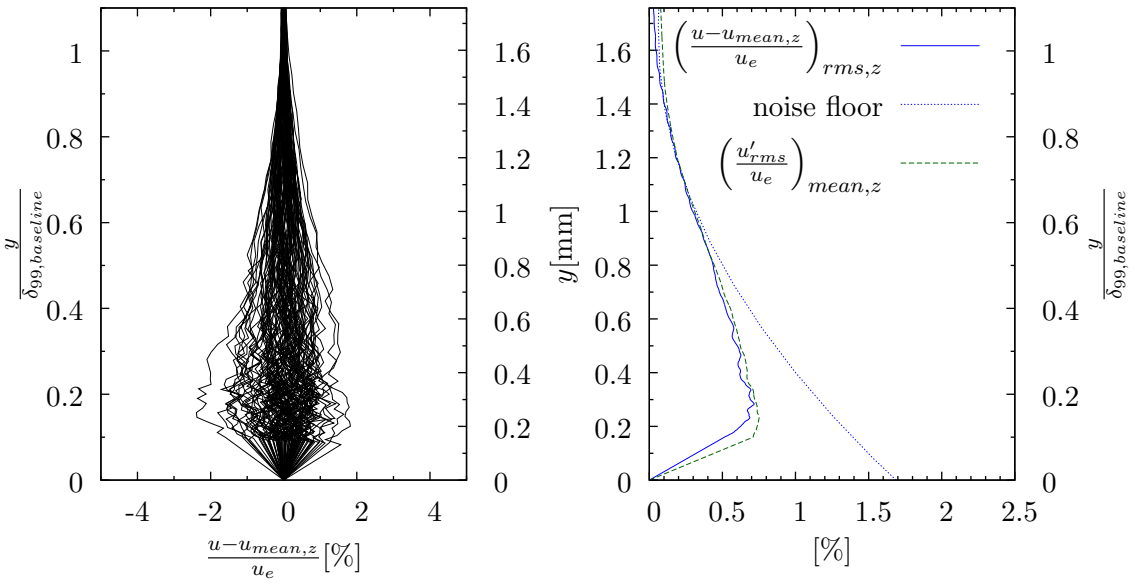

Figure B.11: $x/c = 10\%$

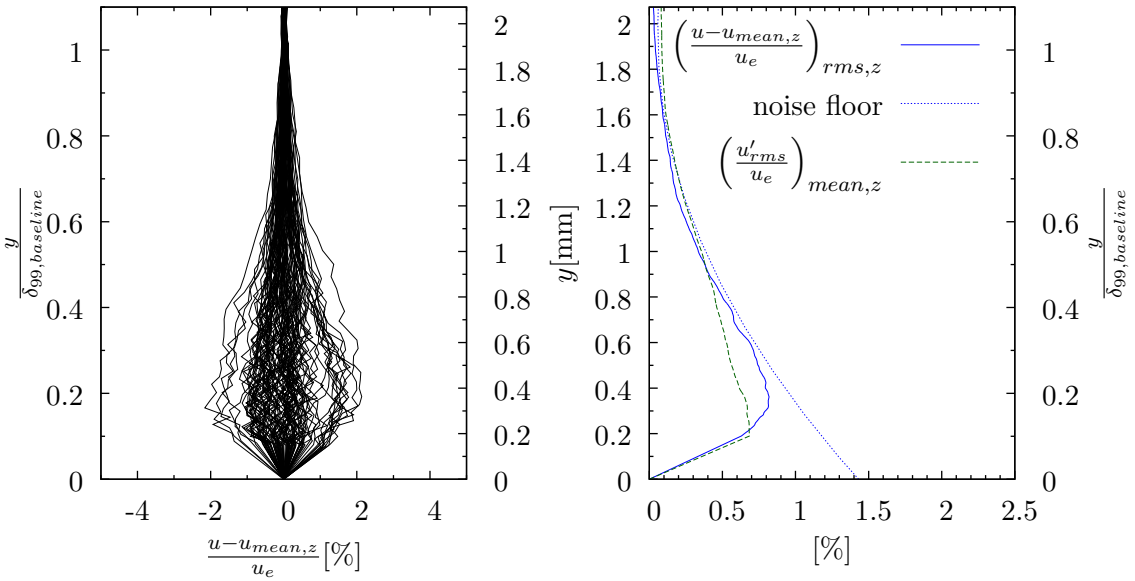

Figure B.12: $x/c = 14\%$

APPENDIX C

SHIM CONFIGURATIONS

Table C.1: Possible shim configurations

shim configurations used noted in **bold**

thickness 10^{-3} in	thickness µm	k µm	σ_k µm	n	shim list 10^{-3} in
-62	**-1575**	**-1323**	**7**	**0**	
-61	-1549	-1301	7	1	001
-60	-1524	-1280	7	1	002
-59	-1499	-1259	7	2	001 002
-58	-1473	-1237	7	2	002 002
-57	**-1448**	**-1216**	**7**	**1**	**005**
-56	-1422	-1194	7	2	001 005
-55	-1397	-1173	7	2	002 005
-54	-1372	-1152	7	1	008
-53	-1346	-1130	7	2	001 008
-52	**-1321**	**-1109**	**7**	**1**	**010**
-51	-1295	-1087	7	2	001 010
-50	-1270	-1066	7	2	002 010
-49	-1245	-1045	7	2	005 008
-48	-1219	-1024	7	3	002 002 010
-47	-1194	-1003	7	2	005 010
-46	-1168	-981	7	2	008 008
-45	-1143	-960	7	3	002 010 005
-44	-1118	-939	7	1	018
-43	-1092	-917	7	2	001 018
-42	-1067	-896	7	1	020
-41	-1041	-874	7	2	001 020
-40	-1016	-853	7	2	002 020
-39	-991	-832	7	2	005 018
-38	-965	-810	7	3	008 008 008
-37	-940	-789	7	1	025
-36	-914	-768	7	2	008 018
-35	-889	-747	7	2	002 025
-34	-864	-726	7	2	010 018
-33	-838	-704	7	3	002 002 025
-32	-813	-683	7	2	010 020
-31	-787	-661	7	1	031
-30	-762	-640	7	2	001 031
-29	-737	-619	7	2	008 025
-28	-711	-597	7	3	008 008 018
-27	-686	-576	7	2	010 025
-26	-660	-554	7	2	018 018
-25	-635	-533	7	3	002 025 010
-24	-610	-512	7	2	018 020

thickness 10^{-3} in	thickness µm	k µm	σ_k µm	n	shim list 10^{-3} in
-23	-584	-490	7	2	008 031
-22	**-559**	**-469**	**7**	**2**	**020 020**
-21	-533	-448	7	2	010 031
-20	-508	-427	7	3	002 020 020
-19	**-483**	**-406**	**7**	**2**	**018 025**
-18	-457	-384	7	3	008 018 018
-17	**-432**	**-363**	**7**	**2**	**020 025**
-16	-406	-341	7	3	010 018 018
-15	-381	-320	7	3	008 008 031
-14	-356	-299	7	3	010 020 018
-13	**-330**	**-277**	**7**	**2**	**018 031**
-12	-305	-256	7	2	025 025
-11	**-279**	**-234**	**7**	**2**	**020 031**
-10	-254	-213	7	3	002 025 025
-9	-229	-192	7	3	010 025 018
-8	**-203**	**-170**	**7**	**3**	**018 018 018**
-7	-178	-149	7	3	010 025 020
-6	**-152**	**-128**	**7**	**2**	**025 031**
-5	-127	-107	7	3	008 031 018
-4	-102	-86	7	3	018 020 020
-3	-76	-64	7	3	010 031 018
-2	-51	-43	7	3	020 020 020
-1	-25	-21	7	3	018 018 025
0	**0**	**0**	**7**	**2**	**031 031**
1	25	21	7	3	018 025 020
2	51	43	7	3	008 031 025
3	76	64	7	3	020 020 025
4	102	86	7	3	010 031 025
5	127	107	7	3	018 018 031
6	152	128	7	3	018 025 025
7	178	149	7	3	018 031 020
8	203	170	7	3	020 025 025
9	**229**	**192**	**7**	**3**	**020 020 031**
10	254	213	7	3	010 031 031
11	279	234	7	4	010 025 020 018
12	305	256	7	3	018 031 025
13	330	277	7	3	025 025 025
14	**356**	**299**	**7**	**3**	**020 031 025**
15	381	320	7	4	010 031 018 018
16	406	341	7	4	018 020 020 020
17	432	363	7	4	018 018 018 025
18	**457**	**384**	**7**	**3**	**018 031 031**
19	483	406	7	3	025 025 031

thickness 10^{-3} in	thickness µm	k µm	σ_k µm	n	shim list 10^{-3} in
20	508	427	7	3	020 031 031
21	**533**	**448**	**7**	**4**	**018 025 020 020**
22	559	469	7	4	010 031 025 018
23	584	490	7	4	020 020 020 025
24	610	512	7	4	018 018 025 025
25	635	533	7	3	025 031 031
26	660	554	7	4	018 025 025 020
27	686	576	7	4	018 031 020 020
28	711	597	7	4	020 020 025 025
29	737	619	7	4	020 020 020 031
30	762	640	7	4	018 018 031 025
31	787	661	7	3	031 031 031
32	813	683	7	4	018 031 025 020
33	838	704	7	4	020 025 025 025
34	864	726	7	4	020 020 031 025
35	889	747	7	4	010 031 031 025
36	914	768	7	4	018 018 031 031
37	940	789	7	4	018 031 025 025
38	965	810	7	4	025 025 025 025
39	991	832	7	4	020 031 025 025
40	1016	853	7	4	020 020 031 031
41	1041	874	7	4	010 031 031 031
42	1067	896	8	5	018 018 018 025 025
43	1092	917	7	4	018 031 031 025
44	1118	939	7	4	025 025 025 031
45	1143	960	7	4	020 031 031 025
46	1168	981	8	5	018 025 025 020 020
47	1194	1003	8	5	018 031 020 020 020
48	1219	1024	8	5	020 020 020 025 025
49	1245	1045	7	4	018 031 031 031
50	1270	1066	7	4	025 025 031 031
51	1295	1087	7	4	020 031 031 031
52	1321	1109	8	5	018 031 025 020 020
53	1346	1130	8	5	020 020 025 025 025
54	1372	1152	8	5	020 020 020 031 025
55	1397	1173	8	5	018 018 031 025 025
56	**1422**	**1194**	**7**	**4**	**025 031 031 031**
57	1448	1216	8	5	018 031 025 025 020
58	1473	1237	8	5	020 025 025 025 025
59	1499	1259	8	5	020 020 031 025 025
60	1524	1280	8	5	020 020 020 031 031
61	1549	1301	8	5	018 018 031 031 025
62	**1575**	**1323**	**7**	**4**	**031 031 031 031**

thickness 10^{-3} in	thickness µm	k µm	σ_k µm	n	shim list 10^{-3} in
63	1600	1344	8	5	025 025 025 025 025
64	1626	1365	8	5	020 031 025 025 025
65	1651	1386	8	5	020 020 031 031 025
66	1676	1407	8	5	010 031 031 031 025
67	**1702**	**1429**	**8**	**5**	**018 018 031 031 031**
68	1727	1450	8	5	018 031 031 025 025
69	1753	1472	8	5	025 025 025 025 031
70	1778	1493	8	5	020 031 031 025 025
71	**1803**	**1514**	**8**	**5**	**020 020 031 031 031**
72	1829	1536	8	5	010 031 031 031 031
73	1854	1557	8	6	020 020 020 025 025 025
74	1880	1579	8	5	018 031 031 031 025
75	1905	1600	8	5	025 025 025 031 031
76	**1930**	**1621**	**8**	**5**	**020 031 031 031 025**
77	1956	1643	8	6	018 031 025 025 020 020
78	1981	1664	8	6	020 020 025 025 025 025
79	2007	1685	8	6	020 020 020 031 025 025
80	2032	1706	8	5	018 031 031 031 031
81	2057	1727	8	5	025 025 031 031 031
82	**2083**	**1749**	**8**	**5**	**020 031 031 031 031**
83	2108	1770	8	6	020 025 025 025 025 025
84	2134	1792	8	6	020 020 031 025 025 025
85	2159	1813	8	6	020 020 020 031 031 025
86	2184	1834	8	6	018 018 031 031 025 025
87	**2210**	**1856**	**8**	**5**	**025 031 031 031 031**
88	2235	1877	8	6	025 025 025 025 025 025
89	2261	1899	8	6	020 031 025 025 025 025
90	2286	1920	8	6	020 020 031 031 025 025
91	2311	1941	8	6	020 020 020 031 031 031
92	2337	1962	8	6	018 018 031 031 031 025
93	**2362**	**1983**	**8**	**5**	**031 031 031 031 031**